

# Metal-Organic and Oxide Nanostructures for Electrocatalyzing the Oxygen Half-Cell Reaction

THIS IS A TEMPORARY TITLE PAGE  
It will be replaced for the final print by a version  
provided by the service academique.

Thèse n. 8449 2018  
présenté le 7 juin 2018  
à la Faculté des Sciences de Base  
Laboratoire de Science à l'Échelle Nanométrique  
Programme doctoral en Science et Génie des Matériaux  
École Polytechnique Fédérale de Lausanne

pour l'obtention du grade de Docteur ès Sciences  
par

Diana Hötger



acceptée sur proposition du jury:

Prof Karen Scrivener, président du jury

Prof Klaus Kern, directeur de thèse

Prof Michael Gottfried, rapporteur

Prof Sabine Maier, rapporteur

Prof Anna Fontcuberta i Morral, rapporteur

Lausanne, EPFL, 2018



Indes sie forschten, röntgten, filmten, funkten, entstanden von selbst die köstlichsten  
Erfindungen: der Umweg als die kürzeste Verbindung zwischen zwei Punkten  
— Erich Kästner (1899-1974)



## **Von Hier an Blind**

Zwischen zwei Fragen  
In der Lücke zwischen zwei Tagen blieb  
nichts mehr zu sagen  
Kein Leid mehr zu beklagen und ich  
Nahm den Wagen  
Und ging vor ihm auf die Knie  
Ich sagte: "Ich weiß nicht weiter  
War ich noch nie"

Ich und der Wagen  
Und der Bienenschwarm im Magen  
Und die Straße die zu schlagen war  
Wir haben uns vertragen aber  
Vor zwei Tagen  
Ging der Wagen in die Knie  
Er sagte: "Ich weiß nicht weiter  
War ich noch nie"

*Chorus: //:Ich weiß nicht weiter  
Ich weiß nicht, wo wir sind  
Ich weiß nicht weiter  
Von hier an blind ://*

Ich und mein Magen  
Und der Kopf in meinem Kragen giengen  
blind getragen von zwei Füßen  
Die nichts sagen  
Außer: "Gib dich geschlagen  
Und geh endlich in die Knie"  
Ich sagte: "Ich weiß nicht weiter  
War ich noch nie"

*Chorus*

Ich weiß nicht weiter  
Und keine Tausend Meter draußen vor dem Tor  
Erklang ein Brausen und es sang ein Männerchor  
Dann war Stille und dazwischen und davor  
Setzte die Pause neue Flausen in mein Ohr  
Und ich: Ich weiß nicht weiter

Wir sind Helden, *Von Hier an Blind*



# Abstract

Fluctuations in energy production common to sustainable energy sources need to be compensated with efficient storage systems to bridge times of low production rates. Storing energy in chemical bonds, a process accessible in electrochemical conversion, is a simple approach to provide a constant energy supply. The water cycle, specifically the water splitting reaction and its back reaction provides a clean process with ideally sufficient energy output to drive electrical devices. However, the water cycle is limited by the oxygen half-cell reaction hindered by large overpotentials caused by a complex reaction mechanism involving several bond forming and cleaving steps as well as multiple electron transfer steps. Hence, the utilization of suitable electrocatalysts is necessary to enhance the electrochemical conversion. For the tailored design of electrocatalysts, fundamental insights into catalytic processes as well as the interaction between individual components of the catalytic material are crucial. Therefore, well-defined model systems represent the base for fundamental research in this field. The molecular/atomic structure of the electrocatalyst has a high impact on the surface-dependent electrochemical reaction. Although it is well known that catalytic activity depends on this level on surface properties such as material and morphology, hence electronic properties of the surface. This point is not always addressed when the performance of a catalyst is described.

This thesis focuses on the investigation of earth-abundant transition metal (TM) electrocatalysts involving organic or purely inorganic components which are studied structurally on the molecular scale by scanning tunneling microscopy (STM). Moreover, the chemical composition of the catalyst before and after the reaction and therefore its chemical stability is explored by x-ray spectroscopy (XS). The sample preparation in ultra-high vacuum (UHV) is bridged to ambient electrochemical conditions by a home-built transfer system enabling the analysis of structural stability of the catalyst before and after the reaction by several surface sensitive tools such as STM, low-energy electron diffraction (LEED), x-ray photoelectron spectroscopy (XPS) and x-ray absorption spectroscopy (XAS). The combined approach of complementary real-space imaging and spectroscopic techniques broadens the picture of the electrocatalytic material studied in this thesis. Processes that happen during catalyst synthesis are discussed as well as catalyst stability.

The first part concentrates on TM atoms of Co, Cu and Fe stabilized within an organic environment forming metal-organic coordination networks (MOCNs) which are bifunctionally active towards oxygen evolution reaction (OER) and oxygen reduction reaction (ORR). An on-surface transmetalation reaction is reported that occurs during catalyst preparation. The exchange of Fe/Cu centers by actively deposited Co atoms in a tetraphenylporphyrin (TPP)

network on Au(111) is analyzed by the combined STM-XS approach. Cobalt sublimation onto the metalloporphyrin (MP) network leaves the topography unchanged while the electronic structure of the metal centers is drastically altered. During the redox transmetalation the Fe atom is reduced and expelled from the macrocycle while oxidized Co accommodates within the porphyrin cage. At room temperature (RT) the exchange ratio is of about 50 %. In addition, the experimentally observed exchange is theoretically supported by density functional theory (DFT) calculations leading to possible intermediates and reaction mechanisms. Indeed, the Co center coordinated in the porphyrin macrocycle is more stable than the Fe equivalent. DFT determines a reaction barrier of about 0.2 eV for Co attacking from the top of the Fe porphyrin adsorbed on Au(111) which can be surmounted at RT. In contrast, actively sublimed Fe to the Co porphyrin network leaves the electronic structure unchanged demonstrating that the backreaction is not occurring. Hence, the exchange is thermodynamically driven. The disposability of a second coordination site in the form of a peripheric pyridyl group (tetrapyrroldiporphyrin (TPyP)) is not inhibiting the transmetalation.

The structural and chemical integrity of the monolayered bimetallic Co/Fe TPyP electrocatalyst are investigated for both the ORR and OER. The molecular network catalyzes the ORR successfully demonstrating a higher conversion rate with respect to the Au(111) substrate. Both the local structural integrity of the self-assembled network as well as the chemical stability are confirmed for up to 10 cycles of ORR by STM and XAS. A partial degradation of the porphyrins is detected by STM after 111 cycles. In contrast, the opposite reaction direction (OER) is more aggressive leading to an entirely changed surface structure already after the very first cycle. The potential induced oxidative cleavage of the molecules occurs before driving the OER explaining the high degree of electrochemical stability up to at least 15 OER cycles. The potential induced formation of Co/Fe oxides is determined by XAS. The oxide structures are the actual catalytically active phases for OER.

Subsequently, *in situ* prepared oxide structures are explicitly investigated, starting from monometallic Co cluster on Au(111). The stability in the transfer process between UHV and electrochemical cell is studied. Co cluster are partially oxidized by exposure to 1 bar Ar atmosphere. The oxidation is confirmed by the Co 2p core level measured by XPS. Although the chemical composition changes, the structure of the cluster is reminiscent of the pristine sample. Aqueous solutions like pure water or 0.1 M NaOH promote the oxidation process of Co. Moreover, in aqueous solution cluster are sintering resulting in a changed morphology exemplifying the structural instability. Nonetheless, oxidized Co cluster successfully catalyze the OER reducing the overpotential of Au(111) by approximately 100 mV.

The last chapter focuses on an inorganic approach to stabilize single metal atoms for catalysis. The  $(\sqrt{2} \times \sqrt{2})$  R45° reconstruction of Fe<sub>3</sub>O<sub>4</sub>(001) stabilizes single TM atoms individually in UHV. In a first study the stability of the sensitive  $(\sqrt{2} \times \sqrt{2})$  R45° reconstruction in various environments relevant for electrocatalysis such as Ar, water and 0.1 M NaOH is analyzed by STM, LEED and XPS. The reconstruction persists both Ar and water exposure, but disappears upon contact with 0.1 M NaOH. The absence of the typical reconstruction lines is explained by the formation of a hydroxo complex at the solid-liquid interface. Preliminary experiments

on Ag adatoms/  $\text{Fe}_3\text{O}_4(001)$  leave the ORR unaffected but XPS confirms the stability of the adatoms after ORR.

In conclusion, this thesis demonstrates the importance of catalyst characterization on the molecular and atomic scale. The influence of the potential and the electrolyte on the catalyst structure should not be underestimated and might change the as-synthesized material to the actual active composition which acts as electrocatalyst. Therefore, processes that might prove diametral to catalytic activity, such as the transmetalation reaction, have to be understood and controlled for proper catalyst synthesis. Moreover, detailed knowledge about influencing factors during electrocatalysis on the catalyst enables tailoring of the electrocatalyst towards the reaction requirements. Furthermore, the necessary long term stability of catalysts can be optimized only if underlying processes are understood.

**Key words:** metal-organic coordination network, transmetalation, transition metal electrocatalyst, single atom catalyst, electrocatalysis, oxygen half-cell reaction, oxygen reduction reaction, oxygen evolution reaction, combined STM-XS approach.



# Zusammenfassung

Nachhaltige Energiequellen unterliegen meist starken Produktionsschwankungen. Um Niedrigproduktionszeiten zu überbrücken und eine konstante Energieversorgung zu gewährleisten müssen sie daher mit geeigneten Speichersystemen kombiniert werden. Dies könnte beispielsweise durch eine Energiespeicherung in chemischen Bindungen gewährleistet werden und ist über elektrochemische Umsetzung einfach zugänglich. Der Wasserzyklus, das heißt die Wasserspaltungsreaktion und ihre Rückreaktion, ermöglicht einen ökologischen Prozess, der im Idealfall genug Energie zum Betreiben von elektrischen Geräten zur Verfügung stellt. Limitiert wird der Wasserzyklus allerdings durch das hohe Überpotential der Sauerstoffhalbzellenreaktion, das in ihrem komplexen Reaktionsmechanismus begründet liegt. Dieser Mechanismus beinhaltet einige bindungsbildende und -spaltende Reaktionsschritte, sowie mehrere Elektronenübergänge. Um die elektrochemische Umwandlung zu verbessern, sind daher geeignete Elektrokatalysatoren notwendig. Für die maßgeschneiderte Entwicklung von solchen Elektrokatalysatoren sind grundlegende Einblicke in die katalytischen Prozesse genauso entscheidend wie das Verständnis der Wechselwirkungen der einzelnen Komponenten des katalytischen Materials untereinander. Deshalb bilden klar definierte Modellsysteme die Basis für die Grundlagenforschung in diesem Themengebiet. Die molekulare/atomare Struktur des Elektrokatalysators hat einen starken Einfluss auf die oberflächenabhängige elektrochemische Reaktion. Obwohl die Abhängigkeit der katalytischen Aktivität von Oberflächeneigenschaften wie Material und Morphologie und somit von der elektronischen Struktur bekannt ist, findet dieser Aspekt bislang wenig Beachtung bei der Beschreibung der Leistungsfähigkeit eines Katalysators.

Diese Arbeit befasst sich mit der Erforschung von Elektrokatalysatoren aus Übergangsmetallen, die reichlich auf der Erde vorkommen, unter Einbindung von organischen oder ausschließlich anorganischen Bestandteilen. Strukturell werden sie auf molekularer Ebene mittels Rastertunnelmikroskopie (engl. scanning tunneling microscopy: STM) untersucht. Mit Röntgenspektroskopie (engl. x-ray spectroscopy: XS) wird zusätzlich die chemische Zusammensetzung des Katalysators vor und nach der Reaktion und damit die chemische Stabilität ermittelt. Die Druckdifferenz zwischen der Probenpräparation im Ultrahochvakuum (UHV) und den elektrochemischen Experimenten unter Umgebungsbedingungen wird mittels eines eigens entwickelten Transfersystems überwunden. Dieses erlaubt die Analyse der strukturellen Stabilität des Katalysators vor und nach der Reaktion mit verschiedenen oberflächensensitiven Untersuchungsmethoden wie beispielsweise STM, Beugung niederenergetischer Elektronen (engl. Low-energy electron diffraction: LEED), Röntgenphotoelektronenspektroskopie (engl.

X-ray photoelectron spectroscopy: XPS) und Röntgenabsorptionsspektroskopie (engl. X-ray absorption spectroscopy: XAS). Die Kombination sich ergänzender Messtechniken, wie bildgebende Methoden im Realraum und Spektroskopie, erweitert das Bild vom hier untersuchten elektrokatalytischen Material. Sowohl Prozesse die während der Katalysatorsynthese stattfinden, als auch die Stabilität des Katalysators, werden erörtert.

Der erste Teil dieser Arbeit konzentriert sich auf die Übergangsmetallatome Co, Cu und Fe, die in einer organischen Umgebung unter Bildung von metallorganischen Koordinationsnetzwerken (engl. metal-organic coordination networks: MOCNs) stabilisiert werden und sowohl gegenüber der Sauerstoffreduktion (engl. oxygen reduction reaction: ORR) als auch der Sauerstoffentwicklungsreaktion (engl. oxygen evolution reaction: OER) aktiv sind. Während der Katalysatorsynthese findet eine Transmetallierung auf der Oberfläche statt. Mit dem kombinierten STM-XS-Ansatz wird der Austausch von Fe/Cu-Zentren mit aktiv aufgebrachten Co-Atomen in einem Netzwerk aus Tetraphenylporphyrinen (TPP) auf Au(111) analysiert. Die Kobaltsublimation auf das Netzwerk aus Metallporphyrinen (MP) lässt die Topographie unverändert, wohingegen die elektronische Struktur der Metallzentren sich stark verändert. Während der Redoxtransmetallierung wird das Eisenzentrum reduziert und aus dem Makrozyklus verdrängt. Gleichzeitig nimmt der Porphyrinkäfig das oxidierte Co auf. Bei Raumtemperatur (RT) liegt die Austauschrate bei rund 50 %. Die experimentell beobachteten Ergebnisse werden durch die Dichtefunktionaltheorie (DFT) unterstützt und zeigen dabei mögliche Zwischenzustände und Reaktionsmechanismen auf. Tatsächlich ist ein Co-Zentrum, das im Porphyrin koordiniert ist, stabiler als das eisenhaltige Äquivalent. Zudem berechnet DFT eine Reaktionsbarriere von ungefähr 0,2 eV für ein Co-Atom, das von oben das auf Au(111) adsorbierte Fe-Porphyrin angreift, die demnach bei Raumtemperatur überwunden werden kann. Zu einem Co-Porphyrin-Netzwerk aktiv sublimiertes Fe verändert hingegen nicht dessen elektronische Struktur. Dies beweist, dass die Rückreaktion nicht stattfindet, wodurch die Vermutung einer thermodynamischen Triebkraft für den Austausch naheliegt. Die Verfügbarkeit einer zweiten Koordinationsmöglichkeit in Form von peripherischen Pyridylgruppen (Tetrapyridylporphyrin: TPYP) verhindert den Austausch nicht.

Die strukturelle und chemische Unversehrtheit des einschichtigen, bimetallischen Co/Fe-TPYP-Elektrokatalysators wird für beide Reaktionen, ORR und OER, untersucht. Die höhere Umsatzrate des molekularen Netzwerkes im Vergleich zum Au(111)-Substrat zeigt, dass die ORR am molekularen Netzwerk erfolgreich katalysiert wird. Sowohl die lokale, strukturelle Unversehrtheit als auch die chemische Stabilität des selbst-assemblierten Netzwerkes werden für bis zu zehn ORR-Zyklen mit STM und XAS nachgewiesen. Nach 111 Zyklen zeigen STM-Bilder jedoch einen partiellen Abbau der Porphyrine. Im Gegensatz dazu ist die umgekehrte Reaktionsrichtung, die OER, wesentlich aggressiver und führt bereits nach einem Zyklus zu einer grundlegend abweichenden Oberflächenstruktur. Die potentialinduzierte oxidative Spaltung der Moleküle tritt vor der eigentlichen OER auf. Dies erklärt die hohe elektrochemische Stabilität von bis zu 15 OER-Zyklen. Die potentialinduzierte Bildung von Co/Fe-Oxid wird durch XAS festgestellt. Die Oxidstrukturen bilden die eigentliche katalytisch aktive Phase für die OER.

Im Anschluss werden die *in situ* hergestellten Oxidstrukturen genauer untersucht. Zunächst werden die monometallischen Co-Cluster auf Au(111) auf ihre Stabilität innerhalb des Transfersystems zwischen UHV und der elektrochemischen Zelle überprüft. Die Kobaltcluster sind bereits nach dem Kontakt mit 1 bar Ar teilweise oxidiert. Der oxidierte Zustand wird durch die Messung des Co-2p-Rumpfniveaus mittels XPS bestätigt. Obwohl sich die chemische Zusammensetzung ändert, ähnelt die Clusterstruktur der ursprünglichen Probe. Wässrige Lösung wie reines Wasser oder 0,1 M NaOH fördern den Oxidationsprozess von Co. Zusätzlich sintern die Cluster in wässriger Lösung, sodass sich eine veränderte Morphologie ergibt, die die strukturelle Instabilität verdeutlicht. Dennoch katalysieren die Co-Cluster erfolgreich die OER und verringern das Überpotential von Au(111) um rund 100 mV.

Das letzte Kapitel behandelt einen anorganischen Syntheseweg zur Stabilisierung von einzelnen Metallatomen für die Katalyse. Die  $(\sqrt{2} \times \sqrt{2})$  R45°-Rekonstruktion von Fe<sub>3</sub>O<sub>4</sub>(001) stabilisiert einzelne Übergangsmetallatome im UHV. In der ersten Versuchsreihe wird die Stabilität der sensitiven  $(\sqrt{2} \times \sqrt{2})$  R45°-Rekonstruktion analysiert. Hierfür wird die Probe verschiedenen, für die Elektrokatalyse relevanten, Umgebungen, wie Ar, Wasser und 0,1 M NaOH ausgesetzt und mittels STM, LEED und XPS betrachtet. Die Rekonstruktion überdauert sowohl die Argon- als auch die Wasserexposition, ist aber nach dem Kontakt mit 0,1 M NaOH nicht mehr nachweisbar. Die Abwesenheit der typischen Rekonstruktionslinien wird durch die Bildung eines Hydroxokomplexes an der Schnittstelle zwischen fester und flüssiger Phase erklärt. Erste Voruntersuchungen mit Ag-Adatomen/Fe<sub>3</sub>O<sub>4</sub>(001) verändern die ORR nicht. Die Stabilität der Adatome nach ORR konnte durch XPS bestätigt werden.

Zusammenfassend zeigt diese Arbeit die Bedeutung der Charakterisierung des Katalysators auf molekularer und atomarer Ebene. Der Einfluss des Potentials und des Elektrolyten auf die Struktur des Katalysators sollte nicht unterschätzt werden. Diese Faktoren könnten das synthetisierte Material in die eigentlich aktiven Bestandteile umwandeln, die dann als Elektrokatalysator agiert. Daher sollten Prozesse, die einer optimalen katalytischen Aktivität entgegenstehen könnten, wie beispielsweise die Transmetallierungsreaktion, verstanden und kontrolliert werden, um eine korrekte Katalysatorsynthese zu gewährleisten. Darüber hinaus ermöglicht detailliertes Wissen über die Einflussfaktoren auf den Katalysator während der Elektrokatalyse die Anpassung des Elektrokatalysators an die Reaktionsanforderungen. Die notwendige Langzeitstabilität des Katalysators kann also nur dann optimiert werden, wenn zugrundeliegende Prozesse verstanden sind.

**Stichwörter:** metallorganische Koordinationsnetzwerke, Transmetallierung, Elektrokatalysator aus Übergangsmetallen, Einzelatomkatalysator, Elektrokatalyse, Sauerstoff-Halbzellenreaktion, Sauerstoffreduktion, Sauerstoffentwicklungsreaktion, kombinierter Rastertunnelmikroskop-Röntgenspektroskopie Ansatz.



# Contents

<b>Abstract</b>	<b>i</b>
<b>Zusammenfassung</b>	<b>v</b>
<b>List of Figures</b>	<b>xi</b>
<b>List of Tables</b>	<b>xiii</b>
<b>List of Acronyms</b>	<b>xv</b>
<b>Introduction</b>	<b>1</b>
<b>1 Fundamentals</b>	<b>7</b>
1.1 Electrocatalysis . . . . .	8
1.1.1 The Solid-Liquid Interface . . . . .	8
1.1.2 The Overpotential . . . . .	10
1.1.3 Challenges in Electrocatalysis . . . . .	13
1.2 Oxygen Half-Cell Reaction . . . . .	13
1.3 Analytical Tools . . . . .	15
1.3.1 Scanning Tunneling Microscopy . . . . .	15
1.3.2 X-Ray Spectroscopy . . . . .	17
<b>2 Vacuum Prepared Electrocatalysts: Achievements and Methods</b>	<b>23</b>
2.1 Home-Built Ultra-High Vacuum-Electrochemistry Transfer System . . . . .	24
2.1.1 Transfer by a Vacuum Suitcase . . . . .	25
2.2 2D-Metal-Organic Coordination Networks . . . . .	26
2.3 Molecule-Metal-Substrate Interaction Explaining the Stability of the Catalyst . . . . .	27
2.4 Bimetallic Coordination Network for Oxygen Evolution Reaction . . . . .	31
2.5 Experimental . . . . .	36
2.5.1 Sample Preparation . . . . .	36
2.5.2 Electrochemical Experiment . . . . .	37
2.5.3 Structure Analysis: Sample Preparation and Instrumental Details . . . . .	38
2.5.4 X-Ray Spectroscopy: Instrumental Details and Data Processing . . . . .	39

## Contents

---

<b>3</b>	<b>Metal Exchange in Porphyrins at the Vacuum/Solid Interface</b>	<b>41</b>
3.1	On-Surface Transmetalation of Fe-Tetraphenylporphyrin . . . . .	43
3.2	Mechanism of the Redox Transmetalation in Vacuum . . . . .	48
3.3	Influencing Transmetalation by Pyridyl Peripheric Functional Groups . . . . .	54
3.4	Transmetalation of CuTPyP by Cobalt . . . . .	59
3.5	Conclusion and Outlook . . . . .	60
<b>4</b>	<b>Integrity of a Bifunctional Porphyrin Electrocatalyst</b>	<b>63</b>
4.1	Structural Stability Over Multiple Cycles of Oxygen Reduction Reaction . . . . .	64
4.2	Potential Induced Morphological and Chemical Transformation . . . . .	67
4.3	Conclusion . . . . .	72
<b>5</b>	<b>Chemical and Structural Integrity of a Vacuum-Prepared Co Electrocatalyst</b>	<b>73</b>
5.1	Behavior of the Co Cluster in the Transfer Procedure . . . . .	74
5.2	Oxidized Co Cluster Catalyzing the Oxygen Evolution Reaction . . . . .	76
5.3	Summary . . . . .	78
<b>6</b>	<b>Fundamental Insights into Fe<sub>3</sub>O<sub>4</sub>(001) Utilized as Catalyst Support</b>	<b>79</b>
6.1	From Vacuum to Electrochemical Conditions . . . . .	81
6.2	Decorating Fe <sub>3</sub> O <sub>4</sub> (001) by Ag for Electrocatalysis . . . . .	84
6.3	Summary . . . . .	88
	<b>Conclusion and Outlook</b>	<b>89</b>
	<b>Bibliography</b>	<b>95</b>
	<b>Acknowledgements</b>	<b>113</b>
	<b>Curriculum Vitae</b>	<b>115</b>

# List of Figures

1	Electrochemistry - a simple approach for energy conversion. . . . .	2
1.1	The Gouy-Chapman-Stern model of the electrical double layer. . . . .	9
1.2	Simplified reaction mechanism of the oxygen half-cell reaction in alkaline medium. . . . .	14
1.3	The concept of STM. . . . .	16
1.4	Excitation of core electrons in XPS and exemplary chemical shift. . . . .	18
1.5	Working principle of XAS. . . . .	20
2.1	Scheme of the home-built UHV-EC transfer system. . . . .	24
2.2	Set-up of the vacuum suitcase. . . . .	26
2.3	Self-assembly of metal-organic coordination networks. . . . .	26
2.4	Polymorphism of PBP. . . . .	28
2.5	Fe centers coordinated in a self-assembled PBP network. . . . .	29
2.6	XPS analysis of PBP and PBP+Fe. . . . .	30
2.7	Bifunctional and bimetallic electrocatalyst based on FeTPyP, CoTPyP, Fe and Co. . . . .	32
2.8	Electrochemical stability for OER. . . . .	33
2.9	XPS analysis of the most active bifunctional electrocatalysts: FeTPyP+Co and CoTPyP+Co. . . . .	34
2.10	Fe <sub>3</sub> O <sub>4</sub> (001) exposed to air. . . . .	39
2.11	Exemplary background subtraction of XAS raw data. . . . .	40
3.1	Self-assembled FeTPP network. . . . .	43
3.2	N K-edge of FeTPP and FeTPP+Co. . . . .	44
3.3	Fe and Co L <sub>2,3</sub> -edges of FeTPP and FeTPP+Co. . . . .	45
3.4	XAS of separated polarization directions of FeTPP and FeTPP+Co. . . . .	46
3.5	Superposition of metallic cluster and coordinated metal center. . . . .	47
3.6	Reaction barriers of the transmetalation on Au(111). . . . .	50
3.7	Projected density of states of Fe(Co)TPP and CoTPP+Fe. . . . .	52
3.8	Proposed reaction pathway for the redox transmetalation. . . . .	53
3.9	Effect of the surface on the reaction energy barrier. . . . .	54
3.10	The FeTPyP and FeTPyP+Co network. . . . .	55
3.11	N K-edge of FeTPyP and FeTPyP+Co. . . . .	56
3.12	Fe and Co L <sub>2,3</sub> -edges of FeTPyP and FeTPyP+Co. . . . .	57
3.13	XAS of CoTPyP and CoTPyP+Fe. . . . .	58

## List of Figures

---

3.14	Cu and Co $L_{2,3}$ -edges of CuTPyP and CuTPyP+Co. . . . .	59
4.1	Topographic integrity of FeTPyP+Co depending on the number of ORR cycles. .	65
4.2	N K-edge: XLD of FeTPyP+Co after 10 ORR cycles. . . . .	66
4.3	XAS at Fe and Co $L_{2,3}$ -edges of FeTPyP+Co after 10 ORR cycles. . . . .	67
4.4	Potential induced structural change of FeTPyP+Co. . . . .	68
4.5	OER of FeTPyP+Co and STM image postOER. . . . .	69
4.6	N K-edge of FeTPyP+Co postOER. . . . .	70
4.7	Fe and Co $L_{2,3}$ -edges of FeTPyP+Co postOER. . . . .	71
5.1	Cobalt cluster exposed to different environments of the transfer procedure. . .	75
5.2	Cobalt cluster catalyzing OER. . . . .	77
5.3	Cobalt cluster postOER. . . . .	77
6.1	Model of spinel $Fe_3O_4$ . . . . .	80
6.2	$Fe_3O_4(001)$ exposed to Ar, $H_2O$ and NaOH. . . . .	82
6.3	LEED of $Fe_3O_4(001)$ pre and postNaOH. . . . .	83
6.4	XPS of $Fe_3O_4(001)$ pre and postNaOH. . . . .	84
6.5	ORR of Ag adatoms/ $Fe_3O_4(001)$ . . . . .	85
6.6	XPS of $Fe_3O_4(001)$ decorated by Ag adatoms or multilayer Ag postEC. . . . .	86
6.7	On-surface polymerization via Ullmann-type coupling. . . . .	91
6.8	UHV-prepared 2D Co oxide islands utilized as OER electrocatalyst. . . . .	92
6.9	Schematic flow cell. . . . .	93

## List of Tables

2.1	Experimental details for preparing self-assembled organic networks. . . . .	36
2.2	Parameters of metal co-deposition. . . . .	37
3.1	Calculated energies for different configurations of CoTPP, FeTPP, Co and Fe adsorbed on Au(111). . . . .	49
3.2	Bader analysis of various combinations of CoTPP, FeTPP, Co and Fe. . . . .	51



## List of Acronyms

<b>AO</b>	atomic orbital
<b>BE</b>	binding energy
<b>CoTPP</b>	cobalt tetraphenylporphyrin
<b>CoTPyP</b>	5,10,15,20-tetra(4- pyridyl)21H,23H-porphyrin cobalt(III) chloride
<b>CuTPyP</b>	5,10,15,20-tetra(4- pyridyl)21H,23H-porphyrin copper(III) chloride
<b>CE</b>	counter electrode
<b>CV</b>	cyclic voltammetry
<b>DEMS</b>	differential electrochemical mass spectrometry
<b>DFT</b>	density functional theory
<b>DL</b>	electrical double layer
<b>EC</b>	electrochemistry
<b>fcc</b>	face-centered cubic
<b>FeTPP</b>	5,10,15,20-tetra(4-phenyl)21H,23H-porphyrin iron(III) chloride
<b>FeTPyP</b>	5,10,15,20-tetra(4-pyridyl)21H,23H-porphyrin iron(III) chloride
<b>H<sub>2</sub>TPyP</b>	free-base tetrapyridylporphyrin
<b>HER</b>	hydrogen evolution reaction
<b>iHL</b>	inner Helmholtz layer
<b>LDOS</b>	local density of states
<b>LEED</b>	low-energy electron diffraction
<b>LSV</b>	linear sweep voltammogram

## List of Acronyms

---

<b>MOCN</b>	metal-organic coordination network
<b>MO</b>	molecular orbital
<b>MP</b>	metalloporphyrin
<b>NEXAFS</b>	near-edge x-ray absorption fine structure
<b>OCP</b>	open circuit potential
<b>OER</b>	oxygen evolution reaction
<b>ORR</b>	oxygen reduction reaction
<b>oHL</b>	outer Helmholtz layer
<b>PBP</b>	5,5'-bis(4-pyridyl)(2,2'-bipyrimidine)
<b>PDOS</b>	projected density of states
<b>RE</b>	reference electrode
<b>RT</b>	room temperature
<b>QCM</b>	quartz crystal microbalance
<b>SAC</b>	single atom catalyst
<b>STM</b>	scanning tunneling microscopy
<b>TEY</b>	total electron yield
<b>TM</b>	transition metal
<b>TMA</b>	benzene-1,3,5-tricarboxylic acid
<b>TPP</b>	tetraphenylporphyrin
<b>TPyP</b>	tetrapyridylporphyrin
<b>UHV</b>	ultra-high vacuum
<b>WE</b>	working electrode
<b>XAS</b>	x-ray absorption spectroscopy
<b>XLD</b>	x-ray linear dichroism
<b>XPS</b>	x-ray photoelectron spectroscopy
<b>XS</b>	x-ray spectroscopy

# Introduction

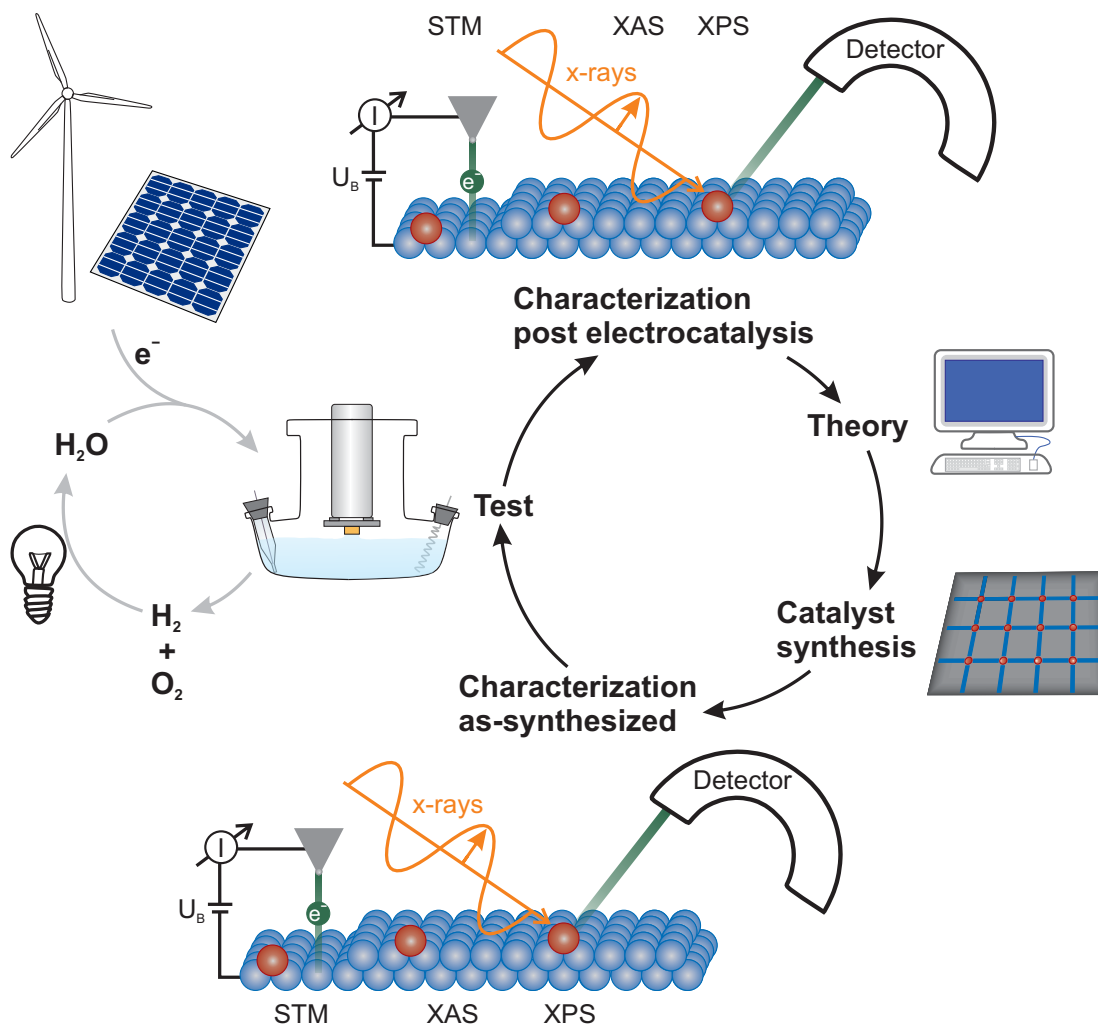
CO<sub>2</sub> induced global warming was first proposed by Svante Arrhenius in 1908<sup>[1]</sup> but was not given much consideration due to the non-immanent consequences. Only in the mid-20th century increasing global mean temperature was varified.<sup>[2,3]</sup> Eventually, new measurement techniques confirmed the long lasting accumulation of CO<sub>2</sub> in the atmosphere responsible for the greenhouse effect. The source of high concentration of CO<sub>2</sub> in the atmosphere is traced back to the combustion of fossil fuels.<sup>[2–5]</sup> Nowadays, first consequences of climate change are reflected by the increasing number and disastrous effects of natural catastrophes such as hurricanes, floods, and contrary weather. Two reasons to abandon the utilization of fossil fuels are their finite availability and the accompanying CO<sub>2</sub> emission. Global energy consumption will not decrease but rather increase. A transition to sustainable energy is needed in order to reduce or even eliminate the production of CO<sub>2</sub> slowing down the climate change. Thus, searching for alternatives mitigating CO<sub>2</sub> production has a high impact on current research.

So far, alternative energy retrieval is incommensurable to fossil fuels because they suffer either of high costs or low efficiency. Nowadays, sustainable energy sources such as wind, water, and sun are already devoted resources. But natural energy sources are intermittent in production resulting in a mismatch of energy demand and supply.<sup>[6]</sup> For compensation of the energy variation, storage systems with a high degree of efficiency are required to compensate low-production times (Fig. 1, grey cycle).

Electrochemistry (EC) offers a facile concept for energy storage and production through the conversion of chemical bonds into energy and vice versa.<sup>[7]</sup> This is a strategy followed also by plants via photosynthesis. Following this route, produced energy can be stored by splitting water into H<sub>2</sub> and O<sub>2</sub> utilizing electrolyzers.<sup>[8–12]</sup> The standard potential of the water cycle ( $\text{H}_2 + \text{O}_2 \rightleftharpoons \text{H}_2\text{O}$ ) is  $E^\circ = 1.23 \text{ V}$ <sup>[13]</sup> promising a combustion cycle with enough energy to drive applications for energy conversion such as fuel cells.<sup>[14,15]</sup> But large kinetic limitations result in high energy losses hindering realization on a large scale. The overall energy loss in an EC reaction is described as overpotential which is the difference between the thermodynamically calculated potential  $E^\circ$  and the applied potential  $E$  to run the device. The water cycle is based on two half-cell reactions. The hydrogen half-cell reaction (alkaline:  $2 \text{H}_2\text{O} + 2 \text{e}^- \rightleftharpoons \text{H}_2 + 2 \text{OH}^-$ ) is a facile reaction with fast kinetics. And the oxygen half-cell reaction (alkaline:  $4 \text{OH}^- \rightleftharpoons \text{O}_2 + 2 \text{H}_2\text{O} + 4 \text{e}^-$ ) is the bottle-neck of the overall water cycle. It is a complex

## Introduction

multi-electron reaction including slow kinetics and involving possibly stable side products which might prevent the final formation of water.<sup>[9,14,16–18]</sup> The best cell potential achieved for electrolyzers is reported at 0.8 V.<sup>[19]</sup> Applications based on the water cycle can only be competitive to fossil fuels when both the overpotential is reduced and the overall reaction rate is sufficiently increased.



**Figure 1:** Electrochemistry - a simple approach for energy conversion. Electrochemical conversion of water using sustainable energy sources like wind or sun is a simple approach to store energy. Driving the reverse direction enables time-delayed energy consumption to compensate energy-strapped (grey cycle). The combination of theory and experiment provides insights into underlying processes promoting the optimization and development of supporting catalysts for applications (black cycle). Explanations: scanning tunneling microscopy (STM), x-ray absorption spectroscopy (XAS), x-ray photoelectron spectroscopy (XPS), bias voltage ( $U_B$ ), current ( $I$ ), electron ( $e^-$ ).

The limitations can be overcome by employing (electro-)catalysts to enhance reactivity and to diminish the overpotential. Catalysts offer an alternative reaction pathway reducing the energy barriers and increasing the reactivity. The best electrocatalysts for the oxygen half-cell reaction are based on noble metals such as Pt<sup>[20–22]</sup>, Ir<sup>[23–26]</sup> and Ru<sup>[23–25,27]</sup>. However, using

precious metals does not solve the problem. Like fossil fuels, they are also limited provoking high production costs. In order to lower the amount of noble metal per device, nanoparticles on cheap substrates such as carbon have been implemented.<sup>[17,27–29]</sup> Moving to the nanoscale approach has two main advantages: first, the significantly reduced amount of catalyst material, and second a higher activity due to quantum size effects and an increased surface area.<sup>[30,31]</sup> Another common strategy is doping the particles with transition metals (TMs) such as Co, Ni and Fe resulting in further enhancement and additionally decreased amount of precious metal.<sup>[14,17,32]</sup>

First row, late TMs show large potential to substitute noble metals entirely in electrocatalysts. Inspired by nature using TM-organic complexes to store and provide energy is one approach to generate earth-abundant, low-cost electrocatalysts.<sup>[33]</sup> For the enhancement of the overall water cycle, the focus lies on improving the multi-step oxygen half-cell reaction which causes mainly the large energy losses. First introduced by Jasinski<sup>[34]</sup>, large complexes such as phthalocyanines or porphyrins demonstrated promising properties for the oxygen half-cell reaction, both in homogeneous<sup>[35–40]</sup> and heterogeneous<sup>[41–43]</sup> catalysis. Using molecular catalysts offers a simple method to change both the electronic and chemical properties by adjusting functional groups and metal centers accordingly going one step closer to a material-by-design approach.<sup>[11,44–46]</sup>

However, molecular catalysts often suffer from stability issues.<sup>[17]</sup> Further heat treatment of these metallocomplexes increases stability and activity.<sup>[47,48]</sup> In this case FeN<sub>4</sub> and FeN<sub>2</sub> moieties or special structures in the altered carbon matrix are assumed to form the active sites.<sup>[49,50]</sup> Indeed, a Fe/N/C containing catalyst outperformed Pt for the first time.<sup>[51]</sup> This breakthrough demonstrates that catalysts of earth-abundant and low-cost materials are no longer a dream.<sup>[17,51]</sup> However, pyrolysis results in undefined structures and compositions of carbides, oxides or intermediate structures disallowing essential understanding of processes for a controlled tailoring of catalysts.<sup>[49]</sup>

A fairly simple approach to create heterogeneous molecular catalysts is based on supramolecular chemistry.<sup>[52]</sup> In this context vacuum prepared self-assembled metal-organic coordination networks (MOCNs) consisting of organic ligands stabilizing individual metal atoms on a conductive surface enable a suitable model system to investigate active sites and mechanisms on the molecular or even atomic scale.<sup>[53,54]</sup> Reducing the complexity of catalytic material to simple model systems provides further investigation of underlying processes involved in electrocatalysis which is crucial to design new materials. For instance, the flat geometry of phthalocyanines and porphyrins allows single molecule studies by scanning probe techniques such as scanning tunneling microscopy (STM) both in ultra-high vacuum (UHV)<sup>[55,56]</sup> and under ambient or even potential controlled conditions<sup>[57,58]</sup>. Sample preparation in UHV enables the stabilization of undercoordinated metal atoms in MOCNs representing a highly reactive single active site.<sup>[59]</sup> Hence, MOCNs have a high potential to be utilized as highly active electrocatalysts. The UHV environment is not comparable to EC but enables a contaminate-free environment to study fundamental reaction steps such as O<sub>2</sub> adsorption.<sup>[55,56]</sup>

Another class of potential catalysts is TM oxides<sup>[11]</sup> which are highly active and diminish the overpotential. In addition, they are stable under the corrosive conditions needed for both fuel cells and electrolyzers.<sup>[60]</sup> TM oxides were studied in detail electrochemically.<sup>[60–67]</sup> However, one drawback is the rather complex structure involving mixed valent states prohibiting an identification of working principles and active sites. Diebold *et al.* realized the investigation of well-defined oxide surfaces in UHV-STM opening also TM oxides to fundamental research on the atomic scale.<sup>[68–71]</sup> Gas dosing experiments in UHV present controlled experiments on the vacuum/solid interface supporting fundamental understanding of processes related to electrocatalysis.<sup>[72,73]</sup>

These manifold challenges to develop new materials and devices for efficient and low-cost energy production in the future requires interdisciplinary collaboration of material science, physics, and (electro-)chemistry (Fig. 1, black cycle).<sup>[19]</sup> Most breakthroughs in electrocatalysis were discovered based on trial- and error experiments. Fundamental insights in processes and relations of both synthesis routes and during catalysis will transform the present approach to a material-by-design approach.<sup>[19]</sup> Understanding and inhibiting undesired synthesis pathways of the catalytically active material is equally crucial for tailored catalysts as a deep knowledge about catalytic processes. Thus, fundamental research is an important base for developing new materials including both information from experiment and theory.<sup>[18]</sup>

The combination of real-space imaging techniques such as STM and the chemical information obtained by x-ray spectroscopy (XS) give complementary insights into catalyst materials. Understanding the complex structure-property relations of catalysts is hardly achievable for real-world catalysts. Here, model systems are a common route to approach the understanding of basic principles. By reducing complexity of the catalytic material or experimental influences fundamental conclusions can be made. Step by step the complexity can be increased in order to eventually bridge the gap between model systems and real world applications.

Catalyst preparation in UHV enables several surface science tools such as STM, x-ray photoelectron spectroscopy (XPS), x-ray absorption spectroscopy (XAS), and low-energy electron diffraction (LEED) giving information about structure, geometry, and chemical environment. Bridging the pressure gap to ambient EC conditions in a controlled way allows the investigation of both stability and active sites. Thus, a transfer system between UHV and EC cell can contribute to clarify principles in electrocatalysis.<sup>[74–76]</sup>

This thesis is based on a UHV-EC transfer system<sup>[77]</sup> enabling the correlation of electrocatalytic performance towards the oxygen half-cell reaction with molecular structure of the catalyst by UHV-STM and its chemical identification by XAS and XPS. The first part focuses on the interaction of single TM atoms with the stabilizing organic matrix and the substrate, for instance Co, Cu and Fe coordinated in a MOCN based on N containing ligands. Furthermore, the connection of metal-molecule-substrate interactions is correlated to the electrocatalytic properties towards the oxygen half-cell reaction in alkaline medium. In the second part,

preliminary results for Co and Fe oxides are presented which are assumed to be of high stability.

In particular this thesis is divided into 6 chapters: **Chapter 1** explains the fundamental concept of electrocatalysis especially referring to the oxygen half-cell reaction. As this thesis follows a multi-technique approach, a brief introduction is given into the utilized analytical tools STM, XPS and XAS. **Chapter 2** illustrates the home-built transfer system enabling the surmounting of the pressure gap between UHV and ambient electrocatalysis. Furthermore, achievements of MOCNs as electrocatalysts for the oxygen half-cell reaction are reviewed. Last, experimental and technical details utilized for sample preparation and characterization throughout this thesis are noted. **Chapter 3** describes the on-surface redox transmetalation process of Fe/Cu-porphyrin by Co co-deposition on Au(111) followed by XAS and supported by density functional theory (DFT). **Chapter 4** investigates the structural and chemical stability of a MOCN based on Fe-porphyrin and co-deposited Co on Au(111) used for oxygen reduction reaction (ORR) and oxygen evolution reaction (OER). **Chapter 5** describes the change of oxidation state and morphology of cobalt cluster/Au(111) induced by the electrolyte contact or the applied EC potential. The cobalt cluster/Au(111) successfully catalyze the OER. **Chapter 6** reports on the utilization of  $\text{Fe}_3\text{O}_4(001)$  as potential substrate for TM-single atom catalyst (SAC). For this purpose  $\text{Fe}_3\text{O}_4(001)$  is investigated in detail by STM, LEED and XPS. Later, preliminary results on  $\text{Fe}_3\text{O}_4(001)$  decorated by Ag adatoms performing ORR are demonstrated. Finally, an outlook will summarize the presented results, gives conclusions and elucidates future strategies.



# 1 Fundamentals

Understanding and optimization of diverse electrocatalytic materials for the oxygen half-cell reaction forms the main topic of this thesis. Following an interdisciplinary approach both electrochemical models and terms are defined as well as working principles of utilized analytical tools.

At first electrocatalysis is defined and a short introduction of developments and findings on the way to the field of electrocatalysis is presented. The particularity of electrocatalysis is based on the solid-liquid interface which plays an important role as the orientation and interaction of reactants and charges influence strongly the overall reaction. Therefore, several models describing the processes at the solid-liquid interface of the electrode surface are illustrated and will facilitate the discussion of the presented results later on.

Catalytic performance is often described by its overpotential which summarizes diverse and complex processes. For a better understanding, general sources and consequences are pointed out. Furthermore, an overview about common challenges in electrocatalysis is enumerated.

The oxygen half-cell reaction is the bottle-neck reaction of the water cycle and will be discussed in detail in this work. Intermediates and reaction pathways need to be taken into account when designing electrocatalysts. For utilized alkaline media, possible reaction pathways involving intermediates and diverse standard potentials are noted. Moreover, specific requirements of the catalytic materials are pointed out.

The designed catalytic material based on nanostructures are characterized carefully and the second part will introduce the utilized analytical tools such as STM, XPS and XAS. For each method a brief explanation of working principles and provided information are explained. The accomplished complementary data enables fundamental insights into the electrocatalysts which are investigated throughout this work and will be discussed in the following chapters.

### 1.1 Electrocatalysis

The fundamentals for EC were already found in 1791 by Luigi Galvani's famous animal electricity.<sup>[78]</sup> Alessandro Volta shortly after generalized Galvani's concept and described the direct correlation of the nature of the electrode and the electrolyte with the measured potential.<sup>[79]</sup> Since then many developments including important theoretical concepts by Faraday<sup>[80]</sup> and Ostwald<sup>[81]</sup> evolved EC as a powerful tool for both analytic chemistry as well as energy conversion. However, the transition from the pure thermodynamic concept to the understanding of kinetic limitations took a long time. The awareness of utilizing (electro-)catalysts to overcome kinetic barriers resulted in the broad research field of electrocatalysis today. In the 1930's the word electrocatalysis was first introduced by Kobosev and Monblanova.<sup>[82]</sup>

A broad description of electrocatalysis is the investigation of electrode reactions in which the kinetics depend on the nature of the interface. In particular the kinetics depend on the electrode material and the double layer formed between electrolyte and electrode.<sup>[19]</sup> The performance can be enhanced by using catalysts on the electrode surface which might act in two ways; first by reducing the overpotential and moving the applied potential closer to the thermodynamic value and second to increase the reaction rate. EC reactions occur on the surface. Even the simplest reaction involves a number of steps including adsorption, electron transfer and desorption. In an ideal case an EC reaction demonstrates a high current density  $j$  close to the equilibrium potential  $E^\circ$ . Before going deeper into the challenges of electrocatalysis we are facing today, the most fundamental aspects are explained. Detailed fundamentals for electrocatalysis and general EC can be studied in Ref.<sup>[83–86]</sup>.

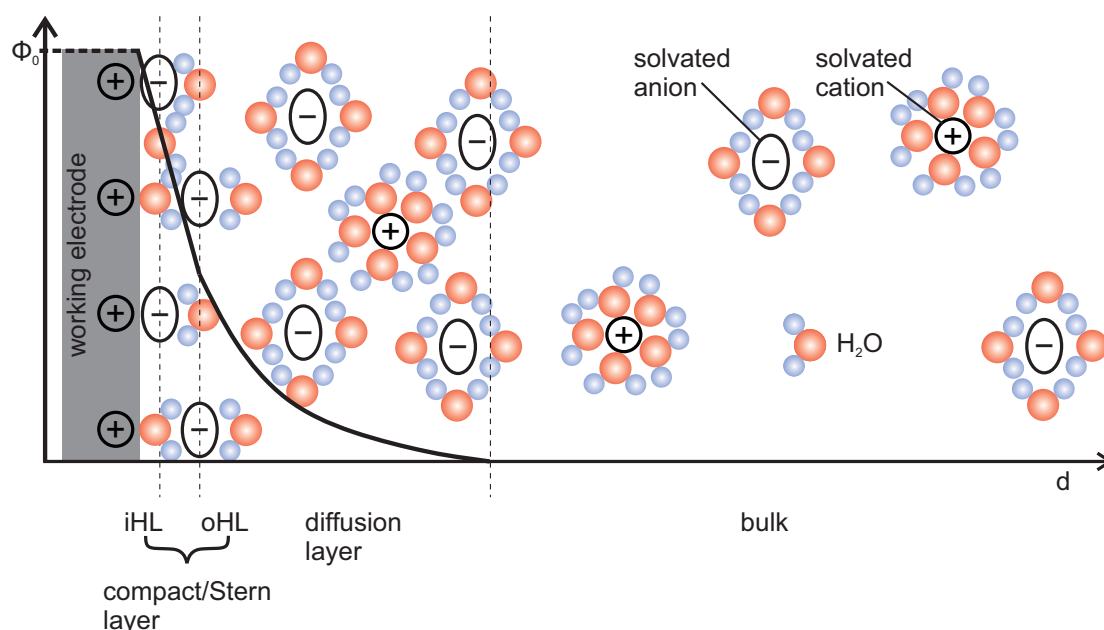
#### 1.1.1 The Solid-Liquid Interface

The heterogeneity of EC reactions explains the importance of the structure of the solid-liquid interface. The polarizability of the electrode and the solid-liquid contact are the two main differences between classic heterogeneous catalysis and electrocatalysis. Nowadays, the solid-liquid interface is modeled as electrical double layer consisting of solvated ions interacting by electrostatic forces with the polarized electrode surface (Fig. 1.1).

The present model, the Gouy-Chapman-Stern model, is based on multiple modifications over the past decades and it is in particular combining two simpler models. The first model was introduced by Helmholtz assuming a compact layer of ions adsorbed on the electrode surface with opposite charge which is known today as inner Helmholtz layer (iHL). The ions are assumed to be adsorbed with partially or completely removed solvation shell. The iHL was extended by the outer Helmholtz layer (oHL) consisting of solvated ions with the same charge as in the iHL. The ion is separated by only one solvated molecule from the electrode surface. Both Helmholtz layers are summarized as the so called Helmholtz or compact layer. Locally the electric potential decays linearly over the whole compact layer which has an estimated size of less than 1 nm. This local Galvani potential  $\phi$  cannot be measured but illustrates the large electric fields dominating at very small distances. The driving force for the electron transfer

promoting the redox reaction is based on the high electric fields at the electrode/electrolyte interface.

The Gouy-Chapman model is the second model included in the Gouy-Chapman-Stern model describing a diffusion layer in front of the electrode. The solvated ions are moving randomly. The ions oppositely charged to the electrode have a higher concentration closer to the electrode surface resulting in a fast, exponential decay of  $\phi$ . The diffusion layer is followed by the bulk electrolyte. Here, both charges equalize. The diffusion and the compact layer can be described as two individual plate capacitors in a series connection determining the overall capacitance of the whole electrical double layer (DL) which is also depicted as plate capacitor in an electrical equivalent circuit.



**Figure 1.1:** The Gouy-Chapman-Stern model of the electrical double layer exemplified at a positively charged working electrode (grey). Cations (+) and anions (−) are solvated by water molecules and interact electrostatically with the charged electrode surface; color code: O (red) and H (blue). Anions adsorb at the electrode surface without solvation shell forming the inner Helmholtz layer (iHL). The outer Helmholtz layer (oHL) consists of anions which are still solvated but electrostatically interacting with the electrode surface. The Galvani potential  $\phi$  decreases linearly in iHL and exponentially in oHL (illustrated in black) with distance  $d$  to the electrode surface starting from the maximum potential  $\phi_0$ . The so-called Helmholtz layer is followed by the diffusion layer where solvated ions are randomly distributed but anions are higher concentrated closer to the surface. Afterwards, the bulk electrolyte is depicted including diluted solvated ions with equal concentration of anions and cations.

When the electrode potential is changed, the DL restructures according to the new conditions causing an electron flow into or out of the electrode. The electron flow causes a measurable current at the external circuit of the EC set-up. This current is not driving any redox reaction and is called a capacitive current which is additive to the faradaic current resulting from an electron transfer driving a redox reaction. Generally for EC experiment the capacitive current should be avoided as it distorts the results. A capacitive current only occurs during

the restructuring immediately after the new potential is applied and decays rapidly once the new structure is formed. Therefore capacitive currents are only apparent in short timescale experiments or at fast scan rates.

In the picture of the DL, the electroactive species has to be within the compact layer to transfer/receive the electron to/from the electrode. The diffusion of the electroactive species into the compact layer also influences the DL. Thus, the kinetics of the electron transfer depends on the structure of the DL. It is obvious that the molecular topography of the electrode influences the layer of adsorbed ions. Therefore, knowing the electrode surface on the molecular scale allows for a deeper understanding of the DL region including possible limitations or promoters. However, for adsorbing, desorbing and intermediate formation not only the structure of the surface, but also the nature of the involved atoms are important. These reaction steps require additional energy and are summarized in the term overpotential.

### 1.1.2 The Overpotential

The overpotential represents a complex, multi-step process influencing the kinetics of an EC reaction. It combines many different types of processes restraining the reaction.

In the simplest case the reactant adsorbs at the electrode surface within the compact layer followed by an electron transfer and eventually desorption of the product from the surface. Therefore, the reaction depends on the diffusion of the reactant to the electrode surface, the adsorption possibility at the electrode, the probability of electron transfer, followed by several bond cleavage or formation processes (summarized as chemical reactions), the desorption energy and eventually the diffusion of the product into the bulk. The slowest of all individual steps defines the rate of the conversion (rate determining step). The overpotential  $\eta$  is the potential difference between the actual applied potential  $E$  at the cell and the corresponding equilibrium potential  $E^\circ$  for the experimental conditions (Equ. 1.1).

$$\eta = E - E^\circ \quad (1.1)$$

The overpotential can be subdivided according to the main contributions to the EC reaction: mass transfer, electron transfer, and chemical reaction including adsorption/desorption processes.

#### Mass Transfer

The mass transfer is responsible for sufficient reactant concentration at the solid-liquid interface. The reaction rate can only be maximized if enough reactants are provided at the electrode surface. The same is true for products which have to be transported into the bulk efficiently to

leave the active sites. Three types of mass transfer are differentiated: migration, convection and diffusion. Typically, diffusion is used for mass transfer in EC and can be influenced by the potential gradient in the cell. The mass transfer based on diffusion can be enhanced by increasing the electrode potential by the mass transfer overpotential  $\eta_{mt}$ .

### Electron Transfer

Among all different types of overpotentials, the electron transfer overpotential  $\eta_{et}$  contributes always. At the thermodynamic equilibrium  $E^\circ$ , no overpotential is required to drive the redox reaction. Moreover, the reduction and the oxidation reaction of a redox couple ( $O + ne^- \rightleftharpoons R$ ) show equal reaction rates and zero current density. The  $E^\circ$  is only determined by the nature of the redox couple ( $O, R$ ) and the bulk concentration of the oxidized ( $C_O$ ) and the reduced species ( $C_R$ ) according to Nernst equation:

$$E = E^\circ + \frac{2.3RT}{nF} \log \frac{C_O}{C_R} \quad (1.2)$$

The Nernst equation describes also the dependence on the temperature  $T$  and the number of transferred electrons  $n$ . And it involves additionally the gas constant  $R$  and Faraday constant  $F$ . When applying an overpotential at the electrode the reaction rate at one electrode is increased while the counter reaction is reduced. As a result a current flows over the external circuit giving a direct measure for the occurrence of product formation.

Electron transfer occurs at the electrode/electrolyte interface by a quantum mechanical tunneling process. For tunneling the reactant has to be either adsorbed at the electrode surface or at least within the compact layer of the DL. The principles for electron transfer kinetics are described by a dependence of the current density with the overpotential applied to the cell. The current density is directly related to the number of active sites per geometric area and the velocity of the reaction from reactant to product. Therefore, the two most important parameters to describe catalytic performance, are  $j$  and  $\eta$ .

For small overpotentials, the Butler-Volmer equation (Equ. 1.3) is valid: Butler-Volmer describes the relation of the current density  $j$ , measured at the working electrode (WE) and the exchange current  $j_0$  with the total overpotential  $\eta$  through the transfer coefficient  $\alpha$ . Additionally, Faraday constant  $F$ , gas constant  $R$ , the number of transferred electron  $n$ , and the temperature  $T$  are involved.

$$j = j_0 \left[ \exp \left( \frac{\alpha n F \eta}{RT} \right) - \exp \left( - \frac{\alpha n F \eta}{RT} \right) \right] \quad (1.3)$$

## Chapter 1. Fundamentals

---

In experimental devices, generally, high overpotentials are applied to generate sufficient exchange currents.<sup>[87]</sup> In this case the Tafel equation is more valid involving the same parameters as in equation (1.3).

$$\log j = \log j_0 + \frac{\alpha n F}{2.3 R T} \eta \quad (1.4)$$

The Tafel slope can be used to extract information about reaction mechanisms. For this purpose,  $\log j$  vs. the  $\eta$  is plotted. The concept of the Butler-Volmer and Tafel relation is further described in Ref.<sup>[83–86]</sup>.

### Chemical Reactions

The kinetics of an EC reaction might be further hindered by reorganization of the molecule after the electron transfer resulting in an overpotential of chemical reactions  $\eta_{chem}$ . Usually, the first molecular structure after the electron transfer is unstable and further energy is needed to run bond formation and cleavage following chemical reactions. Moreover, the adsorption process requires overlapping orbitals of the electrode with the reactant which might cause also higher energy for the overall reaction. The same is valid for desorption of the product.

In summary, the topic of overpotential is complex and only a few general aspects were described. The actual measured or applied overpotential is always a convolution of all different types and is hard to decompose into its separate contributing factors:

$$\eta_{total} = \eta_{mt} + \eta_{et} + \eta_{chem} \quad (1.5)$$

For energy conversion, the redox reaction should not be in equilibrium. Hence, always a minimum overpotential to push the reaction towards the desired product is required. When talking about efficiency of a technical device, discussing exclusively the activation overpotential is not sufficient. The activation overpotential describes the total overpotential applied in addition to the  $E^\circ$  to move the reaction out of equilibrium and to produce a current. Generally, the current is too small to run technical devices efficiently. Thus, additional overpotential is applied to support the reaction rate.  $\eta_{total}$ , especially the  $\eta_{et}$  and the  $\eta_{chem}$  can be minimized by using electrocatalysts. By gaining fundamental insights into involved processes on the molecular scale, it is possible to understand limitations and tailor the electrocatalyst towards the requirements.

### 1.1.3 Challenges in Electrocatalysis

The overall goal of an electrocatalyst is offering a novel reaction pathway requiring a small activation energy by stabilizing adsorbates at an optimum. If compounds adsorb strongly, they block active sites which is commonly described as poisoning. The kinetics and the reaction mechanism might depend on the chemical composition and even on the shape of the electrocatalyst. In the case of electrocatalysis the catalyst is the electrode surface. The role of adsorbates, both intermediates and products, is crucial for life time and energy loss i.e. overpotential. An optimal support requires an overlap of the electronic levels of the catalyst and the adsorbate resulting in optimal strength of surface-adsorbate bonds. The optimization of the adsorption energy of each intermediate causes a trade-off because optimization of individual steps influences always the other steps. Understanding the activity of particular surface sites is crucial for tailoring electrocatalysts. This concept also includes insight into the effect of neighboring active sites and their size.

The current density  $j$  could be influenced, for instance, by a higher surface area which increases the number of active sites as long as they are still available for reactants. Due to the direct correlation of active sites and  $j$ , the strategy results in an enhanced conversion of reactant to product. The higher surface area should not be confused with limited mass transport of the reactants to the surface which is only depending on the geometric area. Nevertheless, mass transfer limitations could also occur but cannot be influenced by the catalyst. Some reactions are limited by competing reactions occurring at similar potentials. Hence, the catalyst needs to provide selectivity to the desired product.

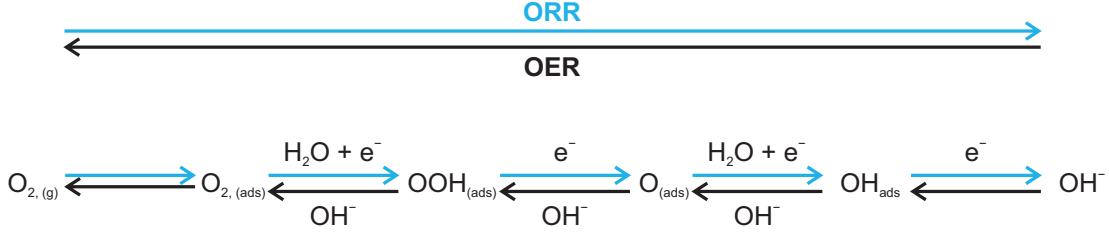
These considerations give only an overview of requirements when designing an electrocatalyst. Most often, they are not easily applied in the experiment. Of course when talking about implementing electrocatalyst in applications numerous challenges in addition need to be considered.

## 1.2 Oxygen Half-Cell Reaction

The oxygen half-cell reaction is the limiting factor for efficient electrolyzers and fuel cells. The numerous reaction steps involving four electron, four proton transfer and several bond formation and cleavage steps explains its high complexity. The reaction is limited by sluggish kinetics requiring high overpotentials. In order to reduce the energy losses of the whole water cycle, the oxygen half-cell reaction kinetics need to be improved by suitable electrocatalysts. The investigation of fundamental aspects of electrocatalysts for the oxygen half-cell reaction is crucial for future improvements and represents an important aspect of this thesis. Thus, the reaction mechanisms and intermediates are specified.

Although OER and ORR are opposite reactions the requirements of the electrocatalyst are entirely different exemplified by the different materials supporting most efficiently the two reaction directions. While Pt catalyzes ORR efficiently,<sup>[20–22]</sup> the OER is catalyzed best by

noble oxides such as  $\text{IrO}_2$  [23–26] and  $\text{RuO}_2$  [23–25,27]. As pointed out earlier, the reaction involves multiple intermediates. A simplified reaction scheme for an associative mechanism in alkaline medium is depicted in Fig. 1.2. The scheme illustrates the multiple bond forming and breaking steps going along with several electron transfers.



**Figure 1.2:** Simplified reaction mechanism of the oxygen half-cell reaction in alkaline medium. ORR (blue); OER (black); indices: gaseous (g), species adsorbed on the surface (ads).

It becomes clear that many different pre and post structural changes of the reactant as well as multiple adsorption and desorption processes are involved. It is well known that the binding energy (BE) of the intermediates are crucial for the kinetics. For instance ORR is either limited by the formation of  $\text{OOH}_{(ads)}$  or the desorption of  $\text{OH}_{(ads)}$ ,<sup>[88]</sup> whereas the OER is either limited by a strong adsorption of  $\text{OOH}_{(ads)}$  or a weak binding of  $\text{OH}_{(ads)}$ .<sup>[89]</sup> A deep understanding of the on-going mechanisms is crucial to tailor electrocatalysts to efficiency. However, the investigation of individual processes, intermediates and kinetics is difficult and even with spectroelectrochemical data ambitious. Moreover, mechanisms highly depend on electrode material disallowing general conclusions.

The overall reaction equations including  $E^\circ$  are listed in the following.<sup>[90]</sup>

The preferable direct 4- $\text{e}^-$ -mechanism:



The (2+2)- $\text{e}^-$ -mechanism involving  $\text{H}_2\text{O}_2$  (alkaline:  $\text{HO}_2^-$ ) as side product:



Additionally  $\text{H}_2\text{O}_2$  (alkaline:  $\text{HO}_2^-$ ) might disproportionate according:



While for the ORR  $\text{H}_2\text{O}_2$  can be the final product demonstrating an unsuitable electrocatalyst,  $\text{H}_2\text{O}_2$  will always further react to  $\text{O}_2$  in OER. The mentioned differences already explain why different requirements of the electrocatalyst are needed for the two reactions. In some technical devices such as metal-air batteries both reactions need to perform at the same electrode presenting an additional challenge for the electrode material.

### 1.3 Analytical Tools

Fundamental insights in electrocatalysis have to be addressed by multiple analytical tools. The molecular structure of the electrocatalyst contributes heavily to the catalytic performance. STM provides molecular or even atomic resolution which illuminates the structure of the prepared electrocatalyst. As imaging technique, STM probes both the structure of as-prepared electrocatalysts as well as postEC. However, STM is not chemical sensitive, hence it is combined with XS in particular XPS and XAS. XS is a non-local technique averaging over large sample areas providing also from that perspective complementary insights. The basic principles of STM, XPS and XAS are explained in the following.

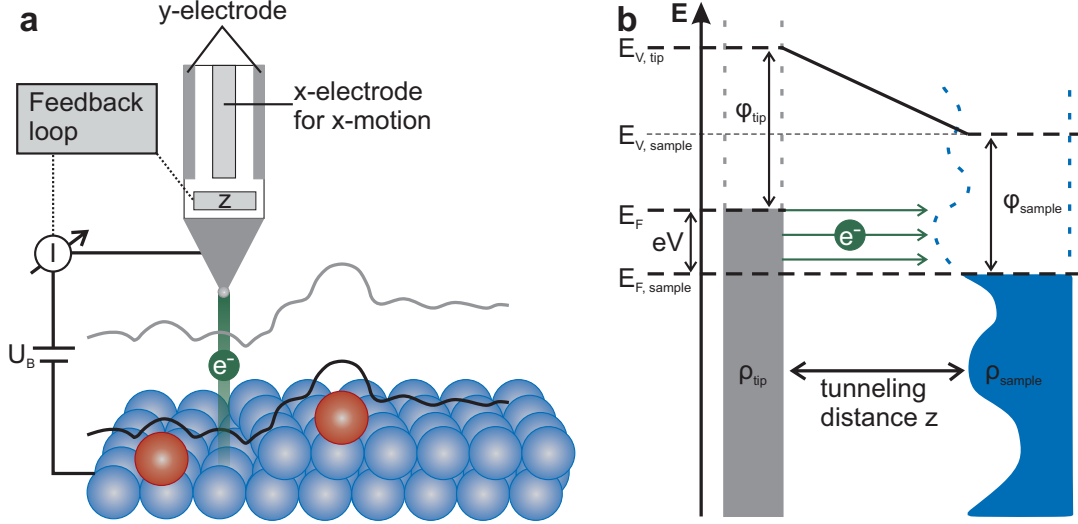
#### 1.3.1 Scanning Tunneling Microscopy

Based on the quantum mechanic tunneling effect, Binnig and Rohrer built the first STM in 1982.<sup>[91]</sup> The STM is a real space imaging technique enabling atomic resolution on conductive samples representing a milestone for surface science and was awarded with the Nobel prize in 1986.<sup>[92]</sup>

Quantum tunneling allows particles, described as wave functions, to pass a potential barrier or insulating gap. In the gap, the wave function decays exponentially resulting in a wave function with a reduced amplitude on the other side of the barrier. A sharp metallic tip is brought in close proximity to a conductive surface by piezo electrics having a precision of a few Ångström (Fig. 1.3 a). Between tip and sample a bias voltage  $U_B$  is applied shifting the Fermi level  $E_F$  against each other driving the tunnel current  $I$  in one direction (Fig. 1.3 b).

In order to obtain information about a surface area the tip is scanned by piezo electrics across the surface (Fig. 1.3 a). There are two operation modes: constant-height and constant-current. The latter mode has been used throughout this work. In constant-height mode the distance between tip and sample is kept constant and the measured tunnel current  $I$  is amplified and provides the information for the STM image. This mode is suitable for small and flat areas because the tip is located closely to the surface without distance adjustment. The constant-height mode works without a feedback loop enabling fast scanning. In contrast, the constant-current mode holds the tunnel current constant by adjusting the tip-sample distance. Hence, the tunnel current works as input for the feedback loop of the z-piezo controller. The image is generated from the z-movements of the tip. The scan velocity is limited by the

feedback loop adjusting the tip-sample distance. However, the distance adjustment enables scanning of large and rough areas.



**Figure 1.3:** The concept of STM. (a) Schematic picture of a sharp metal tip scanning over a conductive surface. Between tip and sample a bias voltage  $U_B$  is applied. For scanning, the tip is moved by piezo electrics controlled by four electrodes responsible for x- and y-motion. Depending on the scan mode, the feedback loop controls the tip-sample distance through the z-piezo (feedback loop on: constant current, off: constant-height). Depending on the mode, z-movements or tunnel current  $I$ , are input for the generated image. (b) Simplified picture of tunneling between tip and sample. Tip and sample have shifted Fermi levels due to an applied bias voltage ( $U_B$ ):  $E_F, E_{F, sample}$ , respectively. The tunnel current  $I$  is illustrated as green arrows demonstrating the tunneling direction from the tip to the sample. Further parameters are: LDOS of tip  $\rho_{tip}$  (grey) and sample  $\rho_{sample}$  (blue), the equivalent vacuum levels  $E_{V, tip}$  and  $E_{V, sample}$ , and the work functions  $\phi_{tip}$  and  $\phi_{sample}$ .

The tunnel current  $I$  between tip and sample is described by the Tersoff-Hamann model<sup>[93,94]</sup> based on Bardeen's theory<sup>[95]</sup>. The model makes several assumptions, namely: thermal equilibrium of tip and sample at 0 K, a low bias voltage  $U_B$ , and the tip is terminated by only one spherical atom providing only s-states. The model correlates the tunnel current  $I(U)$  to the LDOS of the tip  $\rho_t$  and the sample  $\rho_s(x, y)$  explaining the complexity of interpretation as the image cannot be exclusively referred to topographic effects.

$$I(U, x, y, z) \propto \exp\left(-2z\sqrt{\frac{2m_e}{\hbar^2}\phi}\right) \int_0^{U_B} dE \rho_s(E, x, y) \rho_t(E - eV) \quad (1.10)$$

The picture of a metallic tip terminated with only one atom also explains the atomic resolution as the tunneling current decays exponentially with distance  $z$  visible from the exponential prefactor in equation (1.10). The prefactor describes the matrix element with the merged work function  $\phi$  of tip and sample generally unknown in the experimental set-up, the mass

of a single electron  $m_e$ , and  $\hbar$  which is Planck's constant  $h$  divided by  $2\pi$ . A more detailed description of STM and the underlying theoretical concepts are given in Ref. [96,97]

### 1.3.2 X-Ray Spectroscopy

Spectroscopic techniques based on x-ray irradiation offer information about chemical compounds, orientation on the surface and conformation. Depending on the precise detection method oxidation states as well as electronic structure can be identified. Contrary to STM providing local information on the atomic scale, XS averages over macroscopic areas. The information of both methods is complementary and a combined approach completes the picture of the catalyst. Two main spectroscopic techniques are used to characterize samples: XPS and XAS. In both cases, the measured information is collected by electrons in total yield mode and therefore both techniques probe only the surface and surface-near regions of the sample.

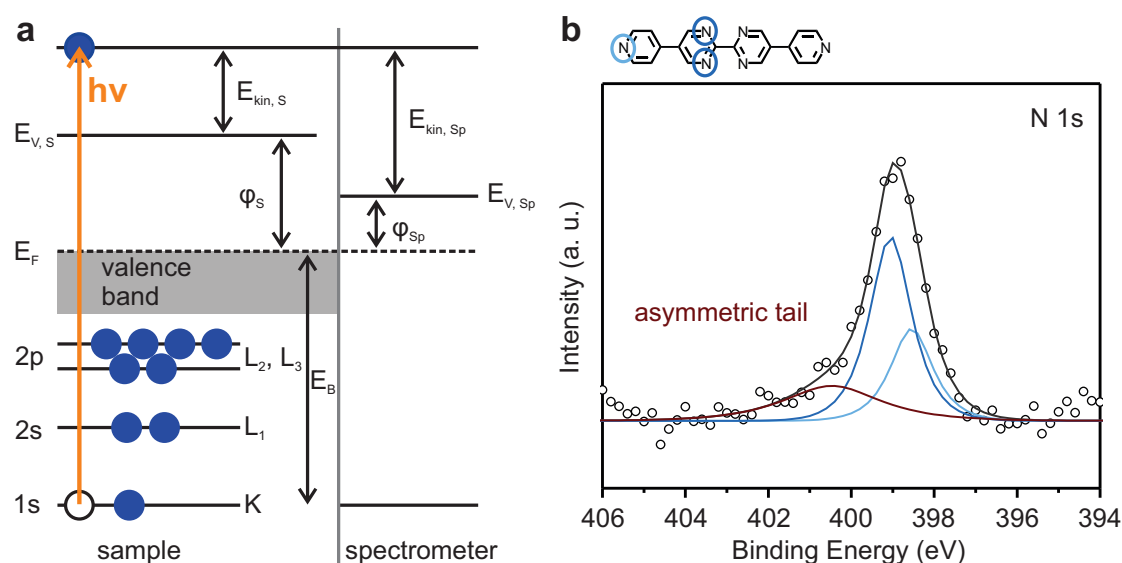
#### X-Ray Photoelectron Spectroscopy

XPS is based on the photoelectric effect which was first discovered by Rudolf Hertz in 1887. [98] In 1905, the effect was explained by Albert Einstein and awarded with the Nobel prize in 1921. [99] The photoelectric effect describes the electron emission from a solid upon light irradiation. For XPS, x-rays are either generated from a lab source providing either Al or Mg  $K\alpha$  lines with an energy of 1487.0 eV and 1253.6 eV, respectively. Alternatively, a broad energy synchrotron x-ray source can be applied having the advantage of adjustable excitation energy. Variable photon energy enables higher yield of photoelectrons resulting in a more detailed sample analysis.

The energy of an incident x-ray photon excites a core level electron to the vacuum level declared as photoelectron (Fig. 1.4 a). The core level energies of different elements are energetically distinct explaining the element specificity provided by XPS. Emitted photoelectrons can only leave the sample from a maximum depth of a few nanometers because of the inelastic mean free path limiting the amount of detected photoelectrons. Hence, XPS is surface sensitive although x-rays penetrate further than only the outmost layers. Using synchrotron sources the inelastic mean free path can be adjusted decreasing the measuring volume to several Ångström. As a consequence the surface sensitivity is enhanced.

The kinetic energy of the photoelectron  $E_{kin}$  is determined by the energy of the photon  $h\nu$ , involving Planck's constant  $h$  and the frequency of the photon  $\nu$ , subtracted by the work function of the sample  $\varphi_S$  and the binding energy of the photoelectron  $E_B$  in the core according to:

$$E_{kin} = h\nu - \varphi_S - E_B \quad (1.11)$$



**Figure 1.4:** Excitation of core electrons in XPS and exemplary chemical shift. (a) The incident x-ray of an energy  $h\nu$  excites a photoelectron with a binding energy  $E_B$ . The emitted photoelectron travels with a kinetic energy  $E_{kin,S}$ . Sample and spectrometer are in electrical contact with equalized Fermi level  $E_F$ . Further parameters: the work function of the sample  $\varphi_S$  and the spectrometer  $\varphi_{Sp}$ , the vacuum level of the sample  $E_{V,S}$  and the spectrometer  $E_{V,Sp}$ . The spectrometer detects the kinetic energy  $E_{kin,Sp}$  of the emitted photoelectrons. (b) Exemplary chemical shift at a N 1s core level of 5,5'-bis(4-pyridyl)(2,2'-bipiridine) (PBP) (structural formula is shown on the top).<sup>[100]</sup> The different N components presented as pyridyl N (light blue) and pyrimidyl N (dark blue) in the molecule demonstrate diverse binding energies due to their different chemical environment. The convolution of all N components form the shape and intensity of the overall N 1s peak. The dotted plot represents the measured spectrum while the solid line demonstrates the fit function. The red curve adjusts the fit function according to its asymmetric tail and is not related to an additional N component.

In an experimental set-up the kinetic energy of the emitted photoelectrons is detected in the spectrometer characterized by its own work function  $\varphi_{Sp}$  resulting in a measured kinetic energy  $E_{kin,sp}$  of the photon differing from the actual  $E_{kin,s}$  of the emitted photoelectron. Due to the electrical contact between sample and spectrometer the Fermi level  $E_F$  of both are equal. Therefore, the sum of equivalent work function and kinetic energy is identical and actual kinetic energy  $E_{kin,s}$  of the photoelectron of the sample can be determined.

XPS is sensitive to the chemical environment, although core and not valence states are probed. Core levels are strongly influenced by the valence electrons resulting in a so called chemical shift of the core level energies (Fig. 1.4 b). An element exposed to diverse chemical environments is represented as a signal with different contributions consisting of the individual shifted peaks. By exploiting peak positions and intensity ratios of the individual contributions, physico-chemical properties can be investigated.

### X-Ray Absorption Spectroscopy

XAS complements information provided by XPS which is limited to chemical environment and oxidation states. In contrast, XAS investigates the orientation on the surface as well as the electronic structure of the element. In XPS the excitation energy  $h\nu$  is held fixed, whereas in XAS the energy is constantly shifted during the measurement. In order to achieve broad and intense energy band of x-rays, a synchrotron source is needed. The exciting x-ray beam is monochromatized and linearly polarized.

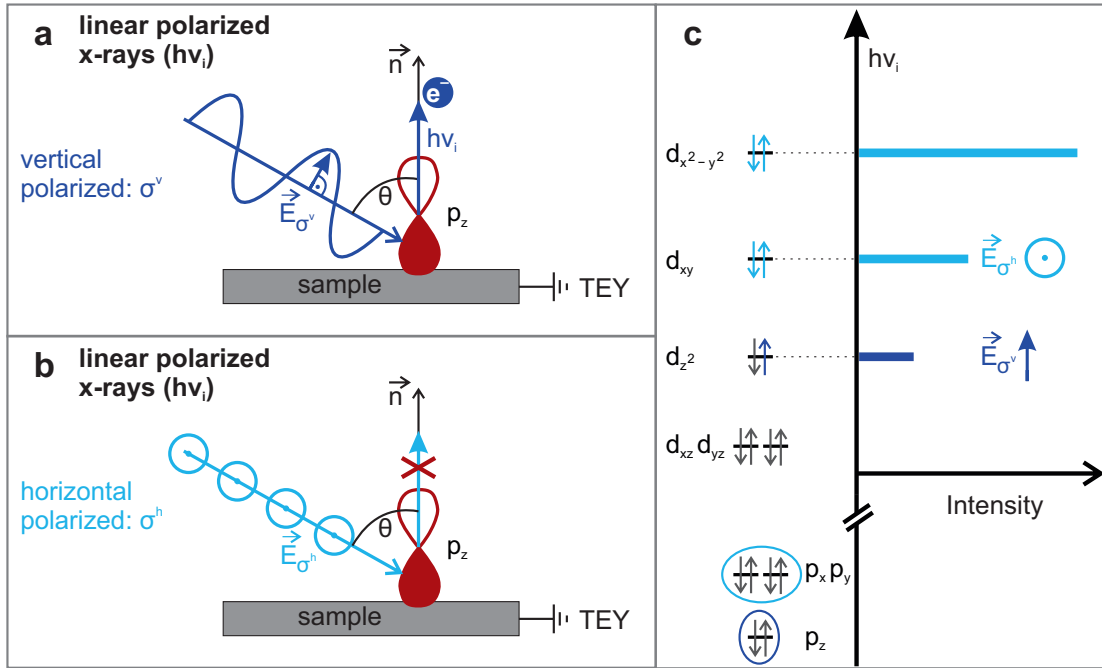
XAS probes the excitation from occupied states to empty valence states. In the following the  $L_{2,3}$  absorption edge is discussed describing a transition from 2p core levels to empty 3d orbitals. The detection is performed by total electron yield (TEY). The core hole, induced by the excitation of the electron, is refilled by multiple decay mechanisms resulting in Auger processes. As primary Auger electrons leave the sample, they induce several secondary electron scattering which dominate the TEY. Due to a limited mean free path of the secondary electrons within the sample, only the surface and surface near regions are measured explaining the surface sensitivity of the technique.

The excitation follows a dipole transition described by Fermi's golden rule.<sup>[101,102]</sup> Quadrupole transitions are weak in XAS and can be neglected in most cases. The sensitivity towards orientation as well as electronic structure of XAS becomes clear when looking at the transition probability based on Fermi's golden rule<sup>[101,102]</sup> proportional to the measured intensity  $I$ :

$$I_{XAS} \propto |\langle \phi_f | \vec{E} \cdot \vec{r} | \phi_i \rangle|^2 \delta_{E_f - E_i - h\nu} \quad (1.12)$$

The intensity  $I_{XAS}$  is proportional to the dipole matrix element or dipole operator  $\vec{E} \cdot \vec{r}$  consisting of the electric field vector  $\vec{E}$  and the position operator  $\vec{r}$  which connects the initial  $\phi_i$  and final state  $\phi_f$ . The dipole operator defines the selection rule limiting the transition to an orbital momentum difference of 1 ( $\Delta L = \pm 1$ ) and a constant spin momentum ( $\Delta S = 0$ ). The delta function  $\delta_{E_f - E_i - h\nu}$  ensures the energy conservation of the transition. The matrix element shows the dependence of the transition on the electric field vector  $\vec{E}$  giving rise to the geometric information as well as the electronic structure. Linear polarized light has a restricted  $\vec{E}$  in one plane.  $\vec{E}$  can be changed by either turning the sample in respect to the incident x-ray beam by adjusting the angle  $\theta$  between the incident x-ray beam and the surface normal vector  $\vec{n}$ , typically done for near-edge x-ray absorption fine structure (NEXAFS), or by changing the direction of the linear polarization (Fig. 1.5 a, b).

In the presented experiments a measuring geometry of grazing incident ( $\theta = 60^\circ$ ) and two different linear polarization directions are used: vertical polarization  $\sigma^v$ , out-of-plane ( $90^\circ$ ), and horizontal polarization  $\sigma^h$ , in-plane ( $0^\circ$ ).



**Figure 1.5:** Working principle of XAS. The monochromatized and linear polarized x-ray beam incidences with an energy of  $h\nu_i$  at an angle  $\theta$  on the sample. A  $p_z$  orbital (red) oriented along the normal vector  $\vec{n}$  represents an exemplary initial state. (a) X-rays are vertical polarized ( $\sigma^v$ ) with an electric field vector  $\vec{E}_{\sigma^v}$  resulting in excitation of a core electron from the  $p_z$  orbital. (b) Horizontal polarized x-rays ( $\sigma^h$ ) with an electric field vector  $\vec{E}_{\sigma^h}$  oriented parallel to the sample surface. The transition probability from the  $p_z$  orbital is zero. (c) The sensitivity of XAS on electronic anisotropy explained at an exemplary  $L_{2,3}$  transition (2p core electrons to 3d empty valence states). Initial distribution of electrons through p and d orbitals is depicted by grey arrows (electrons) based on the ligand field of a square planar complex. Depending on the electric field vector of the linear polarized light  $\vec{E}$ , certain initial states are available: vertical polarized  $\sigma^v$  (encircled dark blue), horizontal polarized  $\sigma^h$  (encircled light blue). Excitation occurs in different d levels depending on the polarization direction and number of empty states. Possible final states for the individual polarization directions are labeled by dark blue arrows for  $\sigma^v$  and light blue arrows for  $\sigma^h$ . The intensity variation as a result of the diverse transition probabilities is demonstrated as bar diagram with similar color code on the right side.

Using a 60° angle of incidence for  $\sigma^v$  results in a limited transition probability due to non-optimized geometric alignment of  $\vec{E}$  with the orientation of the  $p_z$  orbital in this case along the normal vector  $\vec{n}$  (Fig. 1.5 a). The orientation of  $\vec{E}$  and the normal vector  $\vec{n}$  can be described as  $\vec{E} \cdot \sin\theta \parallel \vec{n}$  (Fig. 1.5 a). Optimal transition occurs when  $\vec{E} \parallel \vec{n}$ . However, experimental limitations disallow a perfect positioning of  $\vec{E}$  and  $\vec{n}$ . As a result, the measured intensity is lower and scales with  $\sin\theta$ . In contrast, the  $\vec{E}$  of  $\sigma^h$  is perpendicular to the orientation of  $p_z$  independent of the angle of incidence prohibiting an electron excitation (Fig. 1.5 b).

The sensitivity towards the electronic structure becomes clear by considering an exemplary metal center exposed to a square planar ligand field, for instance, in a metal-organic complex (Fig. 1.5 c). In this case, atomic orbitals (AOs) are probed by incidental x-rays. The transition probability depends on the orientation of the AOs of the initial and the final state. For instance,

$\sigma^h$  excites electrons from  $p_x$  or  $p_y$  orbital (light blue circle) to  $d_{xy}$  or  $d_{x^2-y^2}$  orbital (final state electrons symbolized by light blue arrows). While  $\sigma^v$  drives a transition from  $p_z$  orbital (dark blue circle) to  $d_{z^2}$  orbital (dark blue arrows symbolize the electrons in the final state). The final states have different occupation possibilities resulting in diverse transition probabilities measured as different intensities (Fig. 1.5 c, bar diagram on the right). The XAS shape is a linear combination of all individual species involved at this specific energy giving rise to typical multiplet structures which can be interpreted using several theoretical approaches.

Forming the dichroism (x-ray linear dichroism (XLD) =  $\sigma^h - \sigma^v$ ) of the two polarization directions demonstrates the system's anisotropy in electronic structure or orientation. The grazing incidence configuration implies that the measured anisotropy is always smaller than the real one due to the reduced signal of  $\sigma^v$ .



## 2 Vacuum Prepared Electrocatalysts: Achievements and Methods

Synthesizing electrocatalysts in UHV enables a controlled and clean procedure as well as a variety of surface sensitive characterization tools. Furthermore, vacuum allows different preparation strategies compared to classical wet-chemistry methods such as sublimation. This concept allows, for instance, the stabilization of undercoordinated highly reactive metal centers, and materials which are not accessible within solvents.<sup>[59]</sup> The preparation in UHV requires a sophisticated set-up to overcome the pressure gap between UHV and ambient conditions for electrocatalysis. Our home-built transfer system provides a tool for surmounting the pressure difference in a controlled way.<sup>[77]</sup> The details of the set-up will be described below.

UHV prepared MOCN have the advantage of easy supply of undercoordinated and as such highly reactive individual metal atoms. MOCNs offer a new class of catalytic material which will be explored in this work. The variety of the toolbox provided by MOCN for tailoring electrocatalysts will be elaborated further down. The combination of UHV preparation and real-world electrocatalysis is not widespread but some achievements were documented and will be displayed below. In particular two different MOCNs based on N containing organic ligands namely PBP and metalloporphyrins (MPs) are discussed.

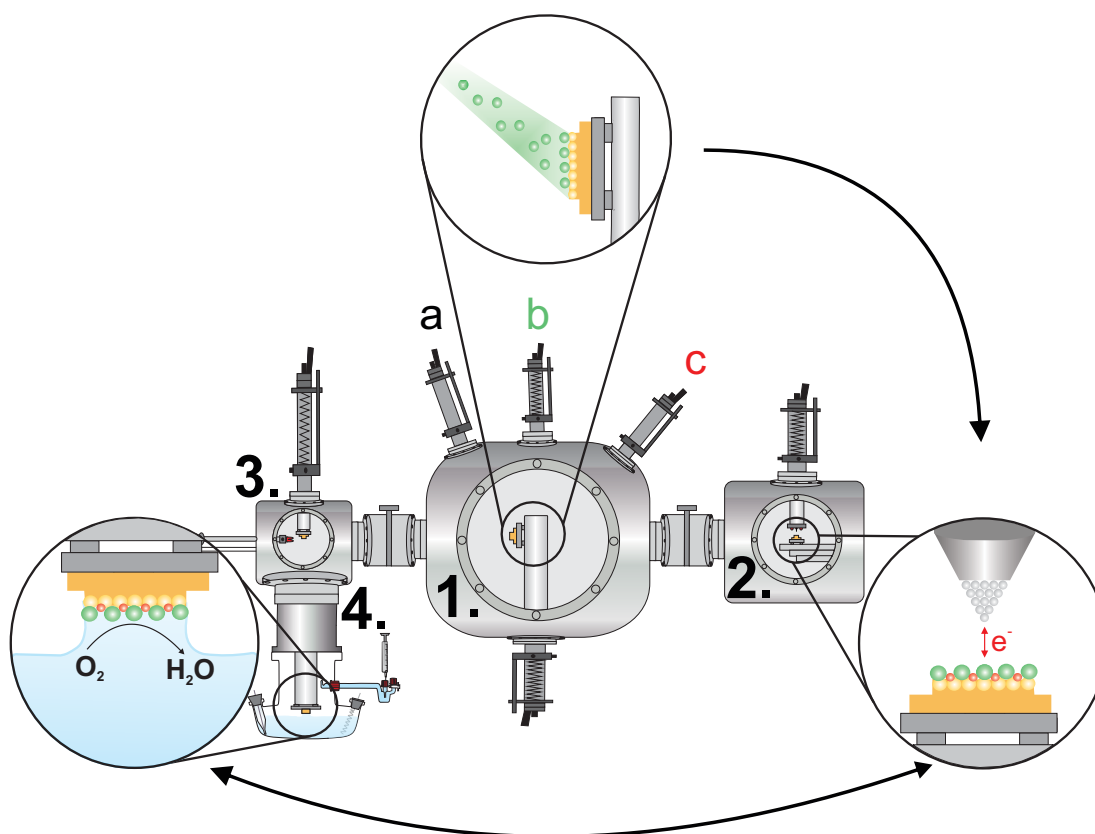
Incorporation of Fe centers into a PBP network leads to enhanced ORR activity.<sup>[77]</sup> The structure of the MOCN is preserved after electrocatalysis demonstrated by STM.<sup>[77]</sup> The interaction of the organic ligand, the metal center and the Au(111) substrate are further investigated with the support of theory in order to clarify the good structural stability.<sup>[100]</sup>

The ability of MOCNs for electrocatalysis are further enlarge by moving from a monometallic to a bimetallic approach. For this purpose a porphyrin molecule serves as organic ligand stabilizing Fe and Co centers.<sup>[103]</sup> The catalytic performance towards OER can be enhanced by moving from a monometallic to a bimetallic network.<sup>[103]</sup> The effect is discussed below.

Finally, thesis related experimental details of catalyst preparation and technical details of the utilized analytical tools are described.

## 2.1 Home-Built Ultra-High Vacuum-Electrochemistry Transfer System

The home-built transfer system<sup>[77]</sup> consists of three separated vacuum chambers (Fig. 2.1, No. 1-3). Optional an electrochemical cell can be connected (Fig. 2.1, No. 4).



**Figure 2.1:** Scheme of the home-built UHV-EC transfer system. The system consists of three different UHV chambers: (1) preparation chamber for sample preparation. The inset shows a schematic picture of molecule deposition onto the sample surface. For cleaning the substrate, a sputter gun (a) is mounted. The annealing filament is included in the main manipulator. For sample preparation a four-pocket molecular beam evaporator (b) and a metal evaporator (c) are available. (2) STM chamber for investigating the structure of the sample. The inset shows a zoom of the sample-tip position and a simplified picture of the tunneling current (red arrow) between both. (3) Transfer chamber to connect UHV sample preparation with the electrocatalytic experiment under ambient conditions. (4) The EC cell. The inset depicts the hanging meniscus configuration used for the electrocatalytic experiment to form a standard three electrode set-up.<sup>[77]</sup>

The first chamber is the preparation chamber used for sample preparation with a base pressure of  $5 \cdot 10^{-10}$  mbar. The cleaning procedure of the substrate is performed by multiple cycles of  $\text{Ar}^+$  ion sputtering and thermal annealing (Fig. 2.1 a). Organic molecules are sublimed from quartz crucibles (Knudsen cell) placed in a four pocket molecular beam evaporator (Dodecon) (Fig. 2.1 b). Metals are sublimed from either a pristine rod or as flakes from a molybdenum

## 2.1. Home-Built Ultra-High Vacuum-Electrochemistry Transfer System

---

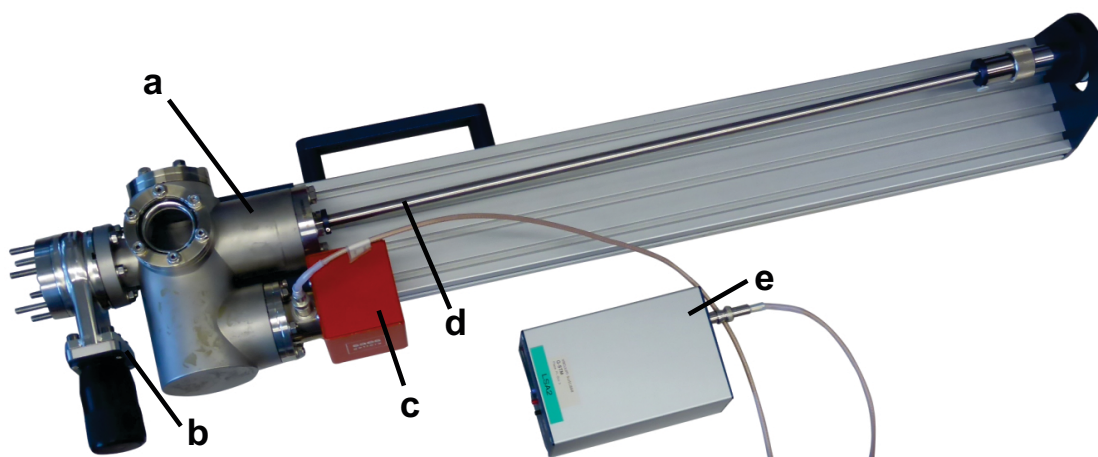
crucible by a single beam evaporator (Omicron) (Fig. 2.1 c). The detailed sample preparation procedures are described in section 2.5.1.

The topography of the sample is characterized by a room temperature (RT) UHV-STM (Fig. 2.1, No. 2). The STM chamber has a base pressure of  $1 \cdot 10^{-11}$  mbar. The third chamber (Fig. 2.1, No. 3) is a transfer chamber enabling the connection of UHV to the EC cell at ambient pressure. The transfer chamber has a base pressure of  $8 \cdot 10^{-8}$  mbar. Starting from the evacuated transfer chamber, the sample is moved from the preparation chamber to the manipulator of the transfer chamber. Subsequently, the transfer chamber is flooded with Ar gas (purity 5.0) until the pressure reaches 1 bar. The EC cell including the electrolyte is mounted at the bottom of the transfer chamber (Fig. 2.1, No. 4). Depending on the desired electrocatalytic experiment, the electrolyte is saturated with Ar (OER) or O<sub>2</sub> (ORR) gas (purity 5.0). As soon as ambient pressure is reached, the transfer chamber and EC cell will be connected by opening the gate valve in between. The sample is lowered close to the electrolyte surface by the manipulator. A drop of the electrolyte is placed on the crystal surface in order to facilitate the approach of the sample surface to the electrolyte. The drop approaches the electrolyte surface forming a meniscus. EC experiments are measured in the meniscus configuration shown in the inset in (Fig. 2.1). The transfer chamber can be used for both directions from UHV to the EC cell and vice versa. For this purpose the sample is rinsed with MilliQ water ( $R = 18.2 \text{ M}\Omega$ ) and dried with Ar after the EC experiment. Both cleaning and drying steps are carried out in the EC cell. By this way, it is possible to investigate the topography of the samples also postEC.

The analytical tools directly at the chamber are limited to STM and EC, but can be extended by characterization at different UHV set-ups enabled by a sample transfer via a vacuum suitcase.

### 2.1.1 Transfer by a Vacuum Suitcase

A vacuum suitcase (Ferrovac) prevents air contact of the sample during a transfer between two vacuum set-ups. This transfer method allows a comparability between STM, electrocatalysis and several other analytical tools such as XAS and XPS provided at different experimental set-ups. The suitcase consists of a small vacuum chamber (Fig. 2.2 a) with a base pressure of  $5 \cdot 10^{-9}$  mbar, decoupled from the environment by a gate valve (Fig. 2.2 b) and pumped by a small getter ion pump (Fig. 2.2 c). For sample transfer and storage a wobble stick is mounted (Fig. 2.2 d). The ion getter pump runs by a battery (Fig. 2.2 e) offering a transfer without continuous power supply.

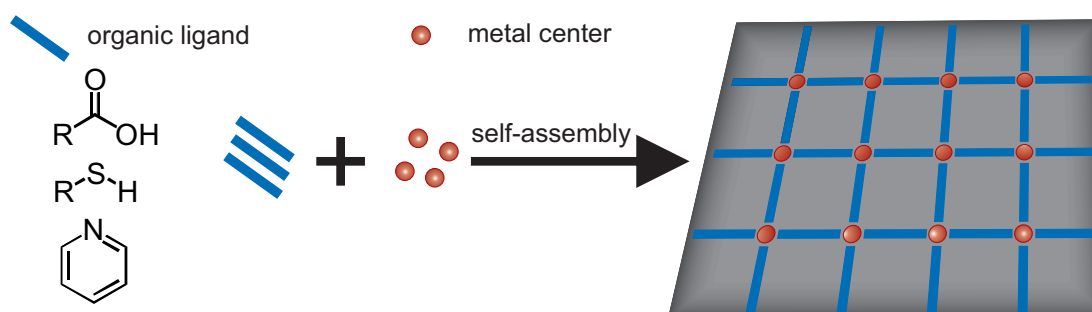


**Figure 2.2:** Set-up of the vacuum suitcase. The suitcase (Ferrovac) enables a sample transfer between different vacuum chambers without breaking the vacuum. It consists of the following parts: (a) small vacuum chamber; (b) gate valve; (c) ion getter pump; (d) wobble stick/sample storage; (e) controller for ion getter pump running on battery.

## 2.2 2D-Metal-Organic Coordination Networks

The modification of electrode surfaces by catalysts is a common route to enhance the redox reaction. Supramolecular architecture based on metal-organic coordination chemistry plays a leading role for the design of new catalytic materials.<sup>[52]</sup> Modifying surfaces by metal-organic nanostructuring offers a new class of molecular catalysts. Modular structures can be created by facile synthesis pathways based on self-assembling processes involving small organic molecules and metal centers as building blocks (Fig. 2.3).<sup>[53,54]</sup>

Preparing MOCNs in vacuum enables incorporation of undercoordinated metal centers which are particularly reactive. By tailoring the molecular network, precise positioning of the metal center is possible. The huge variety of available organic molecules, corresponding functional groups, and TM atoms allow chemical and electronical tailoring of the desired material.<sup>[44]</sup>



**Figure 2.3:** Self-assembly of metal-organic coordination networks (MOCNs) consisting of organic ligands (blue) as molecular building blocks e.g. carboxylic, thiol or pyridyl groups and metal centers (red) on conductive surfaces (grey).

## 2.3. Molecule-Metal-Substrate Interaction Explaining the Stability of the Catalyst

MOCNs are reminiscent of the active sites of enzymes, which drive a number of important reactions in nature e.g. water oxidation, oxygen reduction, and photosynthesis.<sup>[104,105]</sup> If the amino acid pocket of the enzyme is neglected, the corresponding active sites consists of mono or dinuclear metal centers stabilized by organic functional groups such as carboxyl, thiol, hydroxyl, amine and imine.<sup>[106–109]</sup> MOCN enables modeling of the enzymatic active sites. Therefore, these structures are expected to be highly redox active offering a promising electrocatalytic material with a huge variability.<sup>[110–112]</sup>

The self-assembled structure on the surface as well as the physico-chemical properties are determined by the organic ligand, the functional group, the nature and the facet of the substrate, the undercoordinated metal center, as well as, the metal's coordination number.<sup>[59]</sup> The formation of such self-assembled 2D-MOCNs are well understood today.<sup>[59]</sup> But the exploitation of these structures as electrocatalyst has just started. The opportunity of sublimation on conductive surfaces directly enables a facile modification of the WE.

The electronic structure of the redox active metal center is crucial for electrocatalytic properties. The strong influence of the elementary nature of the metal center was reported by Grumelli *et al.*<sup>[77]</sup>. A 2D-MOCN consisting of benzene-1,3,5-tricarboxylic acid (TMA) as organic ligand stabilizing either Mn or Fe centers self-assembled on Au(111) demonstrated enhanced ORR performance. The network was initially characterized by STM. Interestingly, the involved metal centers determined the mechanism of the ORR. Fe-TMA reduced oxygen through the two step (2+2)-electron mechanism including H<sub>2</sub>O<sub>2</sub> as side product, whereas Mn-TMA followed the preferred direct 4-electron mechanism.

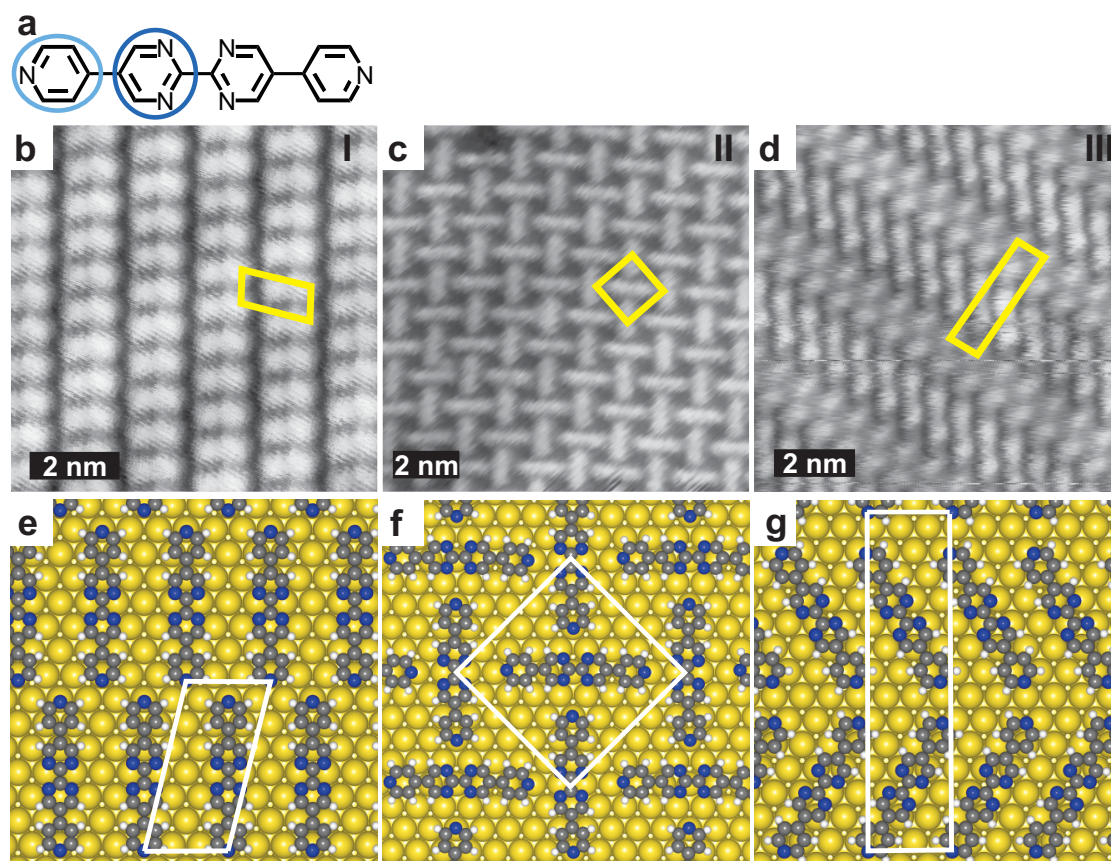
## 2.3 Molecule-Metal-Substrate Interaction Explaining the Stability of the Catalyst

In contrast to the nature of the coordinated TM, the organic ligand is not as influential on the reaction mechanism. Substituting the carboxylic coordination environment of TMA by N based ligands, for instance, pyridyl (light blue) and pyrimidyl (dark blue) groups of 5,5'-bis(4-pyridyl)(2,2'-bipirimidine) (PBP) (Fig. 2.4 a) leaves the mechanism unchanged at a (2+2)-electron mechanism.<sup>[77]</sup>

The electrocatalyst consists of a molecular network which self-assembles in three different morphologies on Au(111) (Fig. 2.4 b – d). The high resolution images demonstrate the molecule in a dumbbell shape. Each loop is attributed to half of the molecule consisting of one pyridyl and one pyrimidyl group. Phase I (Fig. 2.4 b) represents a linear array of molecules which has been reported earlier.<sup>[77,113]</sup> Phase II (Fig. 2.4 c) illustrates a grid structure based on pyridyl-pyrimidyl interaction. And phase III (Fig. 2.4 d) depicts a zig-zag pattern which has been

---

\* This section is based on publication<sup>[100]</sup>.



**Figure 2.4:** Polymorphism of PBP. (a) Chemical structure of 5,5'-bis(4-pyridyl)(2,2'-bipirimidine) (PBP), pyridyl group is indicated in light blue, pyrimidyl group labeled in dark blue; (b-d) STM images of the different phases, unit cells are indicated in yellow: (b) phase I, linear, unit cell:  $(17.3 \times 9.2) \text{ \AA}^2$ ,  $\alpha = 77^\circ$  ( $I_{\text{tunnel}} = 0.68 \text{ nA}$ ;  $U_{\text{bias}} = 0.919 \text{ V}$ ); (c) phase II, grid, unit cell:  $(16 \times 16) \text{ \AA}^2$ ,  $\alpha = 90^\circ$  ( $I_{\text{tunnel}} = 0.68 \text{ nA}$ ;  $U_{\text{bias}} = 0.919 \text{ V}$ ); (d) phase III, zig-zag, unit cell:  $(33.6 \times 8.1) \text{ \AA}^2$ ,  $\alpha = 92^\circ$  ( $I_{\text{tunnel}} = 0.17 \text{ nA}$ ;  $U_{\text{bias}} = 0.945 \text{ V}$ ). (e-g) optimized surface models: (e) linear phase; (f) grid phase; (g) zig-zag phase. Color code: H (white), N (blue), Fe (grey), Au (yellow).

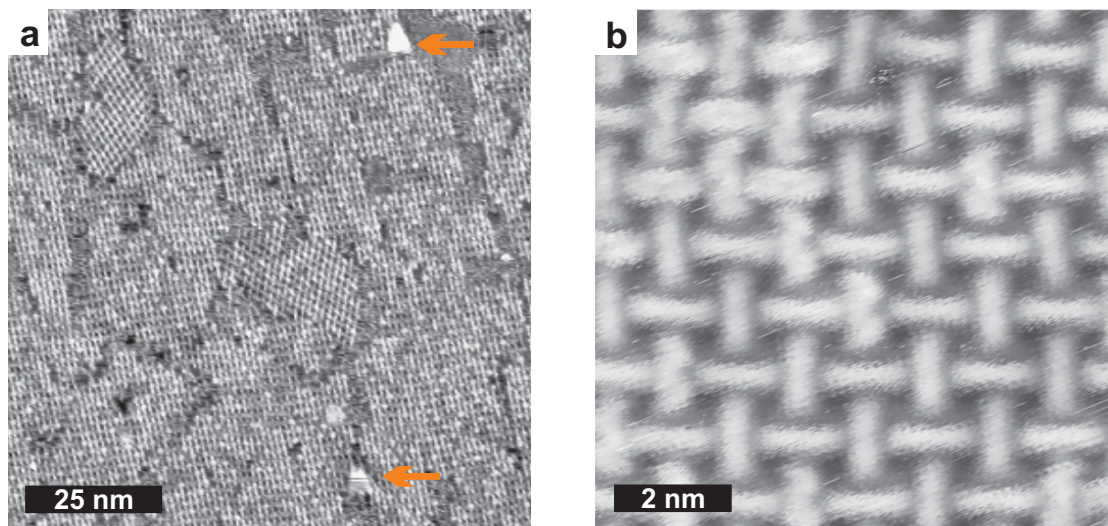
described earlier for Ag(111).<sup>[114]</sup> DFT\* shows physisorbed molecules on the surface mainly due to van-der-Waals interaction of the  $\pi$ -system of the molecule with the surface.

The molecular network turns electroactive when Fe is coordinated by the organic ligands on Au(111).<sup>[77]</sup> Fe deposition transforms the three diverse morphologies to exclusively one structure (Fig. 2.5 a, b). The selectivity of Fe could be explained by a change in coordination number. Phase I and III would coordinate Fe only by two nitrogens resulting in a Fe-N<sub>2</sub> bond (Fig. 2.4 e, g). In contrast, the grid structure coordinates Fe by 3 N atoms (Fig. 2.4 f). A higher coordination number results generally in higher binding energies and increased stability also

\* DFT calculations by Pilar Carro (Universidad de La Laguna, Tenerife, Spain): Calculations were performed with the VASP code<sup>[115,116]</sup> based on the slab-supercell approach and using the projector augmented-wave (PAW) method<sup>[117]</sup>. For estimating the van-der-Waals interaction the optB88-vdW method<sup>[118]</sup> was applied.

### 2.3. Molecule-Metal-Substrate Interaction Explaining the Stability of the Catalyst

reflected by the higher surface energy calculated by DFT. A similar increase of coordination number has been reported for Cu-N2/Cu-N3 networks.<sup>[119]</sup>

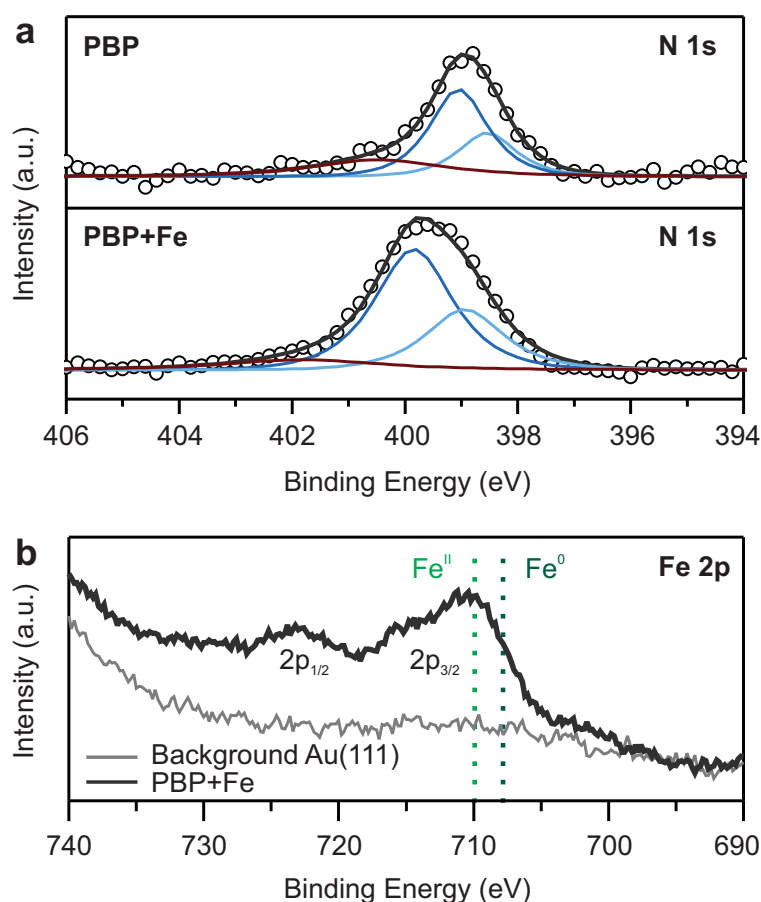


**Figure 2.5:** Fe centers coordinated in a self-assembled PBP network. (a) large area STM image, orange arrows indicate metallic Fe clusters ( $I_{\text{tunnel}} = 0.53 \text{ nA}$ ;  $U_{\text{bias}} = 1.6 \text{ V}$ ); (b) Zoom: demonstrating the grid morphology, unit cell:  $(16 \times 16) \text{ \AA}^2$ ,  $\alpha = 90^\circ$  ( $I_{\text{tunnel}} = 0.36 \text{ nA}$ ;  $U_{\text{bias}} = 1.5 \text{ V}$ ).

Fe atoms are not visible in STM images but clearly identified by XPS at N 1s and Fe 2p peak (Fig. 2.6 a, b). The N 1s peak can be subdivided into two contributions. One centered at 399.1 eV assigned to pyrimidine N (dark blue).<sup>[120]</sup> The second N peak is originating from pyridyl nitrogen and is located at 398.5 eV (light blue).<sup>[121]</sup> The ratio of pyrimidine and pyridyl nitrogen is 2:1 which is reflected by the peak area doubled for the pyrimidine contribution. The third peak (wine) at higher BEs can be removed when using asymmetric fit functions instead of Voigt functions and serves only as assisted fitting peak. The source of the asymmetric peak shape is unclear, but might be explained by for instance, a non-monochromatic x-ray source, shake-up satellites from intramolecular excitation, or from hydrogen bonded molecules resulting from possible multilayers which cannot be excluded.<sup>[122]</sup>

Fe deposition induces a shift in BE of both diverse N contributions. The ratio of the peak areas remains unchanged. The pyridyl nitrogen is shifted by about 0.4 eV to 398.9 eV, while the pyrimidyl N is shifted to 399.9 eV by 0.8 eV. The metal induced shift towards higher BEs is comparable with a peak shift of 0.5 eV reported for iminic N of free-base porphyrin metalated by Fe<sup>[123]</sup> and is support theoretically for N in a carbon matrix.<sup>[124]</sup>

The Fe 2p peak demonstrates a complicated background on Au(111), which hinders the required background subtraction for a valid peak fitting (Fig. 2.6 b). Nonetheless, the Fe 2p peak can be analyzed qualitatively. The main feature of Fe 2  $p_{3/2}$  at approximately 710 eV is attributed to oxidized Fe<sup>II</sup>. The small shoulder at around 707 eV corresponds presumably to metallic Fe<sup>0</sup> resulting from access Fe forming clusters on the surface (Fig. 2.5 a, orange arrows).



**Figure 2.6:** XPS analysis of PBP and PBP+Fe. (a) XPS of N 1s core level before and after Fe sublimation: asymmetric tail (wine), pyrimidine N (dark blue), pyridyl N (light blue); (b) Fe 2p core level of PBP+Fe (black) and Au(111) as background signal (grey). Binding energies of Fe<sup>2+</sup> (light green) and Fe<sup>0</sup> (green) are indicated.

The broad Fe signal might be explained by a multiplet structure originating from shake-up processes from electronic excitation in the organic ligand.

The origin of Fe<sup>II</sup> was investigated by Bader analysis looking at the interaction of the organic ligand, the metal center, and the substrate. The Fe center interacts by electron transfer to the N ligand but even stronger to the Au(111) surface resulting in a cationic Fe atom in the network. Moreover, the shift of N to higher BEs demonstrates the anionic character of N ligands which can be explained by the electron transfer of Fe to the coordinating N. The induced charge distribution results in higher binding energies due to reduced electron density at the core electron of anionic N. The strong interaction of the metal center explains the structural integrity of the network postORR observed by STM.<sup>[77]</sup>

The previous short discussion exemplary highlights some key concepts of self-assembled MOCNs regarding geometric and electronic structure. In the following, this approach will be

put together with electrocatalysis to carve out the complete methodology of the approach pursued in this thesis.

## 2.4 Bimetallic Coordination Network for Oxygen Evolution Reaction

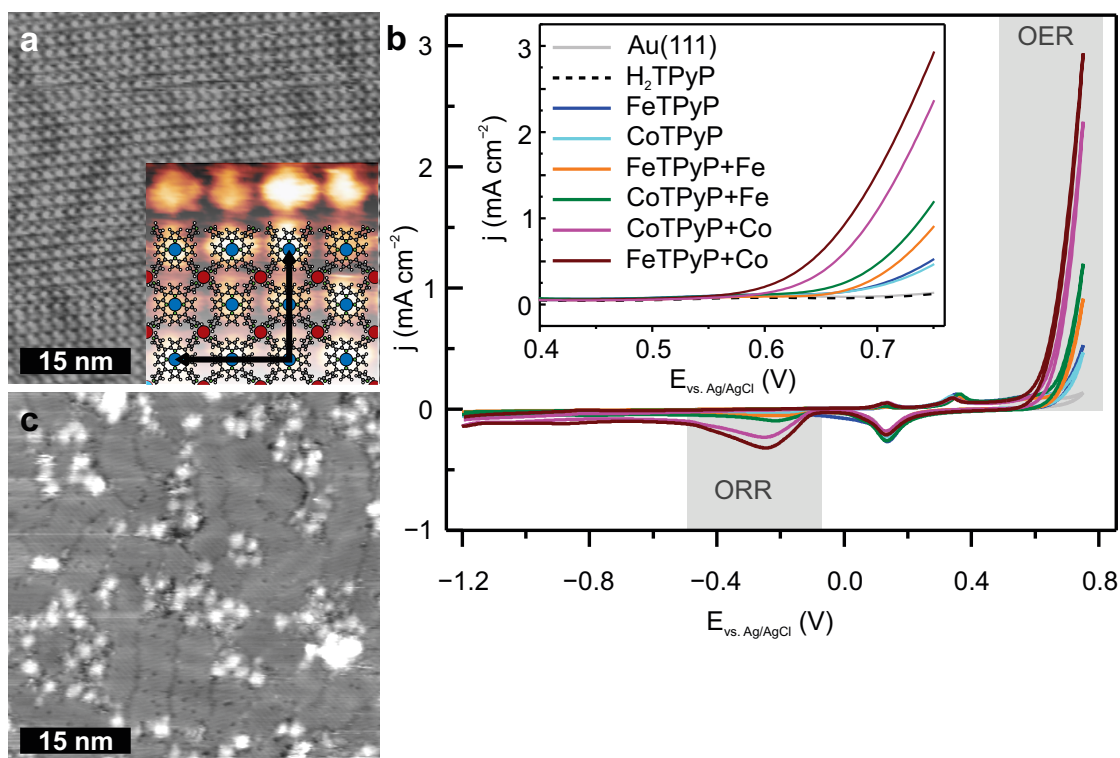
The electronic structure of the active metal species is not only influenced by the organic ligand and nature of the metal center but also by including a second metal into the MOCN. Bimetallic materials can outperform their monometallic counter parts due to synergetic effects between the two metal centers.<sup>[106,125,126]</sup> However, the effect of the second metal center on the catalytic properties is not well understood and predicting new catalytic behavior is rather impossible. Therefore, understanding bimetallic active sites and predicting properties of bimetallic systems is still on-going research. The effect of a second metal center is especially large when only a mono- or submonolayer forms the electrocatalyst.<sup>[125]</sup> For enlightenment of the influence of the second metal, MOCNs with an additional metal center might help to understand underlying processes.

A bimetallic porphyrin network was synthesized by sublimation of MPs chelating either a Fe or Co center. Additionally, either Fe or Co were co-deposited to the molecular network as second metal center forming a homo- or heterobimetallic monolayer. The intact molecular network of CoTPyP with additionally sublimed Co (CoTPyP+Co) is depicted in Fig. 2.7 a. The inset demonstrates the regular square arrangement of the molecules exemplified by the superimposed chemical structure. In the model the second metal centers are stabilized at the peripheric pyridyl groups as has been demonstrated earlier.<sup>[127,128]</sup> The unit cell is determined as  $(3.0 \times 2.9) \text{ nm}^2$ ,  $\alpha = 90^\circ$  indicated by vectors in the image. Neighboring molecules are rotated by  $90^\circ$  against each other explaining the extended unit cell of four molecules.

The bimetallic systems were utilized successfully as bifunctional electrocatalyst for the oxygen half-cell reaction in alkaline electrolyte (Fig. 2.7 b). While metal-free  $\text{H}_2\text{TPyP}$  (black dashed) lacks of  $\text{O}_2$  evolution activity, the monometallic networks of FeTPyP (blue) and CoTPyP (light blue) showed a clear enhancement. Both FeTPyP and CoTPyP exhibit an activation on-set potential of 0.65 V which is a reduction of about 0.1 V compared to the Au(111) substrate (grey) and the metal-free  $\text{H}_2\text{TPyP}$  network. Another proof of the  $\text{O}_2$  evolution is the appearance of the back reaction (ORR) which occurs at about  $-0.22 \text{ V}$ . As  $\text{O}_2$  has been expelled by Ar prior the EC experiment, the detected  $\text{O}_2$  stems from driving the OER producing  $\text{O}_2$  electrochemically. Thus, the presence of the metals is crucial for the electrocatalytic performance.

The bimetallic systems formed by Co deposition to the corresponding molecular network eventually increased the  $\text{O}_2$  production of CoTPyP and FeTPyP, respectively, demonstrated by an increased current density of more than  $1 \text{ mA cm}^{-2}$  at 0.75 V. Moreover, the activation overpotential is reduced which is expressed by the negatively shifted on-set potential in the CV by approximately 0.1 V in total going from monometallic to Fe and Co co-deposited samples

\* This section is based on publication<sup>[103]</sup>

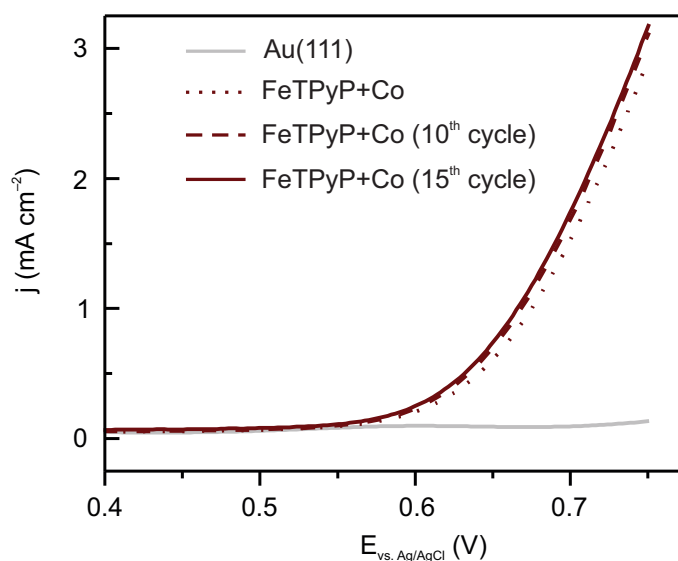


**Figure 2.7:** Bifunctional and bimetallic electrocatalyst based on FeTPyP, CoTPyP, Fe and Co. (a) STM image of the freshly prepared CoTPyP+Co monolayer on Au(111) ( $I_{\text{tunnel}} = 0.2 \text{ nA}$ ;  $U_{\text{bias}} = -1.1 \text{ V}$ ). Inset: molecular resolution image with model and lattice vectors (black) superimposed (CoTPyP+Fe). Color code: Fe (red), Co (dark blue), C (grey), N (blue), H (white). Unit cell:  $(3.0 \times 2.9) \text{ nm}^2$ ,  $\alpha = 90^\circ$ ; (b) CV ( $-1.2 \text{ V}$  to  $0.75 \text{ V}$ ,  $50 \text{ mV s}^{-1}$ , NaOH  $0.1 \text{ M}$ , Ar sat.) for all molecular catalysts. Inset: anodic branch of CV. Color code:  $\text{H}_2\text{TPyP}$  (black dotted line), bare Au(111) electrode (grey), FeTPyP (blue), CoTPyP (light blue), FeTPyP+Fe (orange), CoTPyP+Fe (green), CoTPyP+Co (pink), and FeTPyP+Co (wine); (c) CoTPyP+Co based active catalyst after OER (only one LSV,  $0 \text{ V}$  to  $0.60 \text{ V}$ ,  $50 \text{ mV s}^{-1}$ ,  $0.1 \text{ M NaOH}$ , Ar sat.) ( $I_{\text{tunnel}} = 0.2 \text{ nA}$ ;  $U_{\text{bias}} = 0.8 \text{ V}$ ).

(Fig. 2.7 b). The effect becomes clearly visible in the inset demonstrating the best catalytic activity for Co co-deposition to the molecular network. The enhanced  $\text{O}_2$  production is reflected in the increased current density of the ORR at about  $-0.24 \text{ V}$ .

Besides the electrochemical performance, the electrocatalyst's stability is also an important parameter for describing an electrocatalytic system. The stability of the electrocatalyst is investigated from two different perspectives: 1) the structural stability and 2) electrochemical stability.

The well-known surface sensitivity of electrocatalytic reactions on the atomic level desires a detailed structural analysis of the catalyst on the molecular scale by STM both before and after driving OER and ORR. The STM topography changed dramatically already after the very first cycle (Fig. 2.7 c) demonstrating a poor structural stability of the MOCN.



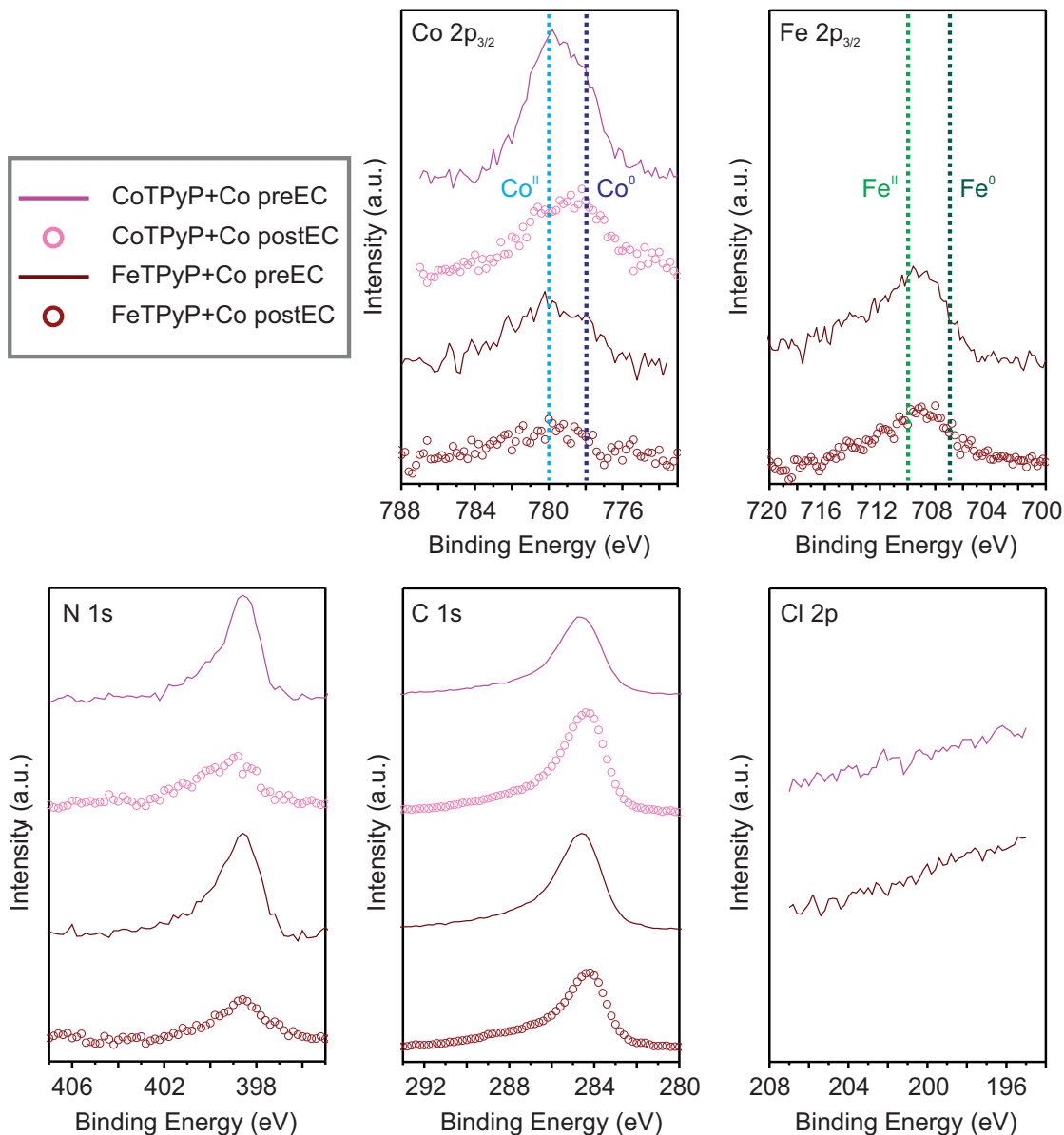
**Figure 2.8:** Electrochemical stability for OER of the bimetallic electrocatalyst exemplified at the FeTPyP+Co system. Anodic branch of CV ( $50 \text{ mV s}^{-1}$ , NaOH 0.1 M, Ar sat.) for Au(111) (grey) and FeTPyP+Co: 1<sup>st</sup> cycle (wine), 10<sup>th</sup> (wine dotted) and 15<sup>th</sup> (wine dashed).

In contrast the electrocatalytic stability was determined for at least 15 cycles exemplified for the most active heterobimetallic FeTPyP+Co system catalyzing the OER (Fig. 2.8). Neither the on-set potential nor the current density changes strongly going from the first to the 15<sup>th</sup> cycle of OER demonstrating a reasonable electrochemical stability.

The highly stable electrochemical response is contradictory to the morphological transformation because such a strong surface change is expected to be visible in the EC signal due to the surface dependence. Hence, the squared network is not believed to be the real catalyst but the postEC structure depicted in Fig. 2.7 c. Considering the high EC stability, it suggests the formation of the real catalyst before or meanwhile driving the OER for the first time. The current density increases quiet steep and might hide additional current signal which could be traced back to the rearrangement of the active surface. Supposedly, once the structure is formed it leaves the EC performance unaffected.

As STM lacks of element specificity, the results of the structural analysis postEC is combined with XPS. The two most active catalysts prepared by Co co-deposition as representatives of the various systems are discussed (Fig. 2.9). The Co  $2p_{3/2}$  core level of CoTPyP+Co represents a mostly oxidized signal located at about 780 eV and is equivalent to a formal +2 oxidation state which is expected for Co stabilized within a porphyrin macrocycle.<sup>[129–131]</sup> Additionally, metallic Co is detected which is explained by excess Co provided during the sublimation process. An excessive supply of Co cannot be implemented within the network and remains in the metallic state. Driving the OER leaves the general response at the Co  $2p_{3/2}$  signal unchanged. However, the intensity is decreased pointing to a loss of material during the EC experiment. The heterobimetallic catalyst FeTPyP+Co demonstrates a similar Co  $2p_{3/2}$  peak.

The oxidized Co signal is again traced back to chelated Co within the MOCN, while the metallic state can be explained by excess Co supply. The FeTPyP+Co postEC shows similar results as the CoTPyP+Co demonstrating a chemical stability also for the heterobimetallic network.



**Figure 2.9:** XPS analysis of the most active bifunctional electrocatalysts: FeTPyP+Co and CoTPyP+Co at following core levels: Co 2p<sub>3/2</sub>, Fe 2p<sub>3/2</sub>, N 1s, C 1s, Cl 2p. PostEC samples: one LSV (0.0 V to 0.60 V, 50 mV s<sup>-1</sup>, 0.1 M NaOH, Ar sat.) Color code: CoTPyP+Co preEC (pink) and postEC (pink dotted), FeTPyP+Co (wine) and postEC (wine dotted). Additionally oxidized and metallic Co and Fe are indicated: Co<sup>II</sup> (light blue), Co<sup>0</sup> (dark blue), Fe<sup>II</sup> (light green), Fe<sup>0</sup> (dark green).

Similar to the constant chemical environment of the Co metal before and after OER, the Fe 2p<sub>3/2</sub> core level illustrates also a consistency for both samples. The maximum intensity

## 2.4. Bimetallic Coordination Network for Oxygen Evolution Reaction

of the Fe 2p<sub>3/2</sub> core level at about 709 eV has a clear oxidized character which might stem from the organic coordination environment provided by the porphyrins.<sup>[123,132]</sup> However, for monolayers of porphyrins on Ag(111) the Fe 2p<sub>3/2</sub> peak overlaps with the metallic position at approximately 707 eV.<sup>[123,132]</sup> This effect is explained by a strong interaction of the Fe center with the surface resulting in a core level shift towards lower BE. The interaction with Au(111) might be weaker and it could therefore explain the intermediate position between the BE at 710 eV of a +2 oxidation state of Fe which is formally expected for FeTPyP and the BE of Fe<sup>0</sup> at 707 eV.

The stability of the organic backbone is probed at C 1s and N 1s core levels. Neither the BE nor the shape undergo a major change due to the exposure to the EC experiment. The intensity reduction emphasizes the proposed material loss due to the EC experiment already reported for the two metal centers. The peak maximum of N 1s lies at a BE of approximately 398.6 eV which is repeated for all four systems. The BE is reminiscent of N coordinating a metal center in the porphyrin core.<sup>[123]</sup> In line with the N 1s peak, the C 1s peak is unaltered. The consistency of the N 1s and the C 1s core levels for all four samples leads to the conclusion of a preserved organic backbone after OER.

The molecules are provided with an additional axial chloride ligand. Residual chloride on the surface can interfere in the presented potential window for the OER and ORR. Indeed, a chloride signal is present at 0.35 V (Fig. 2.7 b). However, XPS shows the absence of chloride on the surface. Hence, the ligand supposedly detaches during sublimation process and arrives already without the chloride ligand on the surface forming the MOCN. Thus, the chloride visible in the CV can only stem from the Ag/AgCl reference electrode (RE).

The unaltered core levels for both metal centers as well as the organic backbone represented by C 1s and N 1s suggests a constant chemical environment for all components of the MOCN postOER. Nevertheless, the network could not be resolved by STM demonstrating a structural change. The three-dimensional orientation visible in the STM image could be explained by a sintering process of the molecules. On the other hand, cluster formation of the molecules excludes a stabilization of the second metal center at the periphery as assumed for freshly prepared networks. Nonetheless, the Co 2p<sub>3/2</sub> peak in FeTPyP+Co resembles CoTPyP+Co which is attributed to chelated Co. Therefore, the appearance of the STM image cannot be fully understood by XPS results. Additionally, the chemical stability demonstrated by XPS is contradictory to the large changes visible by STM.

This short overview represents the starting point of the experimental results which will be discussed in the following chapters. Resolving the fate of the MOCN and characterizing the actual catalytic material was achieved by XAS as described in Chap. 4.

## 2.5 Experimental

The experimental procedures for the various sample preparations are reported in the following. Furthermore, technical details and utilized electrolytes involved in the EC experiments are described. Throughout this thesis multiple characterization tools are used. Technical details and experimental conditions will be reviewed.

### 2.5.1 Sample Preparation

#### Cleaning the Substrate

Au(111) is cleaned by  $\text{Ar}^+$  ion sputtering (1.0 kV) for 10-15 min followed by an annealing step at 823 K for 10-15 min. After EC experiment at least 2 sputtering/annealing cycles were necessary to obtain a clean surface. Au(111) serves as substrate in all experiments with the exception of Chap. 6 which uses  $\text{Fe}_3\text{O}_4(001)$ .

$\text{Fe}_3\text{O}_4(001)$  is cleaned by multiple sputtering/annealing cycles similar to Au(111) but applying an annealing temperature of 923 K. Every third cleaning cycle, the annealing step was performed in an oxygen environment ( $6 \cdot 10^{-7}$  mbar) for 15 min followed by an annealing step in UHV at 923 K for 5-10 min. After EC experiment or metal deposition at least 10 cleaning cycles are performed to ensure a clean surface.

#### Preparation of Self-Assembled Organic Network

Self-assembled monolayers were created using different organic molecules: 5,10,15,20-tetra(4-pyridyl)21H,23H-porphyrin cobalt(III) chloride (CoTPyP); 5,10,15,20-tetra(4-pyridyl)21H,23H-porphyrin copper(III) chloride (CuTPyP); 5,10,15,20-tetra(4-phenyl)21H,23H-porphyrin iron(III) chloride (FeTPP), 5,10,15,20-tetra(4-pyridyl)21H,23H-porphyrin iron(III) chloride (FeTPyP); and 5,5'-bis(4-pyridyl)(2,2'-bipiridine) (PBP). Preparation details such as sublimation temperature  $T_s$  and time  $t_s$ , temperature of the substrate  $T_{\text{Au}(111)}$  during sublimation, annealing temperature  $T_{\text{ann}}$ , and time  $t_{\text{ann}}$  applied after sublimation are shown in Tab. 2.1.

**Table 2.1:** Experimental details for preparing of self-assembled organic networks. Sublimation parameters: sublimation temperature  $T_s$ ; sublimation time  $t_s$ ; temperature of the substrate  $T_{\text{Au}(111)}$  during sublimation; annealing temperature  $T_{\text{ann}}$  and time  $t_{\text{ann}}$  which was applied after the sublimation step.

Chapter	Molecule	$T_s$ ; $t_s$	$T_{\text{Au}(111)}$	$T_{\text{ann}}$ ; $t_{\text{ann}}$	Supplier
2	PBP	470 K; 20-35 min	RT	413 K; 10 min	synthesized <sup>[114]</sup>
3	CoTPyP	683 K; 30 min	RT		Frontier Scientific, 99 %
	CuTPyP	683 K; 15-30 min	RT		Frontier Scientific, 99 %
	FeTPP	618 K; 20 min	RT	373 K; 10 min	Frontier Scientific, 99 %
	FeTPyP	744 K; 20-35 min	RT		Frontier Scientific, 99 %
4	CoTPyP	683 K; 30 min	523 K	523 K; 5 min	Frontier Scientific, 99 %
	FeTPyP	744 K; 20-35 min	523 K	523 K; 5 min	Frontier Scientific, 99 %

### Metal Deposition

For MOCNs Co (Goodfellows, 99.99 %) and Fe (Goodfellows, 99.99 %) are co-deposited to the self-assembled organic networks by an e-beam metal evaporator (Omicron). Preparation parameters such as temperature of the substrate  $T_{Au(111)}$  during deposition, annealing temperature  $T_{ann}$ , and time  $t_{ann}$  applied after deposition are illustrated in Tab. 2.2.

**Table 2.2:** Parameters of metal co-deposition: temperature of the substrate  $T_{Au(111)}$ ; post annealing temperature  $T_{ann}$  and time  $t_{ann}$ .

Chapter	Network	$T_{sub}$	$T_{ann}; t_{ann}$
2	PBP+Fe	413 K	413 K; 5 min
3	CoTPyP+Fe	RT	
	CuTPyP+Co	RT	
	FeTPP+Co	RT	
	FeTPyP+Co	373 K	373 K; 5 min
4	FeTPyP+Co	523 K	523 K; 5 min

### Preparation of Cobalt Cluster

Co was sublimed by an e-beam metal evaporator (Omicron) using a Co rod (Goodfellows, 99.99 %). For reproducibility the amount of evaporated Co was controlled by a quartz crystal microbalance (QCM). First the QCM was calibrated by exploring the coverage of Co on Au(111) by STM. The parameters for the desired amount of Co were calculated accordingly and the deposition time was adjusted. For each preparation the metal evaporator deposition rate was stabilized onto the QCM and the momentary deposition time was calculated. A deposition rate of approx. 0.02 monolayer per minute was achieved. For preparation of the metallic nanoclusters the Au(111) substrate was held at RT.

### Ag Adatoms on Magnetite

Silver deposition was performed by an e-beam metal evaporator (Omicron) filled with an Ag rod (Goodfellows, 99.99 %). The amount of Ag was controlled by a QCM, procedure is described above.

### 2.5.2 Electrochemical Experiment

All EC experiments were conducted with an Autolab PGSTAT302N potentiostat (Metrohm) operated with Nova 1.9 software. The standard three electrode set-up was provided by a Ag/AgCl/(3 M KCl) reference electrode (RE) and a Pt wire as counter electrode (CE). In this thesis, all EC experiments are presented with respect to the Ag/AgCl/(3 M KCl) reference electrode.

### Electrocatalysis

The 0.1 M NaOH electrolyte was freshly prepared from NaOH pellets (Sigma-Aldrich, 99.99 %) dissolved in MilliQ water ( $R = 18.2 \text{ M}\Omega$ ). For ORR the electrolyte was enriched with  $\text{O}_2$  gas (purity 5.0). In order to run the OER experiment air  $\text{O}_2$  was expelled from the electrolyte by Ar (purity 5.0). Details of scan speed, potential window and EC technique are indicated in corresponding chapters.

### 2.5.3 Structure Analysis: Sample Preparation and Instrumental Details

#### Scanning Tunneling Microscopy

All STM images were recorded at RT mainly in the home-built set up described in section 2.1. Nanonis (SPECS) was used to control the STM electronics. Metallic STM tips were prepared by electrochemical etching of a tungsten wire (MaTeck, 99.5 %) in a 2 M NaOH (Merck, 99 %) solution, freshly prepared. Subsequently, the tip was introduced into the UHV to prevent oxidation. Bias is applied at the tip.

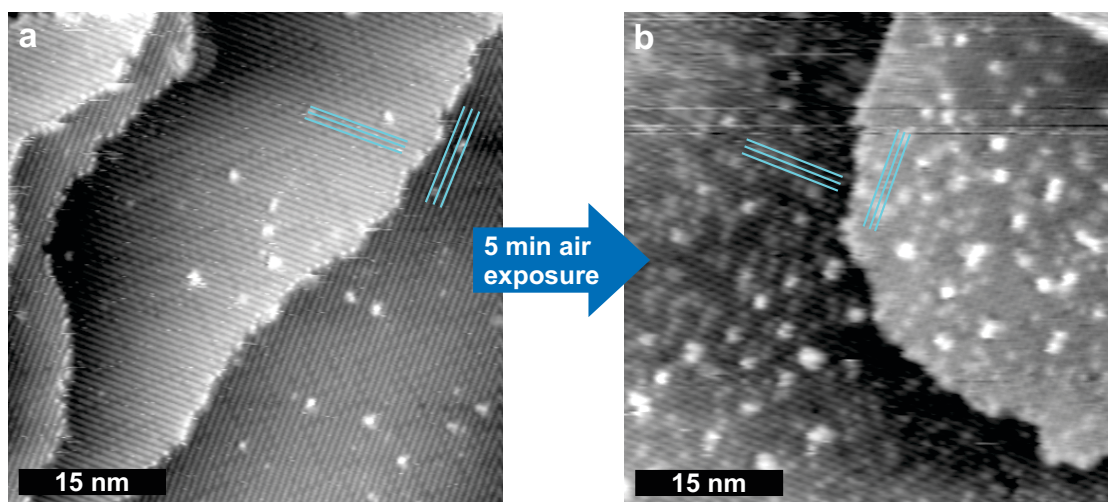
The STM images in Chap. 3 were recorded during a beamtime time at the X-Treme beamline of the Swiss Light Source, Paul Scherrer Institute, Switzerland<sup>[133]</sup> with a commercial Omicron STM using also electrochemically etched W tips.

STM images were analyzed by WsXM software.<sup>[134]</sup>

#### Low-Energy Electron Diffraction

LEED characterization was performed in a ErLEED 1000-A (SPECS) operated by the interface analysis service department, Max Planck Institute for Solid State Research, Stuttgart.

Sample preparation was performed in the experimental set-up provided by the interface analysis group. For the electrolyte exposure, samples were transferred out of the vacuum through a standard load lock vented with  $\text{N}_2$ . Subsequently, the sample was taken out of the chamber and covered with a drop of 0.1 M NaOH, freshly prepared. It was rinsed by MilliQ water ( $R = 18.2 \text{ M}\Omega$ ) before transferring back to UHV. This procedure is still comparable to the experiments performed in the transfer system as a short exposure of the clean  $\text{Fe}_3\text{O}_4(001)$  crystal (Fig. 2.10 a) to air was not affecting the reconstruction lines (Fig. 2.10 b).



**Figure 2.10:**  $\text{Fe}_3\text{O}_4(001)$  exposed to 5 min air. (a) UHV-clean  $\text{Fe}_3\text{O}_4(001)$ , reconstruction lines are indicated in cyan ( $I_{\text{tunnel}} = 0.5 \text{ nA}$ ;  $U_{\text{bias}} = 2.1 \text{ V}$ ); (b)  $\text{Fe}_3\text{O}_4(001)$  exposed to 5 min air, reconstruction lines (cyan) remain clearly visible ( $I_{\text{tunnel}} = 0.3 \text{ nA}$ ;  $U_{\text{bias}} = 1.5 \text{ V}$ ).

## 2.5.4 X-Ray Spectroscopy: Instrumental Details and Data Processing

### X-Ray Photoelectron Spectroscopy

Two different XPS instruments were used. One is a commercial set-up (SPECS) offering a non-monochromatic Mg or Al  $K\alpha$  photon source ( $h\nu = 1253.6 \text{ eV}$  and  $h\nu = 1486.6 \text{ eV}$ , respectively). A Phoibos 150 (SPECS) analyzer was implemented in the system. Spectra were recorded with a pass Energy of  $E_{\text{pass}} = 20 \text{ eV}$ . The SPECS set-up using the Mg  $K\alpha$  photon source was mainly utilized for data presented in Chap. 5. XPS data is normalized on the maximum intensity of the Au  $4f_{7/2}$  core level.

Additionally, in Chap. 6 another experimental set-up was utilized which was operated by the interface analysis service department, Max Planck Institute for Solid State Research, Stuttgart. The x-ray source is a monochromatic Al  $K\alpha$  line (Kratos Ultra, Axis). Survey scans and detailed spectra were recorded using  $E_{\text{pass}} = 80 \text{ eV}$  and  $E_{\text{pass}} = 20 \text{ eV}$ , respectively. Note: the same sample preparation was followed as described for LEED measurements (section 2.5.3). The utilized XPS source and set-up is identified at the spectra in Chap. 6.

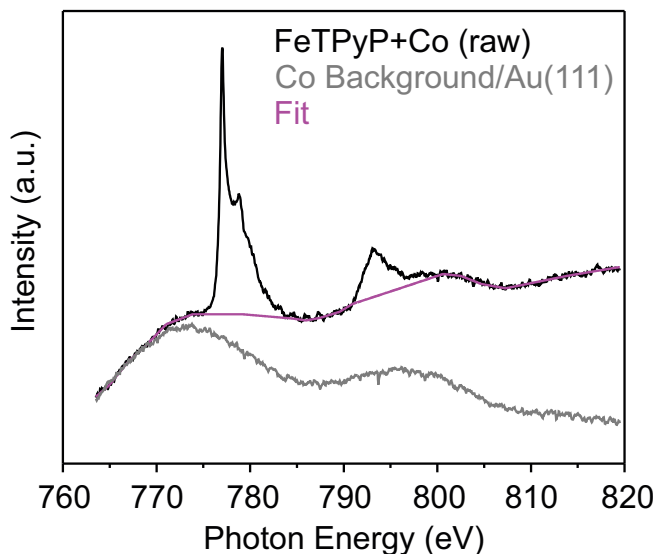
XPS data was analyzed using XPSpeak4.1 software.

### X-Ray Absorption Spectroscopy

All XAS experiments were performed at the X-Treme beamline of the Swiss Light Source, Paul Scherrer Institute, Switzerland<sup>[133]</sup>. Linear horizontal ( $\sigma^h$ ) or linear vertical ( $\sigma^v$ ) polarized x-rays were generated by a synchrotron source. Spectra were recorded at 300 K in grazing incidence ( $\theta = 60^\circ$ ) using TEY mode. A negligible magnetic field of 50 mT was applied helping

the electrons to leave the surface resulting in a reduced noise on the measured drain current. Contrary to the notation explained in section 1.3.2,  $\sigma^h$  refers to out-of-plane, while  $\sigma^v$  represents in-plane excitation due to a different definition at this specific beamline.

Post EC samples investigated by XAS were prepared in Stuttgart and transferred using a vacuum suitcase to the Swiss Light Source. The transfer is described in section 2.1.1.



**Figure 2.11:** Exemplary background subtraction of XAS raw data. Color code: raw data of FeTPyP+Co at Co  $L_{2,3}$ -absorption edge for  $\sigma^h$  (black); manual fit (purple); measured background of Co  $L_{2,3}$ -edge on Au(111) for  $\sigma^h$  (grey).

The data was analyzed with Igor and OriginPro. The background differed for each sample, thus subtracting a baseline was rather complicated. The baseline was fitted manually in OriginPro for each polarization individually. A representative example is shown in Fig. 2.11. Subsequently, the background corrected  $\sigma^h$  and  $\sigma^v$  were summed (in the following referred as XAS). The XLD is calculated by subtracting  $\sigma^h$  from  $\sigma^v$ . Data is normalized to the integral of the corresponding XAS. However, the N K-edge was normalized to the integral of XAS of the corresponding Fe  $L_{2,3}$ -edge. Furthermore, the Cu  $L_{2,3}$ -edge is normalized on the integral of the CuTPyP for a better comparison of the changed intensities due to a change in occupation from  $d^9$  to  $d^{10}$ .

### 3 Metal Exchange in Porphyrins at the Vacuum/Solid Interface

Controlled synthesis and modification of organic nanostructures is key for designing new materials for, e.g., sensors<sup>[135]</sup>, (electro-)catalysts<sup>[39,42]</sup> or optoelectronics<sup>[136]</sup>. Inspired by nature, porphyrins are promising molecules to generate highly reactive, stable and flexible technical devices. A prominent example of naturally occurring porphyrins is the iron porphyrin incorporated in the heme-group serving as co-factor for enzymes involved in transport and storage of respirator gases, as well as constituting the active site of cytochrome P450.<sup>[137,138]</sup> Another example is the Mg porphyrin active site of chlorophyll, which is involved in the photosynthesis process.<sup>[139]</sup>

Porphyrins are large organic molecules consisting of a rigid tetrapyrrole macrocycle with a large conjugated  $\pi$ -system leading to high chemical and mechanical stability as well as a planar geometry. The macrocycle acts as a tetradentate ligand explaining the strong metal-organic coordination bond which is responsible for the extraordinary stability of the complex. Moreover, the tetrapyrrole ring provides a coordination cage for many metal center of the periodic table enabling a great variety of complexes. The planar geometry provides an easy access of reactants to the active metal cation supporting the reactivity of the MP. Furthermore, the planarity makes it attractive to the field of surface science due to the utilization as organic structural element for a bottom-up approach of novel nanostructured materials and its investigation on the molecular scale by scanning probe techniques. In addition to the large number of metal centers applicable to the macrocycle, the organic backbone can be modified by suitable functional groups connected in *meso*-position at the methine bridges or at the pyrrolic  $\beta$  site. Thus, the variations of this molecular class are seemingly unlimited offering a large toolbox for tailoring the molecular building block towards the needs of the specific applications and promoting research on porphyrins and related molecules in thin films, as monolayers, and at the single-molecule level.<sup>[45,46,140–142]</sup>

In order to exploit the full capacity of the MP's variety, suitable synthetic pathways to incorporate the active metal center are of great importance. Typical techniques utilized are

---

\* This chapter is based on publication [2] of my publication list (see CV).

metalation, demetalation, and transmetalation, which have been studied extensively in liquid environment.<sup>[143–148]</sup> Metal incorporation (metalation) in a free-base porphyrin proceeds by substitution of the two pyrrolic hydrogens by the metal cation, generally present as metal salt in the reaction flask.<sup>[143,144]</sup> Demetalation is performed by adding diluted acetic acid or water following a hydrolysis reaction pathway. An alternative synthetic route is the so-called transmetalation process describing the exchange of two different metal cations.

In some cases transmetalation offers a more efficient synthesis pathway for a specific MP. For instance the formation of Zn-tetraphenylporphyrin (TPP) demonstrated a faster reaction rate starting from HgTPP than from the free-base porphyrin.<sup>[147]</sup> This observation also excludes the free-base porphyrin as intermediate for the transmetalation reaction mechanism in this context.<sup>[144]</sup> The possibility of a transmetalation reaction strongly depends on the properties of the metal cation such as electronegativity, charge, bond strength, solvation energy and size of the cation. Alongside qualitative studies, reaction rates and mechanisms of metalation and transmetalation have been investigated for a better understanding of the process.<sup>[145–150]</sup> However, the concepts in liquid environment are not easy transferable to surface science in UHV but serves as inspiration.

The flat geometry making the active center accessible for a variety of reactants also results in a strong influence of the surface on the central metal atom changing the catalytic properties of the MP, additionally.<sup>[151]</sup> Hence, the interest in finding *in situ* synthesis and modification of MPs on surfaces is rising. There are two experimental pathways to generate self-assembled MP networks in UHV: 1) sublimation of the desired MP directly onto the substrate, 2) on-surface metalation of free-base porphyrin by up-taking metal atoms at the vacuum/solid interface. In the latter case, the metalation can occur through the incorporation of readily available metal atoms from the metallic support,<sup>[152]</sup> or alternatively through the allocation of a different metal by thermal evaporation.<sup>[123,153,154]</sup> The metalation can therefore be achieved with various metal species and is routinely used to synthesize MPs on surfaces on demand.<sup>[45,140]</sup>

While metalation of free-base porphyrin became a standard procedure in vacuum, an on-surface transmetalation process is rarely reported. Conflicting publications demonstrate the complexity of on-surface transmetalation by showing both the formation of a bimetallic MOCN<sup>[127,128]</sup> and a cationic exchange on the surface<sup>[155,156]</sup>. Two studies describe the replacement of Ni or Co by Cu, which is supplied through the adatom gas on the Cu(111) surface in ultra-high vacuum.<sup>[155,156]</sup> A third study describes the exchange at the solid/liquid interface, in which Zn is replaced by Cu.<sup>[157]</sup> The process underlying the metal exchange is far from being understood which is exemplified by two publications: on the one hand Franke *et al.*<sup>[157]</sup> report that Zn is substituted by Cu in a TPP network at the solid-liquid interface. On the other hand, Shi *et al.*<sup>[128]</sup> report the formation of a bimetallic coordination network for Zn-TPP and co-deposited Cu instead of an exchange. These two publications highlight that the underlying process of metal exchange is highly complex and critically depending on the exact nature of the environment, i.e. vacuum vs. solution, and the metal species involved as well as the supporting surface. A recent study on a Cu-porphyrin network on a

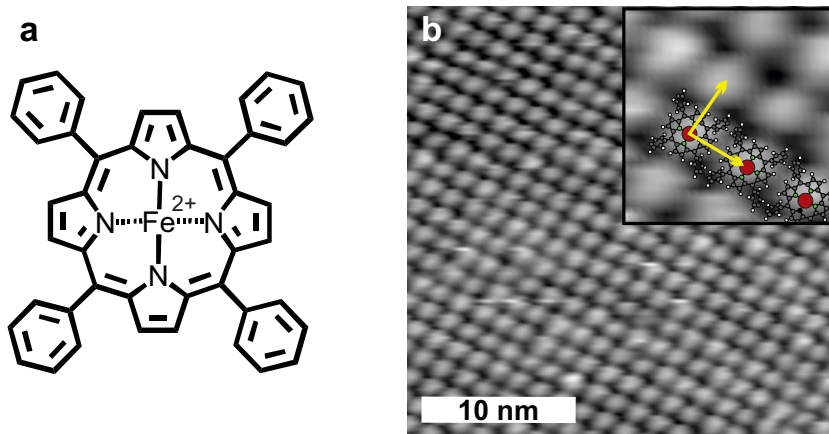
Cu(111) substrate demonstrates a hierarchical exchange of Cu by co-deposited Ni and Fe.<sup>[158]</sup> The authors claim a poor stability of Cu in the porphyrin cage resulting in a transmetalation process. Fe is assumed to be the most stable of the three tested metal centers.

Certainly, further studies are needed to explore on-surface transmetalation. Understanding underlying processes requires suitable analytical tools, such as XAS probing the electronic structure. The chemical environment highly influences the electronic structure of the involved metal centers yielding information about a possible cationic exchange.

This chapter describes the exchange of Fe and Cu chelated in a porphyrin macrocycle by Co at the solid/vacuum interface. The topography of the self-assembled porphyrin network is investigated by STM and the exchange is studied by XAS. Sublimation of Co spontaneously substitutes Fe/Cu occupying its place in the tetrapyrrole ring on a Au(111) substrate at RT. The Co as additional metal center is deposited in an active way in contrast to the two published studies making use of the adatom gas of Cu(111) and annealing temperatures to initiate the substitution reaction.<sup>[155,156]</sup>

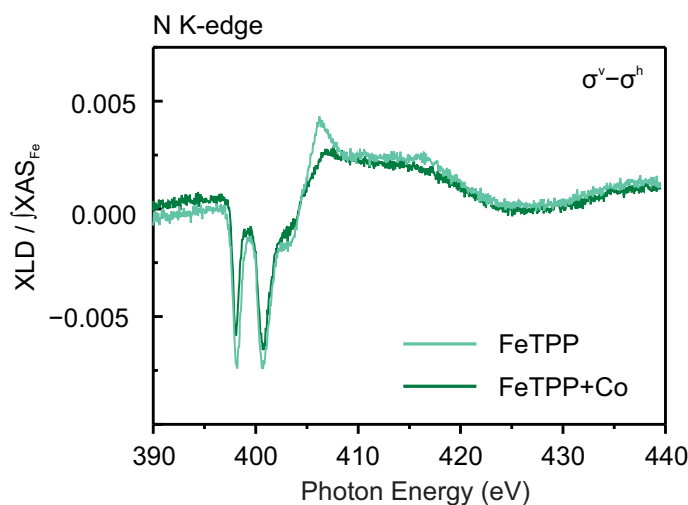
### 3.1 On-Surface Transmetalation of Fe-Tetraphenylporphyrin

The substitution of Fe by Co in a TPP molecular network was actively initiated by Co deposition onto the FeTPP network. FeTPP (Fig. 3.1 a) self-assembles in a highly ordered almost square structure on Au(111) with lattice constants of about 1.5 nm indicated by yellow vectors in an exemplary STM image (Fig. 3.1 b). One molecule is encountered per unit cell. Sublimation of Co to FeTPP (FeTPP+Co) leaves the monolayer structural unchanged.<sup>[103]</sup> The deposited amount of Co is slightly exceeding the stoichiometric amount of Fe (Co/Fe  $\approx$  1.2). The electronic structure of involved elements is investigated by XAS.



**Figure 3.1:** Self-assembled FeTPP network. (a) Structural formula of FeTPP; (b) STM image of a FeTPP-monolayer ( $I_{\text{tunnel}} = 1.0 \text{ nA}$ ;  $U_{\text{bias}} = 1.0 \text{ V}$ ), Inset:  $(10 \times 10) \text{ nm}^2$  zoom-in, yellow vectors indicate the lattice constants of about 1.5 nm. A model of the molecule is superimposed; color code: N (green), C (black), H (white), Fe (red).

The N K-edge represents the organic backbone stabilizing the metal center. The spectra are normalized to corresponding XAS at the Fe L<sub>2,3</sub>-edge (Fig. 3.2) and demonstrates similar XLD ( $\sigma^v - \sigma^h$ ) for both systems FeTPP (light green) and FeTPP+Co (green). The minima in the XLD are assigned to  $\pi^*$  transitions, whereas the positive peaks are related to excitation into the  $\sigma^*$  molecular orbitals (MOs).<sup>[152,159,160]</sup> The four nitrogens of the porphyrin core of MPs are chemically equivalent due to the D<sub>4h</sub> symmetry.<sup>[152,154]</sup> Hence, the two minima and the shoulder at 398.2 eV, 400.7 eV and 403.4 eV are related to N 1s  $\rightarrow \pi^*$  transitions into various excited  $\pi^*$  states.<sup>[152,160]</sup> The peak positions are in good agreement with spectra reported in literature.<sup>[160]</sup> The maximum of FeTPP at 406.2 eV is shifted to 406.8 eV and of reduced intensity upon Co deposition.

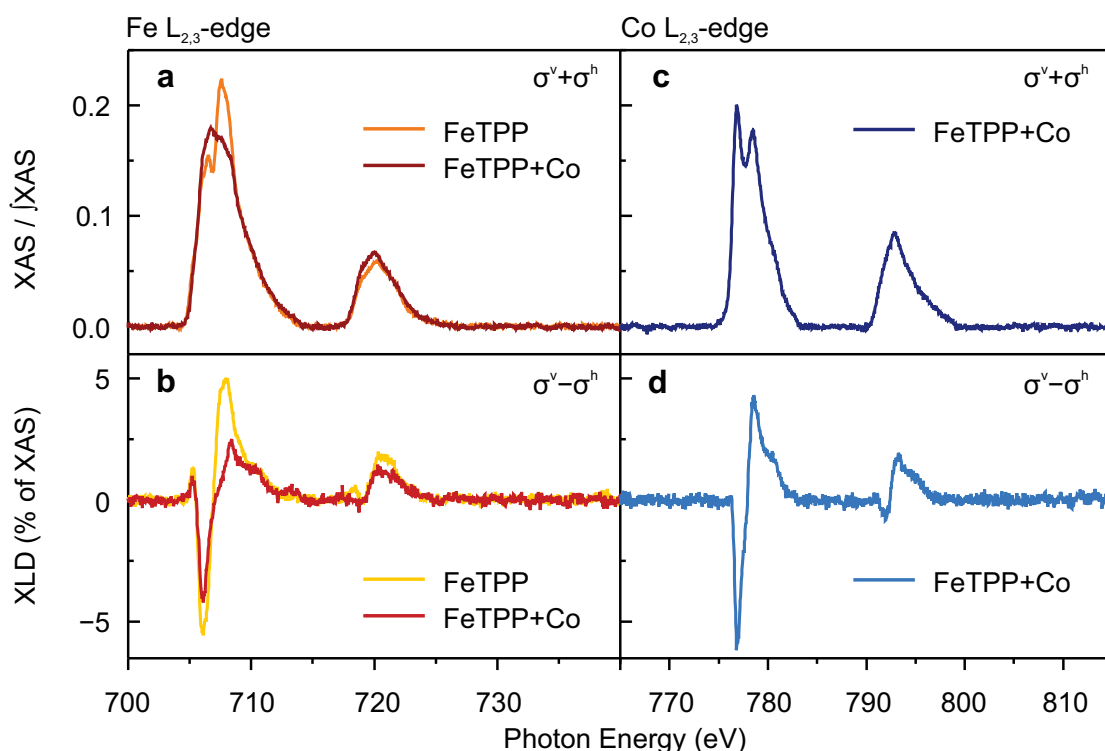


**Figure 3.2:** N K-edge of FeTPP and FeTPP+Co. XLD ( $\sigma^v - \sigma^h$ ), normalized to XAS of corresponding Fe L<sub>2,3</sub>-edge, color code: FeTPP (light green), FeTPP+Co (green).

The small differences demonstrated for the two systems can be attributed to the diversity of different samples and bedevil a conclusion about the influence of the second metal to the coordinating nitrogens. Therefore, a dramatic change of the coordinating ligand upon Co deposition is not verifiable at N K-edge.

The Fe L<sub>3</sub>-edge ( $\sigma^v + \sigma^h$ ) of FeTPP exhibits a multiplet structure with maxima located at 706.5 eV and 707.6 eV (Fig. 3.3 a, orange). The multiplet structure stems from the coordination environment applied by the porphyrin core to the Fe center.<sup>[161]</sup> The strong absorption at the Fe L<sub>2,3</sub>-edge is preserved after Co sublimation. However, its multiplet structure is strongly diminished which is typically reported for metallic Fe (Fig. 3.3 a, red).<sup>[162,163]</sup> FeTPP+Co depicts only one maximum at 706.5 eV which is in accordance with the first maximum of pristine FeTPP. The shoulder at 707.6 eV is reminiscent of the second peak of pristine FeTPP indicating a reduced influence of pristine FeTPP to the XAS signal. Thus, the spectrum of FeTPP+Co reflects presumably a superposition of molecular FeTPP and a metallic contribution.

For the FeTPP monolayer the XLD signal is clearly visible (Fig. 3.3 b, yellow), demonstrating an anisotropy in the electronic structure of the Fe cation probed by diverse polarization of



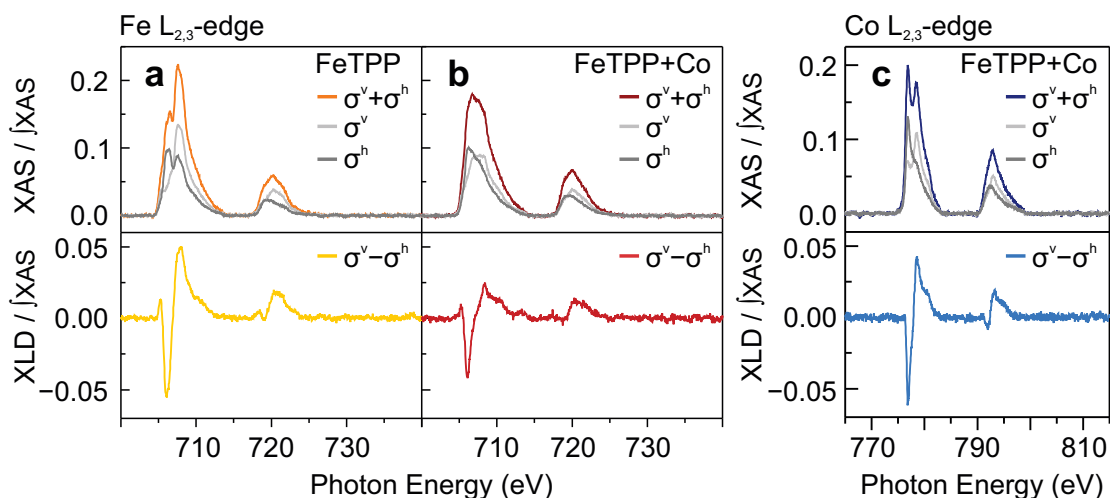
**Figure 3.3:** XAS ( $\sigma^v + \sigma^h$ ) and XLD ( $\sigma^v - \sigma^h$ ) at Fe and Co  $L_{2,3}$ -edges of FeTPP and FeTPP+Co.  $L_{2,3}$ -edges are normalized to the corresponding integral of XAS. Fe  $L_{2,3}$ -edge: (a) XAS, color code: FeTPP (orange), FeTPP+Co (red) and (b) XLD, color code: FeTPP (yellow), FeTPP+Co (light red); Co  $L_{2,3}$ -edge: (c) XAS of FeTPP+Co (dark blue) and (d) XLD of FeTPP+Co (light blue).

exciting x-rays. The anisotropy originates from the ligand field determining the electronic structure of Fe. After Co deposition (Fig. 3.3 b, light red), the spatial shape of the spectra is preserved and only the high relative weight of the  $L_3$  shoulder at approximately 708 eV identifies a difference between the two systems.

This findings indicate a changed environment of Fe in many molecules upon Co deposition towards a significantly more metallic character as XAS averages over large areas. Whether this is simply due to the presence of Co cluster insulate the Fe, or a transmetalation cannot be concluded from the Fe  $L_{2,3}$ -edge alone.

The Co  $L_{2,3}$ -edge exhibits a clear multiplet (Fig. 3.3 c) accompanied by a pronounced linear dichroism (Fig. 3.3 d). The maxima of the double peak  $L_3$ -edge are located at 776.8 eV and 778.5 eV. The presence of a multiplet structure in combination with the clear electronic anisotropy determined by XLD suggests chelated Co<sup>[164]</sup> rather than metallic Co<sup>[163,165]</sup> in the sample. The most likely hypothesis that explains these results is a transmetalation of Fe by Co.

The drastic change of the Fe electronic structure upon Co sublimation is not only reflected by  $\sigma^v + \sigma^h$  at the Fe  $L_{2,3}$ -edge discussed above, but also by the separated polarization directions (Fig. 3.4).  $\sigma^h$  illustrates clearly the diverse electronic structure of the Fe center in pristine FeTPP



**Figure 3.4:** XAS of separated polarization directions of FeTPP and FeTPP+Co. Vertical ( $\sigma^v$ , light grey) and horizontal ( $\sigma^h$ , grey) polarized x-rays at the Fe  $L_{2,3}$ -edge of (a) FeTPP: XAS ( $\sigma^v + \sigma^h$ , orange), XLD ( $\sigma^v - \sigma^h$ , yellow); (b) FeTPP+Co: XAS (red), XLD (light red) and (c) Co  $L_{2,3}$ -edge of FeTPP+Co: XAS (dark blue), XLD (light blue). Both absorption edges are normalized to corresponding integral of XAS.

and FeTPP+Co (Fig. 3.4 a, b) supporting the hypothesis of an altered chemical environment due to Co deposition. The double peak shape of ( $\sigma^v + \sigma^h$ ) of pristine FeTPP is mostly generated by  $\sigma^h$ , whereas the  $\sigma^v$  signal is mainly unstructured.

Both polarization directions of FeTPP+Co lack a clear multiplet structure. However, the spectra differ slightly from each other in contrast to a purely metallic signal (Fig. 3.4 b).<sup>[164]</sup> The anisotropy between  $\sigma^v$  and  $\sigma^h$  is demonstrated by the presence of a XLD. The electronic structure of metallic components consists of an isotropic band structure resulting in an independence of polarization direction of the exciting x-rays visible as a multiplet-free XAS. Thus, it strengthens the idea of a superposition of both chelated and metallic Fe. Although  $\sigma^v$  is also featureless for the molecular network itself, the spatial shape is sharp, while FeTPP+Co is broad most probably resulting from hybridization of the orbitals typical for a metallic state. The spatial shape of the XLD is similar before and after Co deposition. This is surprising when considering the large changes of XAS spectra.

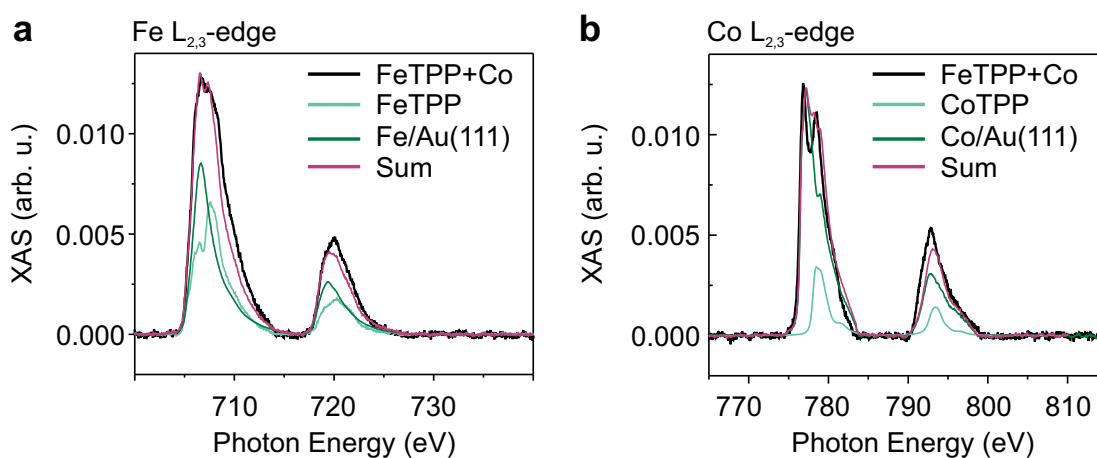
At the Co  $L_{2,3}$ -edge, both  $\sigma^v$  and  $\sigma^h$  (Fig. 3.4 c) show a multiplet leading to the double peak shape of the overall XAS. The varying spectra according to the polarized x-rays point to an electronic anisotropy of Co which can be explained by a ligand field.<sup>[164]</sup> As TPP exclusively offers one coordination site, the coordinated Co can only be embedded within the macrocycle. Realization of a chelated Co implies removal of Fe center from the porphyrin macrocycle forming a cobalt tetraphenylporphyrin (CoTPP) molecule. However, the presented XAS deviates from reported CoTPP.<sup>[164]</sup> The measured peak positions of the  $L_3$ -edge are shifted to higher energies in respect to the reported spectra and exhibits only one defined maximum together with a small shoulder. However, the experimental conditions differ in substrate and temperature from those reported here. For instance, the authors determined a strong influence of

### 3.1. On-Surface Transmetalation of Fe-Tetraphenylporphyrin

the Ag(111) substrate on the electronic structure of the Co center explaining the discrepancy between the two studies. Nonetheless, the formation of CoTPP is a suitable explanation for the varying XAS.

The hypothesis of a cation exchange is consistently evidenced at Fe and Co  $L_{2,3}$ -edge, as it explains plausibly the changes of the electronic structure upon Co deposition onto FeTPP. In contrast, the N K-edge could not provide further information about the position of co-deposited Co.

The XAS multiplet structure at Co  $L_3$ -edge can be explained by a ligand field generated by the four pyrrole nitrogen atoms of the porphyrin ring.<sup>[164]</sup> Consequently, Fe has to be reductively expelled from the porphyrin transforming into a metallic state which is confirmed by the lack of multiplet structure at the Fe  $L_3$ -edge after Co deposition.<sup>[162,163]</sup> The metallic Fe on the surface strongly contributes to the XAS signal leading to the superposition of two contributions at Fe  $L_{2,3}$ -edge. Similarly, the excess Co stays metallic and probably forms cluster on the surface contributing also to the Co signal. The convolution of XAS from coordinated metal species in the porphyrin and those in the cluster makes it difficult to unambiguously decompose the multiplet at the Fe and Co  $L_{2,3}$ -edge. The superposition of metallic and molecular Co contribution might be also an explanation for the different XAS line shape of *in situ* prepared CoTPP (generated by transmetalation of Fe by Co in the TPP network) compared to reported CoTPP<sup>[164]</sup>.



**Figure 3.5:** Superposition of metallic cluster and coordinated metal center at (a) Fe  $L_{2,3}$ -edge and (b) Co  $L_{2,3}$ -edge. Color code: recorded spectra of FeTPP+Co (black); superposition (pink):  $\sum[a \cdot \text{FeTPP} + b \cdot \text{Fe/Au(111)}]$  and  $\sum[a \cdot \text{CoTPP} + b \cdot \text{Co/Au(111)}]$ , respectively. At the Fe  $L_{2,3}$ -edge both Fe/Au(111) (green) and pristine FeTPP (light green) are measured. While at the Co  $L_{2,3}$ -edge Co/Au(111) (green) is measured and CoTPP/Ag(111) (light green) is taken from multiplet calculations presented in Ref.<sup>[164]</sup>.

For a quantitative evaluation of the metal exchange ratio as well as to support the hypothesis of the present metallic states, the XAS of FeTPP+Co was reproduced by the assumed individual components (Fig. 3.5). For this purpose, the weighted sum of pristine FeTPP and Fe cluster on Au(111) was compared to the measured FeTPP+Co spectrum. The shape of the FeTPP+Co XAS

signal is well reproduced by varying the ratio between the two individual spectra (Fig. 3.5 a) at the Fe L<sub>2,3</sub>-edge. Within this simple approach, the ratio between FeTPP and metallic Fe is roughly 0.4, i.e. more than half of Fe is substituted by Co.

The same analysis was performed for the Co L<sub>2,3</sub>-edge. The peak can be deconvoluted by summing pure CoTPP<sup>[164]</sup> and Co/Au(111) spectra (Fig. 3.5 b) indicating a superposition of both also at Co L<sub>2,3</sub>-edge. However, at the Co absorption L<sub>2,3</sub>-edge the fit and the corresponding measured spectra are not in perfect agreement. This discrepancy might be explained by the theoretical data of CoTPP taken from multiplet calculations<sup>[164]</sup>, while only Co/Au(111) was measured within the presented data set. The relative weight of CoTPP is found to be small in the spectra, showing that only a fraction of deposited Co (0.2) is exchanged with Fe.

A missing reference system hinders the direct comparison of the two ratios determined by this simple fitting model. However, the number of coordinated Fe centers determines the amount of available coordination site. Therefore an exchange rate of Fe by Co of about 0.4 can be estimated.

The used model assumes that FeTPP+Co can be decomposed into FeTPP or CoTPP, Fe and Co cluster. The cluster spectrum is likely not strongly influenced by the presence of molecules. However, it is not clear that the Fe(Co)TPP spectra will not be influenced by the presence of additional metal cluster. Taking this into account the agreement between the data and this simple model is surprisingly good. In particular, this good agreement gives a strong experimental proof of the transmetalation processes involved in this system. Additionally, it provides a rough estimation of the transmetalation ratio. Due to this simplified qualitative approach, it can be concluded on a rough transmetalation ratio of about 50 %.

## 3.2 Mechanism of the Redox Transmetalation in Vacuum

The mechanism underlying the metal exchange can be expected to be fairly complex because a number of different bond formation and breaking processes are involved. The transmetalation mechanism has been widely studied in solution-based experiments, but it is still far from being fully understood.<sup>[146–150]</sup> Most of the reports agree on a S<sub>E</sub>2 -mechanism involving a bimetallic atop complex as intermediate. A free-base porphyrin intermediate is excluded in most of the solution-based studies due to slow reaction rates.<sup>[146,148,150]</sup> However, in liquid involved metal centers are always coordinated in complexes. Therefore the reaction is not only based on the redox reaction of the metal centers (M), but also by a ligand (R) exchange (<sup>1</sup>M–R + <sup>2</sup>M–R' → <sup>1</sup>M–R' + <sup>2</sup>M–R). Contrary, in UHV the initial situation contains only one metal center coordinated in an organic matrix, while the second metal is sublimed in a metallic state. Therefore, in UHV the redox transmetalation involves one metallic reactant

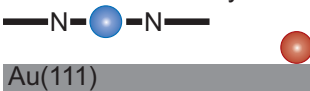
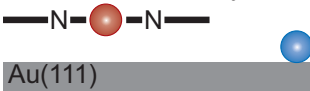
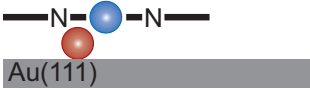
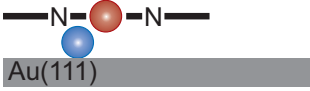
---

\* DFT calculations presented in this section are performed by Paula Abufager and H. Fabio Busnengo (Instituto de Física Rosario and Universidad Nacional de Rosario, CONICET-UNR, Rosario, Argentina): Calculations were performed with the VASP code<sup>[115]</sup> based on the slab-supercell approach and using the projector augmented-wave (PAW) method<sup>[166]</sup>. Charge analysis of the reactants followed Bader's method<sup>[167]</sup>.

### 3.2. Mechanism of the Redox Transmetalation in Vacuum

transforming into an oxidized metal center coordinated by the organic ligand ( $^1M^{Z+}-R + ^2M^0 \rightarrow ^1M^0 + ^2M^{Z+}-R$ ).

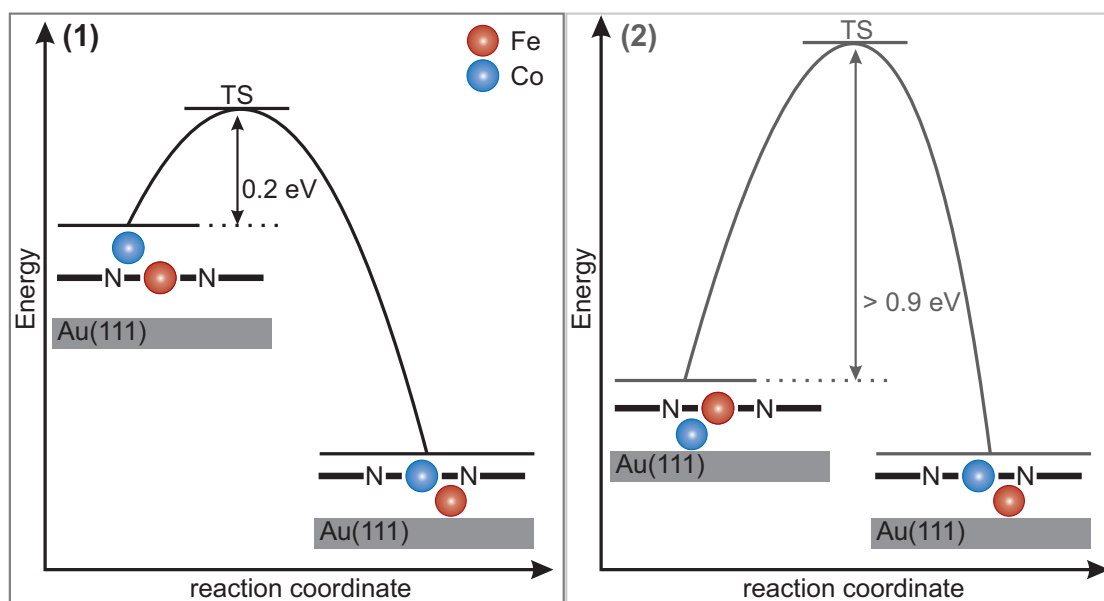
**Table 3.1:** Calculated energies for various configurations of CoTPP, FeTPP, Co and Fe adsorbed on Au(111). Color code: Co (blue), Fe (red), Au(111) (grey), schematic side view of the organic backbone (black).

Caption	Configuration	Energy (eV)
<b>a</b>	adsorbed Fe far away from CoTPP/Au(111) 	1.9
<b>b</b>	adsorbed Co far away from FeTPP/Au(111) 	1.8
<b>c</b>	Fe sandwiched between CoTPP and Au(111) 	0.0
<b>d</b>	Co and Fe stabilized underneath TPP/Au(111) 	0.2

Experimental data provide only information about the pristine molecular network and the partial exchanged bimetallic system. Therefore, theory can illuminate possible reaction pathways and might help to evaluate the probability of a transmetalation at RT. Indeed the transmetalation is supported by theory allocating CoTPP (Tab. 3.1a) a higher thermodynamic stability than FeTPP (Tab. 3.1b). Consistently, the most stable bimetallic configuration would be a CoTPP molecule sandwiching Fe between the molecule and the surface (Tab. 3.1c). In this configuration the Fe atom acts as an additional linker between the MP and the Au(111) surface. The opposite configuration stabilizing Co between FeTPP and the Au(111) substrate (Tab. 3.1d) is thermodynamically less favored by about 0.2 eV. The thermodynamic advantage of the possible final states already suggests the preference of a transmetalation.

However, a thermodynamically favored final state needs to be available through a sufficiently low reaction energy barrier to drive the transmetalation at RT. Two possible initial states are proposed to reach the most stable final state of CoTPP stabilizing Fe below (Fig. 3.6). Reaction pathway one (Fig. 3.6, black) starts with Co attacking the FeTPP molecule from the top. The sublimed metallic Co center lands on the macrocycle and accommodates eventually close to the Fe center within the macrocycle following a *trans* attacking position for the exchange. The reaction barrier is calculated of approximately 0.2 eV. The surprisingly small reaction barrier could easily be overcome at RT at which samples are prepared.

Contrary, reaction pathway two (Fig. 3.6, grey) initiates with a Co center which diffuses over the Au(111) surface. The sublimed Co arrives on top of the Au(111) substrate and moves under-



**Figure 3.6:** Reaction barriers of the redox transmetalation on Au(111) transforming to the most stable configuration of metallic Fe (red) sandwiched between Co (blue) porphyrin and Au(111) surface starting from two diverse initial states (the organic backbone is shown schematically in black as side view): (1) Co attacking from the top (*trans*), to the molecule through a transition state (TS) and (2) Co first landing on Au(111) and diffusing to the FeTPP attacking from below (*cis*).






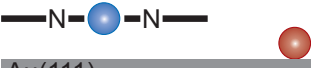
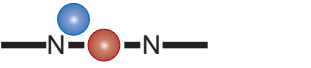
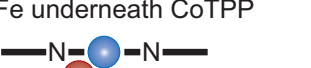
neath the molecular layer close to the FeTPP. Thus, pathway two describes a *cis* configuration which faces steric hindrances as both the attacking position as well as the expelling position are underneath the molecule. This fact is expressed by the fairly high reaction barrier of at least 0.9 eV. Therefore, the most plausible initial state is identified as Co accommodated on top of the molecule reaching the final state through a reaction barrier of only ~ 0.2 eV.

As mentioned above, the transmetalation is expected to occur similar to a redox transmetalation ( $^1M^{z+}TPP + ^2M^0 \rightarrow ^2M^{z+}TPP + ^1M^0$ ) which requires a charge transfer between the two involved metal centers  $^1M$  and  $^2M$  ( $^1, ^2M$ : Co, Fe). The charge distribution is approached by Bader analysis (Tab. 3.2). Firstly, Bader analysis demonstrates the expected oxidized character of the metal centers coordinated to the TPP organic backbone in the gas phase. The oxidized state is expressed by charge reduction of 1.1 e for Fe and 1.0 e for Co. Concerning the experimental approach, the surface needs to be considered.

Indeed the influence of the surface is shown by a small reduction of Fe and Co in the molecule of about 0.1 e. Similarly, the non-coordinated single metal atoms adsorbed on Au(111) also get reduced of about 0.5 e and 0.3 e for Fe and Co, respectively. These interactions already illustrate the influencing character of both the organic backbone and the Au(111) substrate. A charge transfer between the two metal centers is caused when moving the second metal center closer to the molecule. The Co atom accommodated close to the Fe center of the molecule has a charge of 8.4 e pointing to an initiated oxidation, while Fe (7.0 e) starts to be reduced with respect to the FeTPP adsorbed separated on Au(111). Although the values are

### 3.2. Mechanism of the Redox Transmetalation in Vacuum

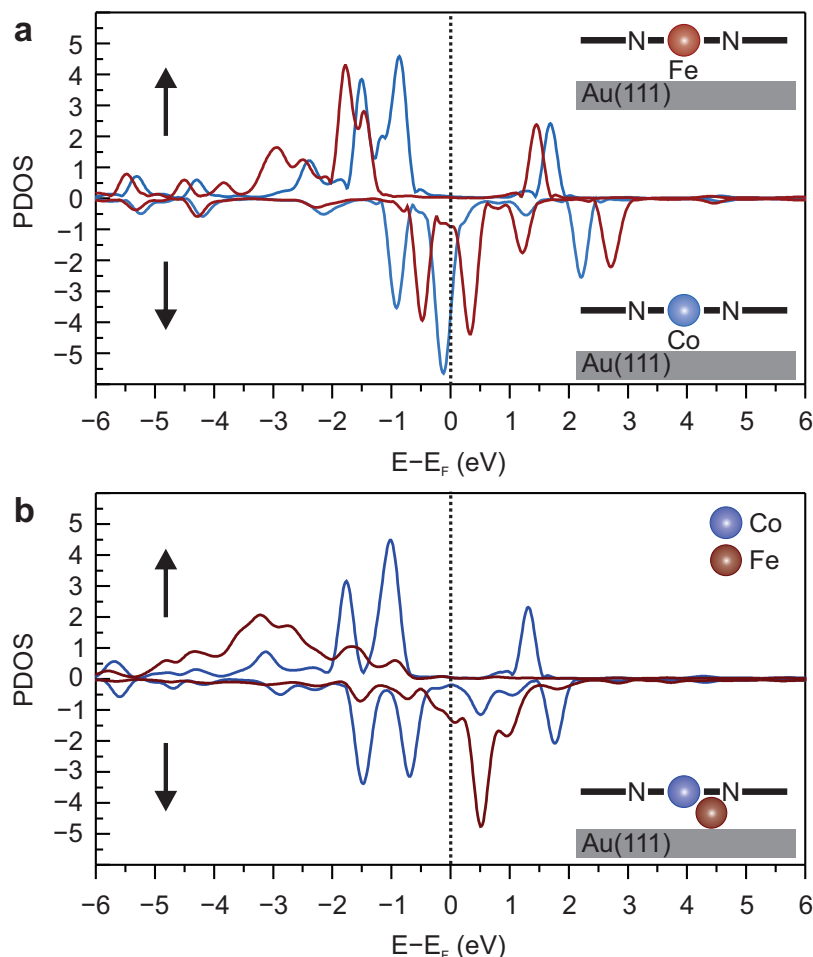
**Table 3.2:** Bader analysis of various combinations of CoTPP, FeTPP, Co and Fe. Charges  $q$  in e of both metal centers, Fe and Co as well as the components of the molecular backbone, N, C, H are depicted. In addition, the total number of electrons of the molecule is shown. Species calculated for the gas phase are indicated by a grey background. Species adsorbed on the Au(111) surface have an uncolored background. Color code for the schematic configurations: Co (dark blue), Fe (red), Au(111) (grey), schematic side view of the organic backbone (black).

	Species	$q(\text{Fe})$	$q(\text{Co})$	$q(\text{N})$	$q(\text{C})$	$q(\text{H})$	$q(\text{molecule})$
gas phase	atomic Fe 	7.9					
	atomic Co 		8.9				
	FeTPP 	6.8		24.6	174.5	25.9	231.8
	CoTPP 		7.9	24.5	174.7	25.6	232.7
adsorbed species	Co far away from FeTPP 	6.9	8.6	25.6	174.6	25.4	231.5
	Fe far away from CoTPP 	7.4	8.0	24.4	174.7	25.5	232.6
	Co on top of FeTPP 	7.0	8.4	24.4	175.0	25.3	231.7
	Fe underneath CoTPP 	7.2	8.2	24.5	174.9	25.2	232.8

still not comparable to the metallic state of Fe and the coordinated state of Co which would be alongside a redox transmetalation process, the tendency of a charge transfer points to the proposed transmetalation process utilizing presumably this configuration as initial state. The metallic character of Fe becomes even more clear when looking at the proposed final state where Fe is located between the CoTPP molecule and the Au(111) surface. With a charge of 7.2 e the Fe gets closer to the situation of single Fe adsorbed on Au(111) and thus explains the metallic character also demonstrated by XAS. Moreover, Co with 8.2 e is similar to adsorbed CoTPP.

In addition to the thermodynamic stability and the low reaction barrier for pathway one, Bader analysis consistently reports a charge transfer between the two involved metal centers as necessary for the transmetalation process. The unaltered charge distribution for N, C and

H leads to an organic backbone which is potentially uninvolved in the charge redistribution resulting in oxidized Co and reduced Fe.

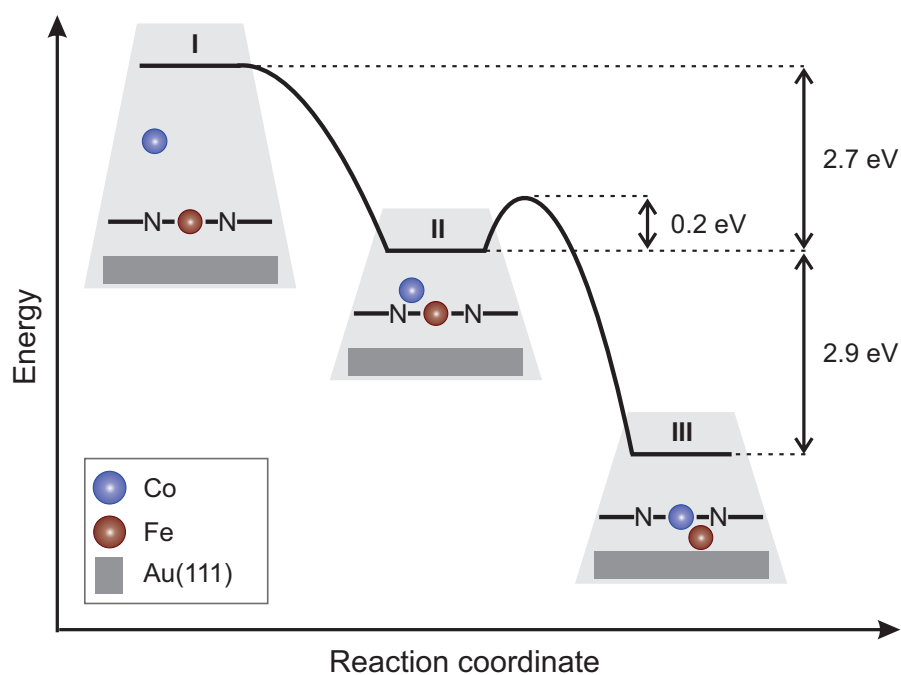


**Figure 3.7:** Projected density of states (PDOS) around the Fermi level  $E_F$  of (a) FeTPP (red) and CoTPP (blue) adsorbed on Au(111) and (b) the most probable final state (the organic backbone is shown schematically in black as side view): CoTPP+Fe with Fe sandwiched between CoTPP molecule and Au(111) surface: PDOS of Fe (wine), PDOS of Co (dark blue). Positive y-values are referring to spin up, negative y-values to spin down as marked by arrows on the left.

The redox transmetalation is also supported by looking at the projected density of states (PDOS) of the proposed final state and the two separated molecules. The discrete atomic orbitals expected for metals coordinated by organic ligands is clearly depicted by the PDOS of FeTPP and CoTPP (Fig. 3.7 a). The unoccupied atomic orbitals split in the ligand field are responsible for the multiplet structure demonstrated by XAS shown earlier (section 3.1). By looking at the final state in which the Fe atom sits between the CoTPP and the gold surface, the metallic character detected experimentally by XAS and determined theoretically in Bader analysis becomes clearly visible. Co still shows discrete atomic orbitals (dark blue), whereas Fe demonstrates a band like structure which is typical for a metallic state (wine).

### 3.2. Mechanism of the Redox Transmetalation in Vacuum

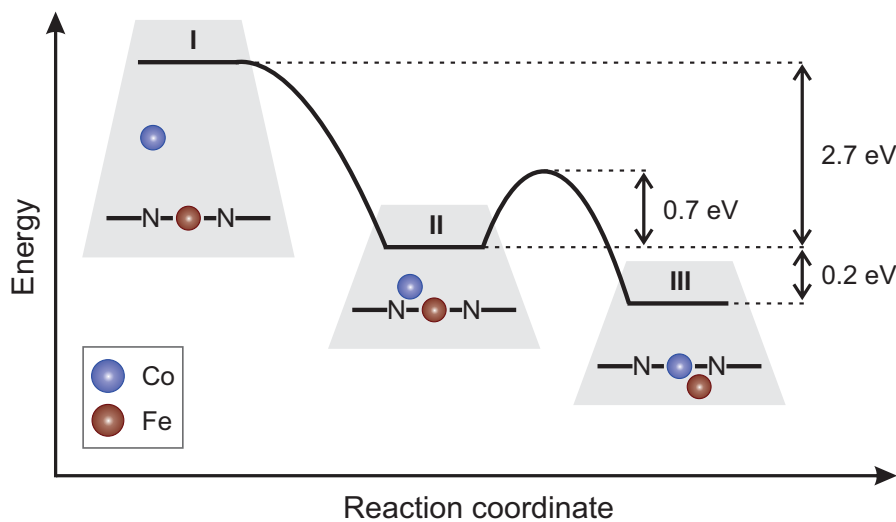
Both the charge transfer and accommodation of metal centers on the molecule is consistently reported by Vijayaraghavan *et al.* [164]. Subsequently, the oxidized Co expels the Fe which is simultaneously reduced and will be stabilized underneath the molecule. Experimentally, the proposed final state could not be confirmed definitely. Although STM provides molecular resolution, strong variations upon Co deposition were not evident in the images. Furthermore, the XAS clearly demonstrates a metallic Fe contribution. A single Fe atom located underneath the molecule might hybridize with the Au(111) surface producing a metallic-like band structure which could explain the featureless XAS. The hybridization with the surface is also in line with DFT findings showing an interaction of the separated metallic atom and the surface. However, the single Fe atom could be strongly influenced by the organic ligand on top resulting in a varied ligand field. In this case a diverse multiplet structure including a varied XLD would be expected which was not evident in the experimental spectra. The metallic state could be also explained by cluster formation. Admittedly, cluster were not visible in STM, thus only small cluster could justify the metallic signal. However, cluster formation might not be preferred from a thermodynamic perspective considered by DFT. Hence, a single Fe atom stabilized underneath the CoTPP as proposed by DFT seem to be more plausible than cluster of metallic Fe.



**Figure 3.8:** Proposed reaction pathway of Co (blue) substituting Fe (red) in FeTPP (schematic side view of the organic back bone in black) via transmetalation on Au(111). Molecular model of I) initial, II) intermediate, and III) final state. Calculated reaction energy barrier and energy differences are indicated.

The proposed redox transmetalation process is well supported by DFT calculations. The fact that CoTPP is thermodynamically favored is additionally assisted by a fairly low reaction energy barrier reaching the proposed most stable final state of Fe stabilized between CoTPP

and Au(111) (Fig. 3.8). The reaction is initiated by Co sublimed onto the network (Fig. 3.8 I), followed by Co adsorbing on the MP (Fig. 3.8 II). This reaction route might be even more plausible if Co reaches the initial state for the elementary step of Co substituting Fe before completely losing the 2.7 eV gained during the adsorption process on top of the molecule (Fig. 3.8 II). In this case the reaction barrier of  $\sim 0.2$  eV is easily overcome and the most stable final state (Fig. 3.8 III) is formed. Moreover, Bader analysis carves out the charge redistribution between the two metal centers which is in line with the suggested redox transmetalation reaction mechanism.

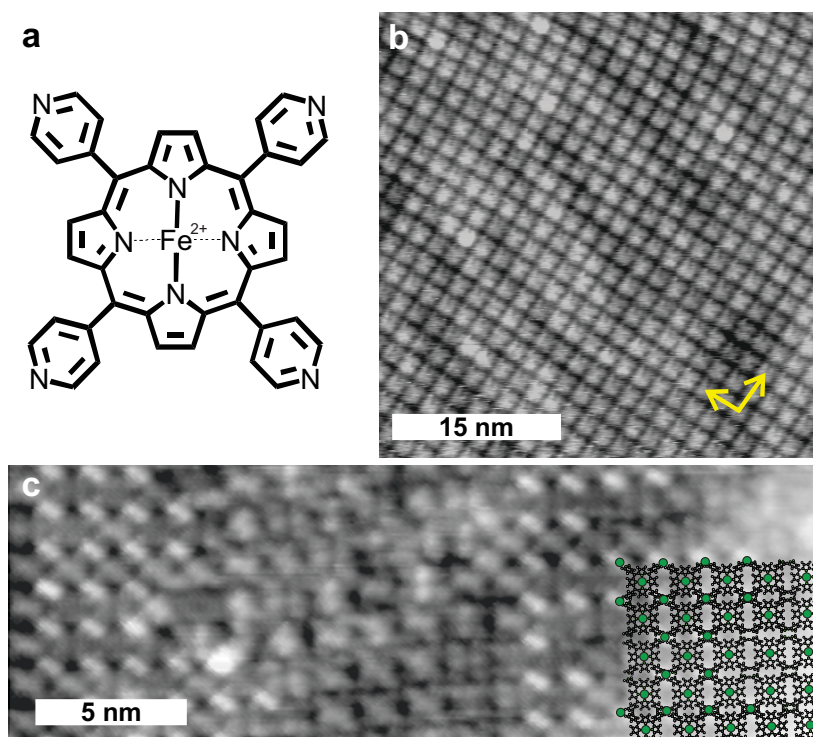


**Figure 3.9:** Effect of the surface on the reaction energy barrier of the proposed transmetalation reaction pathway. Co (blue) substituting Fe (red) in FeTPP (schematic side view of the organic backbone in black) via transmetalation in gas phase. Molecular model of I) initial, II) intermediate, and III) final state. Calculated reaction energy barrier and energy differences are indicated.

Interestingly, the fairly small reaction energy barrier of  $\sim 0.2$  eV increases significantly when driving the exchange without the Au(111) surface (Fig. 3.9). In the gas phase the reaction energy barrier is 3.5 times higher in respect to the calculated energy barrier of the on-surface reaction. Hence, the surface plays an important role as it facilitates the transmetalation process by reducing the reaction energy barrier between the intermediate (Fig. 3.9 II) and final state (Fig. 3.9 III) drastically.

### 3.3 Influencing Transmetalation by Pyridyl Peripheral Functional Groups

Peripheral functional groups can alter the electronic properties of the metal in the porphyrin by inductive or mesomeric effects. As a result the substitution barrier for a metal exchange might be influenced. Likely more prominent in the substitution reaction are the pyridyl groups of tetrapyrrolylporphyrin (TPyP) (Fig. 3.10 a) providing a second coordination site by the pyridyl nitrogens which are able to stabilize a second metal center.<sup>[103,127,128,168–170]</sup>

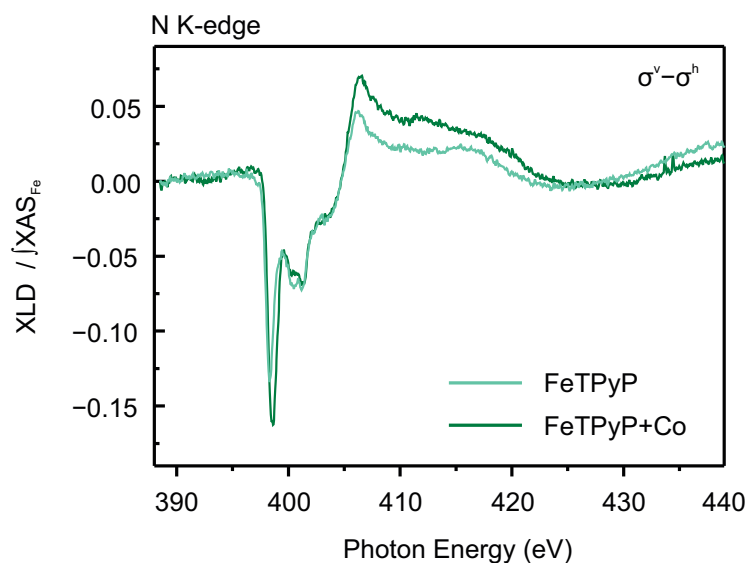


**Figure 3.10:** The FeTPyP and FeTPyP+Co network. (a) Structural formula of FeTPyP; (b) large scale STM image of FeTPyP+Co, yellow vectors indicate the lattice constants ( $I_{\text{tunnel}} = 0.29 \text{ nA}$ ;  $U_{\text{bias}} = 945 \text{ mV}$ ); (c) STM image of FeTPyP+Co including a schematic molecular structure superimposed ( $I_{\text{tunnel}} = 0.01 \text{ nA}$ ;  $U_{\text{bias}} = 1.2 \text{ V}$ ). Color code: Fe and Co (dark green), C (black), H (white), N (green).

Molecules self-assemble in a long-range ordered and dense network (Fig. 3.10 b) described by a  $(3.0 \times 2.9) \text{ nm}^2$  unit cell indicated by yellow vectors. Adjacent molecules are rotated by  $90^\circ$  with respect to each other forming the roughly square unit cell (see Ref. <sup>[103]</sup> for details). Occasionally, STM images upon Co deposition to the molecular network show protrusions in between the molecules located at the pyridyl groups (Fig. 3.10 c) identified as additional coordinated metal centers. Again, the system was investigated by XAS in order to look for indication of transmetalation.

The XLD profile at the N K-edge (Fig. 3.11) is similar to FeTPP (Fig. 3.2). The minima in the XLD located at 398.3 eV, 400.4 eV, 401.2 eV and the shoulder at 403.7 eV are assigned to N  $1s \rightarrow \pi^*$  transitions. <sup>[152,159,160]</sup>

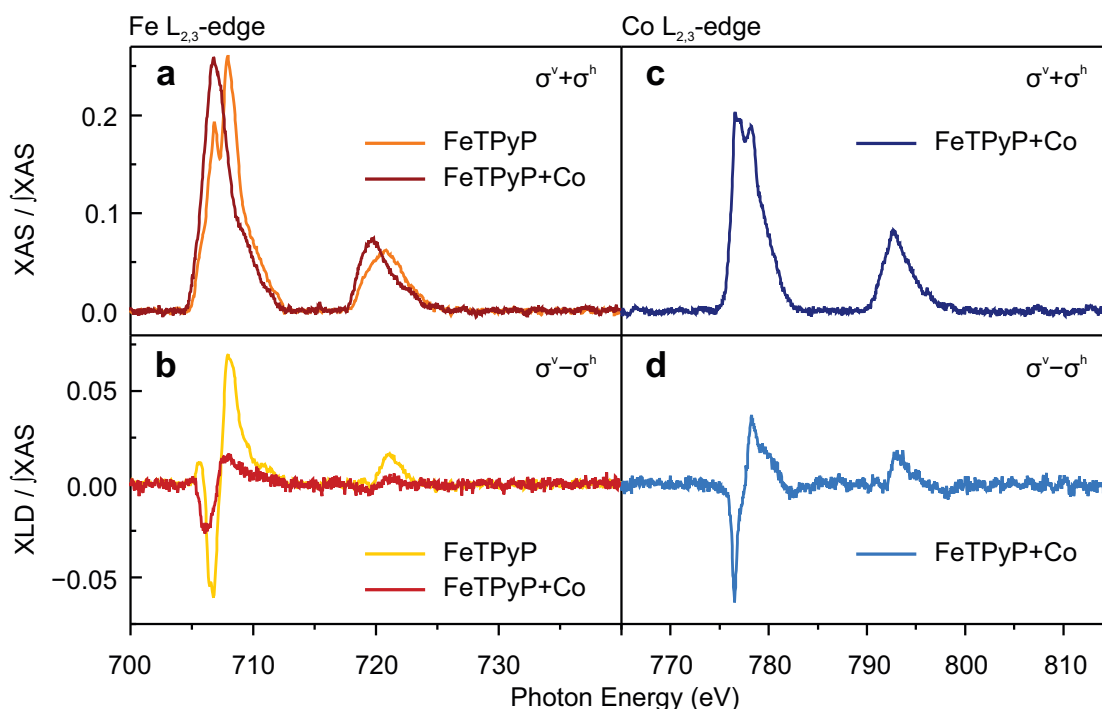
Similar to the N K-edge spectra of FeTPP, the positive peaks are related to excitation into the  $\sigma^*$  MOs. <sup>[152,159,160]</sup> The first maximum at N K-edge is at 406.3 eV with a higher intensity for the bimetallic system compared to the monometallic one. The second maximum is pronounced and easy to identify for FeTPyP at 416.1 eV while it is an undefined broad band for FeTPyP+Co. However, the reported differences of mono- and bimetallic system are not significant inhibiting a strong conclusion about the occupation of certain coordination sites or the influence of Co to the organic backbone.



**Figure 3.11:** N K-edge of FeTPyP and FeTPyP+Co. XLD ( $\sigma^v - \sigma^h$ ) at N K-edge, normalized to corresponding Fe  $L_{2,3}$ -edge, color code: FeTPyP (light green) and FeTPyP+Co (green).

Similar to the observation of Co deposition to FeTPP, the multiplet at the Fe  $L_{2,3}$ -edge of FeTPyP upon Co sublimation changes drastically. Pristine FeTPyP exhibits a double peak structure at the Fe  $L_3$ -edge (Fig. 3.12 a, orange) which resembles the shape of FeTPP (Fig. 3.3 a, orange), as a consequence of the coordinated Fe center<sup>[161]</sup>. The intensity of the first signal at 706.8 eV is diminished by 30 % with respect to the second peak at 707.9 eV. Co deposition onto FeTPyP removes the multiplet structure at the Fe  $L_{2,3}$ -edge (Fig. 3.12 a, red). The energy of the maximum (706.8 eV) is identical to the signal at lower energies of pristine FeTPyP. A small shoulder at 708.9 eV is the only evidence of an anisotropy. The lack of multiplet structure indicates again the formation of metallic Fe<sup>[162,163]</sup> and points again to a transmetalation of Fe by Co in the TPyP network.

Thus, the strongly reduced XLD signal of FeTPyP+Co (Fig. 3.12 b, light red) is attributed to chelated Fe having two possible coordination sites, one in the tetrapyrrole macrocycle and another one at the peripheral pyridyl groups. The small shift to lower energies indicates a different ligand field which is provided by the second coordination site at the pyridyl N. Consistently, the partial occupation of the pyridyl coordination site is supported by STM (Fig. 3.10 c). However, it remains unclear if the coordinated Fe sits exclusively at the periphery. Considering the TPP transmetalation, only an exchange of about 50 % is achieved. Thus, with similar experimental conditions, a 100 % exchange is also unexpected for TPyP. Most probably, the XLD represents a linear combination of two diverse ligand fields originating from residual Fe in the macrocycle and Fe coordinated at the periphery. A shift of the XLD by interaction with present metallic Co or Fe can be excluded as this shift was not observed for the FeTPP+Co system (Fig. 3.3).



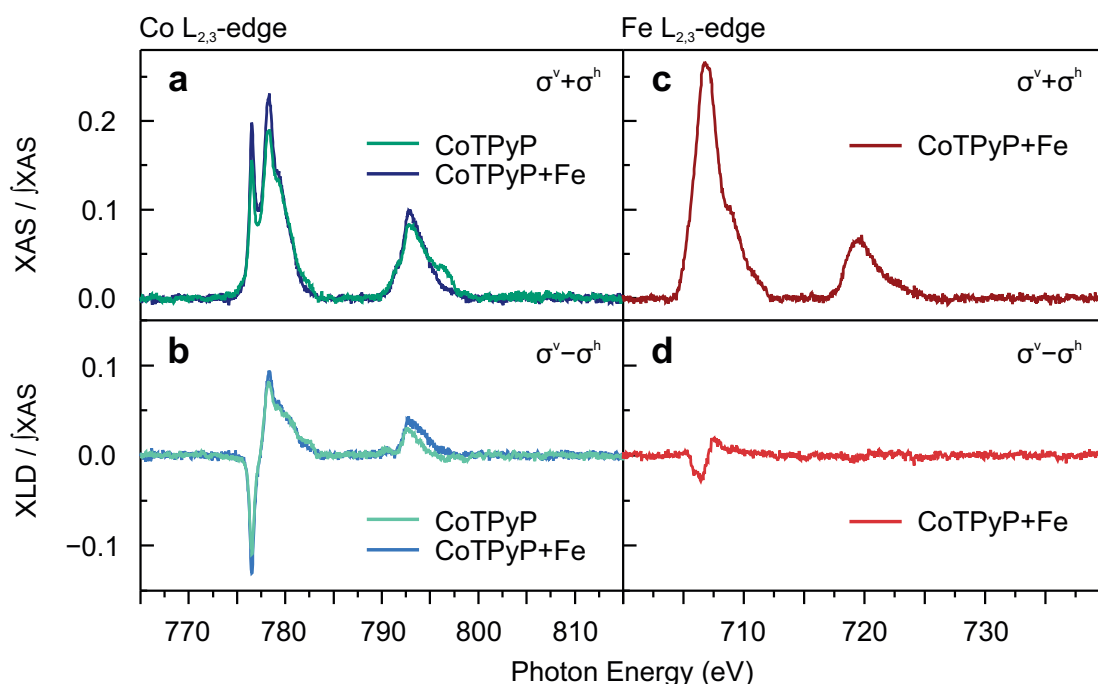
**Figure 3.12:** XAS ( $\sigma^v + \sigma^h$ ) and XLD ( $\sigma^v - \sigma^h$ ) of FeTPyP and FeTPyP+Co at Fe and Co  $L_{2,3}$ -edges.  $L_{2,3}$ -edges are normalized to the corresponding integral of XAS. Fe  $L_{2,3}$ -edge: (a) XAS of FeTPyP (orange) and FeTPyP+Co (red); (b) XLD of FeTPyP (yellow) and FeTPyP+Co (light red); Co  $L_{2,3}$ -edge: (c) XAS of FeTPyP+Co (dark blue) and (d) XLD of FeTPyP+Co (light blue).

The Fe  $L_{2,3}$ -edge depicts also the result of a transmetalation process. Due to the availability of a second coordination site, expelled Fe could accommodate at the pyridyl groups demonstrated by the shifted XLD. Nonetheless, a large amount of Fe has metallic character. The transmetalation is already evident at the Fe  $L_{2,3}$ -edge but becomes even more plausible when considering the Co  $L_{2,3}$ -edge.

The Co  $L_{2,3}$ -edge for FeTPyP+Co shows a double peak structured XAS (Fig. 3.12 c) and a strong XLD (Fig. 3.12 d) indicating Co coordinated by an organic ligand<sup>[164]</sup>. The multiplet is reminiscent of FeTPP+Co (Fig. 3.3 c) with comparable peak positions at 776.6 eV and 778.2 eV. The detection of coordinated Co cannot be attributed to a specific coordination site. Nonetheless, the ligand field of the macrocycle and the peripheric pyridyl is expected to deviate. Due to the similarity to FeTPP+Co, a major part of Co seems to be accommodated in the macrocycle. However, the differences in the ligand field might be not large enough to produce a diverse multiplet. Furthermore, STM constrains the presence of metal centers at the pyridyl coordination environment. By STM an explicit discrimination between Fe and Co accommodated at the peripheric N is impossible.

The transmetalation becomes clear considering both Fe and Co  $L_{2,3}$ -edges. The simultaneously reported absence of the multiplet structure at Fe  $L_{2,3}$ -edge and the similar shaped Co  $L_{2,3}$ -edge as FeTPP+Co supports the occurrence of a redox transmetalation as reported for

FeTPP. Due to the similarity of FeTPyP+Co and FeTPP+Co at Co  $L_{2,3}$ -edge, Co is assumed to be accommodated in the macrocycle. In contrast, Fe  $L_{2,3}$ -edge shows for all four cases FeTPP, FeTPP+Co, FeTPyP and FeTPyP+Co different shaped spectra demonstrating a variety of chemical environments. The availability of the second coordination site is not inhibiting the exchange explaining the large metallic character at Fe  $L_{2,3}$ -edge, but influences additionally the Fe environment which is evident from a shifted XLD. STM images clearly show that some coordination sites at the periphery are occupied by metal centers but it remains unclear if they are exclusively occupied by Fe or Co or rather by a mixture of both metals.



**Figure 3.13:** XAS of CoTPyP and CoTPyP+Fe. Spectra are normalized to corresponding integral of XAS. Co  $L_{2,3}$ -edge: (a) XAS ( $\sigma^v + \sigma^h$ ) of CoTPyP (green) and CoTPyP+Fe (dark blue); (b) XLD ( $\sigma^v - \sigma^h$ ) of CoTPyP (light green) and CoTPyP+Fe (light blue); Fe  $L_{2,3}$ -edge: (c) XAS of CoTPyP+Fe (red) and (d) XLD of CoTPyP+Fe (light red).

Although DFT finds CoTPP as thermodynamically most stable configuration, the reaction might be kinetically driven. Therefore, the back reaction Fe substituting Co in a CoTPyP molecular network is investigated experimentally.

The XAS of CoTPyP (Fig. 3.13 a, green), which shows identical multiplet shape and peak positions as FeTPP+Co or FeTPyP+Co, supports the hypothesis that this is a result of Co being located within the porphyrin macrocycle. The Co  $L_{2,3}$ -edge structure and intensity is preserved after Fe deposition (Fig. 3.13 a). Moreover, the XLD signal remains essentially unaffected by the presence of Fe (Fig. 3.13 b). Additionally, the Fe  $L_{2,3}$ -edge (Fig. 3.13 c) demonstrates metallic characteristics with a low-intense XLD (Fig. 3.13 d). As Fe is deposited in a metallic state on the network it suggests that the deposited Fe is poorly interacting with the organic ligand to form metal-organic bonds. Consistently, both XAS and XLD of Fe  $L_{2,3}$ -edge resemble FeTPyP+Co.

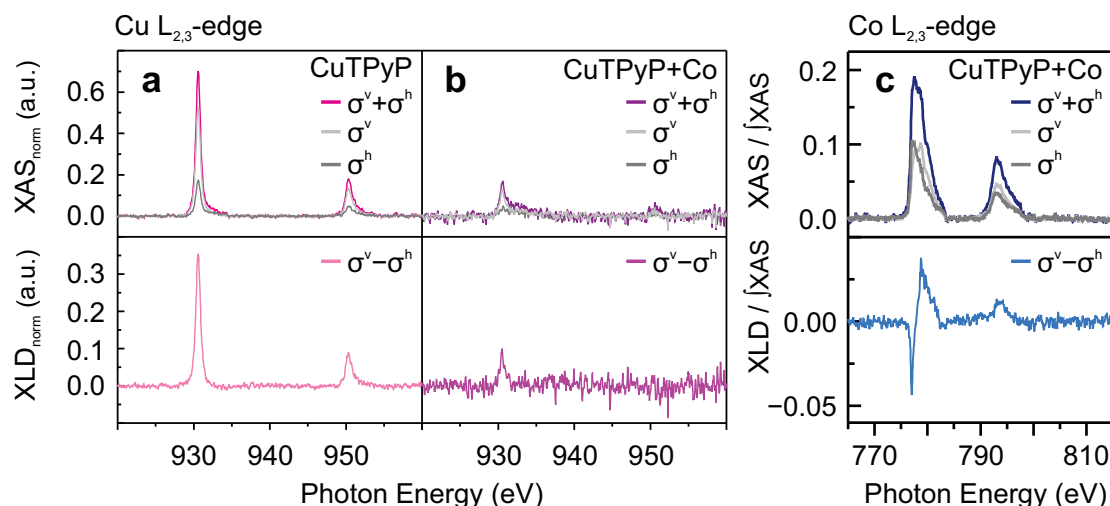
Peak position and shoulder of XAS lie at identical energies. Furthermore, the XLD is equally centered as FeTPyP+Co which was attributed to the influence of the ligand field originating from the peripheric coordination sites. Thus, the small XLD visible at Fe  $L_{2,3}$ -edge is also assigned to Fe accommodated at the peripheric pyridyl N which is generally accessible for metal-organic coordination bonds.<sup>[127,128]</sup>

A transmetalation of Co by Fe in the TPyP network on Au(111) can be excluded. However, Co substitutes Fe in TPyP. Both additionally sublimed Fe and expelled Fe accommodate partially at the peripheric pyridyl groups.

### 3.4 Transmetalation of CuTPyP by Cobalt

Transmetalation is highly dependent on the nature of the metal atoms involved as discussed for the cation exchange in dissolved porphyrins.<sup>[147]</sup> While the co-deposition of Co to FeTPP or FeTPyP monolayers on Au(111) leads to an exchange of the central Fe atom by Co, the inverse sample preparation showed no evidence for a cation exchange. In previous studies, Cu was shown to induce transmetalation in MPs.<sup>[155,156]</sup> Here, the CuTPyP network will be exposed to Co co-deposition and the effect of the deposited second metal center is explored.

CuTPyP generates a narrow  $L_3$ -edge at 930.6 eV and a  $L_2$ -edge at 950.3 eV. The absorption is determined by a  $d^9$  electron configuration of  $Cu^{2+}$  (Fig. 3.14 a, top) providing exclusively one final state.<sup>[171]</sup> Since the hole is located in the  $3d_{x^2-y^2}$ <sup>[171]</sup> CuTPyP/Au(111) is characterized by an intense positive XLD signal at the Cu  $L_{2,3}$ -edge (Fig. 3.14 a, bottom).



**Figure 3.14:** Cu and Co  $L_{2,3}$ -edges of CuTPyP and CuTPyP+Co. Cu  $L_{2,3}$ -edge of vertical ( $\sigma^v$ , light grey) and horizontal ( $\sigma^h$ , grey) polarized x-rays, XAS ( $\sigma^v + \sigma^h$ ) and XLD ( $\sigma^v - \sigma^h$ ) at Cu  $L_{2,3}$ -edge, normalized to the integral of XAS of CuTPyP at Cu  $L_{2,3}$ -edge (a) CuTPyP: XAS (pink), XLD (light pink); (b) CuTPyP+Co: XAS (purple), XLD (light purple); (c) Co  $L_{2,3}$ -edge, normalized to corresponding integral of XAS: XAS (dark blue), XLD (light blue).

After cobalt sublimation, the XAS and XLD signals have almost vanished and a large noisy background was observable, which is assigned to a  $d^{10}$  configuration (Fig. 3.14 b). XAS at Cu  $L_{2,3}$ -edge is normalized to the integral of XAS of CuTPyP due to the  $d^9 - d^{10}$  transition. The  $L_3$ -edge is still located at 930.6 eV. A  $d^{10}$  configuration is most probably traced back to metallic Cu in accordance with the hypothesis of a cation exchange as shown for FeTPP+Co and FeTPyP+Co.

The Co  $L_{2,3}$ -edge supports the cationic exchange by confirming the presence of coordinated Co evident by a pronounced XLD (Fig. 3.14 c). XAS is dissimilar to the XAS of CoTPyP (Fig. 3.13 a) demonstrating a more metallic signal without a significant multiplet. The pronounced metallic character stems from an excessive Co supply during the experiment, which cannot be incorporated into the MOCN. However, the XAS can be described by a double peak at 777.5 eV and 778.5 eV together with a shoulder at 779.8 eV. The energies of the double peak are comparable to CoTPyP (Fig. 3.13 a). The shoulder is reminiscent of Co/Au(111) but the peak position is located at different energy. The strong XLD (Fig. 3.14 c, bottom) shows similar shape as CoTPyP (Fig. 3.13 b) clearly evidencing the large amount of coordinated Co. The  $d^{10}$  Cu and coordinated Co with similar shaped XLD as CoTPyP indicate a transmetalation also for this particular system.

The exchange of Cu by Co goes along with the assumption by Rieger *et al.* <sup>[158]</sup> indicating the Cu-porphyrin bond as weak. However, the expelled Cu lies in contrast to the observation of Shen *et al.* <sup>[156]</sup> demonstrating exactly the opposite when Co-phthalocyanine interacts with the adatom gas of the Cu(111) surface at elevated temperatures. Once more the complexity of the on-going processes and the dependence on the experimental conditions is emphasized.

## 3.5 Conclusion and Outlook

Redox transmetalation determined by XAS is induced by Co deposition on Fe/Cu porphyrin networks. Although the TPyP molecular network offers a second coordination site by pyridyl groups, the exchange is preferred. Expelled metal centers turn metallic, likely residing between molecule and surface. The process occurs at RT indicating low reaction barriers. DFT suggests a thermodynamic driven exchange of Fe by Co, calculated for the TPP ligand. The transmetalation is initiated by Co sitting on top of the macrocycle going through a reaction barrier of  $\sim 0.2$  eV to the most stable final state. As final state, CoTPP stabilizing the expelled Fe in the sandwich configuration is proposed. The surface seems to support the transmetalation process as the calculated reaction barrier is significantly increased to 0.7 eV when calculating the reaction pathway for the gas phase.

The Co  $L_{2,3}$ -edge presented similar shape and peak positions for all presented systems which might be an additional hint that Co is actually bound in the macrocycle. The thermodynamic driving force is confirmed as the back reaction of Fe substituting Co is unobserved. The dependence on using either CoTPyP or FeTPyP networks as starting point for preparing the bimetallic electrocatalyst by Fe or Co co-deposition in a second step reported in section 2.4 <sup>[103]</sup>

concerning their electrocatalytic performance towards the OER might be explained by the transmetalation occurring only for the FeTPyP+Co system.

Nevertheless, at RT the transmetalation reaction is not complete and only a part of the porphyrins exchange their metal center, even in the presence of excess Co. This is contrary to the metalation of free-base porphyrins, which can be routinely employed to achieve complete synthesis of MPs with close to 100% yield.<sup>[153,172,173]</sup> Consequently, mixed MP layers and mixed valent metal centers present on the surface complicate quantitative analysis. The data remains unclear about a conclusive trend of requirements for the exchange reactions hindering a precise prediction of a possible exchange. The contrary results of UHV and liquid environment prove that the underlying process are complex and not necessarily comparable.

The presented results are relevant for the fabrication of well-defined molecular structures on surfaces. Since the metal center is defining the chemical and physical properties of the monolayer, uncontrolled transmetalation contradicts the request of a tailored synthesis of porphyrin structures with desired properties. After metal deposition the surface consists of an undefined and multi-component layer inhibiting reasonable interpretation of experimental data. Although XAS is a suitable technique to study the exchange, a quantitative analysis is barely possible as always at least two states of metal centers contribute to the spectra. Thus, the presented data lacks strong quantitative conclusions. Further studies are needed to extend the results.

Generally temperature has a large impact on both products and reaction pathways. Furthermore, different temperatures for co-deposition might influence the amount of exchanged metal centers pointing to controlled transmetalation processes. Moreover, the activation barrier could be investigated by varying the temperature during the deposition.

Additionally, the surface has a major effect on the electronic properties of the MPs and presumably is highly involved in the transmetalation process. Hence, studying different surfaces might give more information about its participation in transmetalation. Furthermore, the surface has a large impact on the stability of the MPs influencing strongly the probability of an exchange reaction. The metal center itself is crucial for transmetalation. In order to understand the principles of the exchange depending on the cation, experiments need to be extended to more metals than Fe, Co and Cu presented in this thesis. In the context of applications a controllable and reproducible synthesis pathway is required.

Nonetheless, this is the first study presenting a transmetalation in UHV using actively deposited metal on Au(111). Once, the mechanism and controlling factors are well established transmetalation offers a new route towards complex multimetallic porphyrin nanostructures.



## 4 Integrity of a Bifunctional Porphyrin Electrocatalyst

First row TMs within a N containing organic matrix have been shown to be promising earth-abundant electrocatalysts for the oxygen half-cell reaction.<sup>[34–43,51]</sup> MPs for designing molecular catalysts is inspired by nature as they represent the active site of various enzymes.<sup>[138]</sup> Active centers of enzymes consist of both monometallic and homo- or heterobimetallic complexes involving mainly Fe, Ni, Cu and Mn centers.<sup>[106]</sup> A bimetallic approach enables an additional parameter for tailoring catalytic performance demonstrating different or even novel electronic and catalytic properties in respect to the corresponding monometallic counterparts.<sup>[125]</sup> Indeed artificial MPs were applied quite successfully as catalysts.<sup>[37,40,42,174–180]</sup>

MPs find applications as homo-<sup>[35–40]</sup> and heterogeneous<sup>[41–43]</sup> electrocatalysts. Homogeneous catalysts provide an easy access to product and intermediate characterization by spectroscopy. However, homogeneous electrocatalysts are only electroactive when being nearby or in contact with the surface resulting in hindered electron transfer. Moreover, the electrolyte is restricted to media dissolving both reactant and catalyst.<sup>[175]</sup> By using heterogeneous electrocatalysts, the electrolyte is independent of the catalyst's solubility. In addition, the electron transfer is simplified due to the direct connection of the catalyst and the conducting electrode. The structure and chemical environment is more controlled leading to higher reactivity. Therefore, heterogeneous catalysts are preferred for industrial applications. Heterogeneous molecular catalysts can be created by following the concept of MOCNs. Furthermore, the 2D network with embedded undercoordinated single metal atoms enable the structural investigation on the molecular scale for fundamental insights.

Besides the reactivity of an electrocatalyst also the stability is of great importance determining the catalyst's life time. Due to the surface dependence of electrocatalysis, small changes on the molecular level are sufficient to change the performance dramatically. The structural integrity is marginal covered, while electrocatalytic stability is always discussed when reporting about electrocatalysts. The combined STM-XS approach allows studying structural and chemical stability and might indicate of active sites.

---

\*This chapter is based on publication [3] of my publication list (see CV).

This chapter addresses the structural integrity of FeTPyP+Co utilized as bifunctional catalyst for the oxygen half-cell reaction in alkaline medium. The catalyst is analyzed by complementary STM and XAS measurements depicting the behavior in diverse environments of both the transfer system and the applied EC potential.

### 4.1 Structural Stability Over Multiple Cycles of Oxygen Reduction Reaction

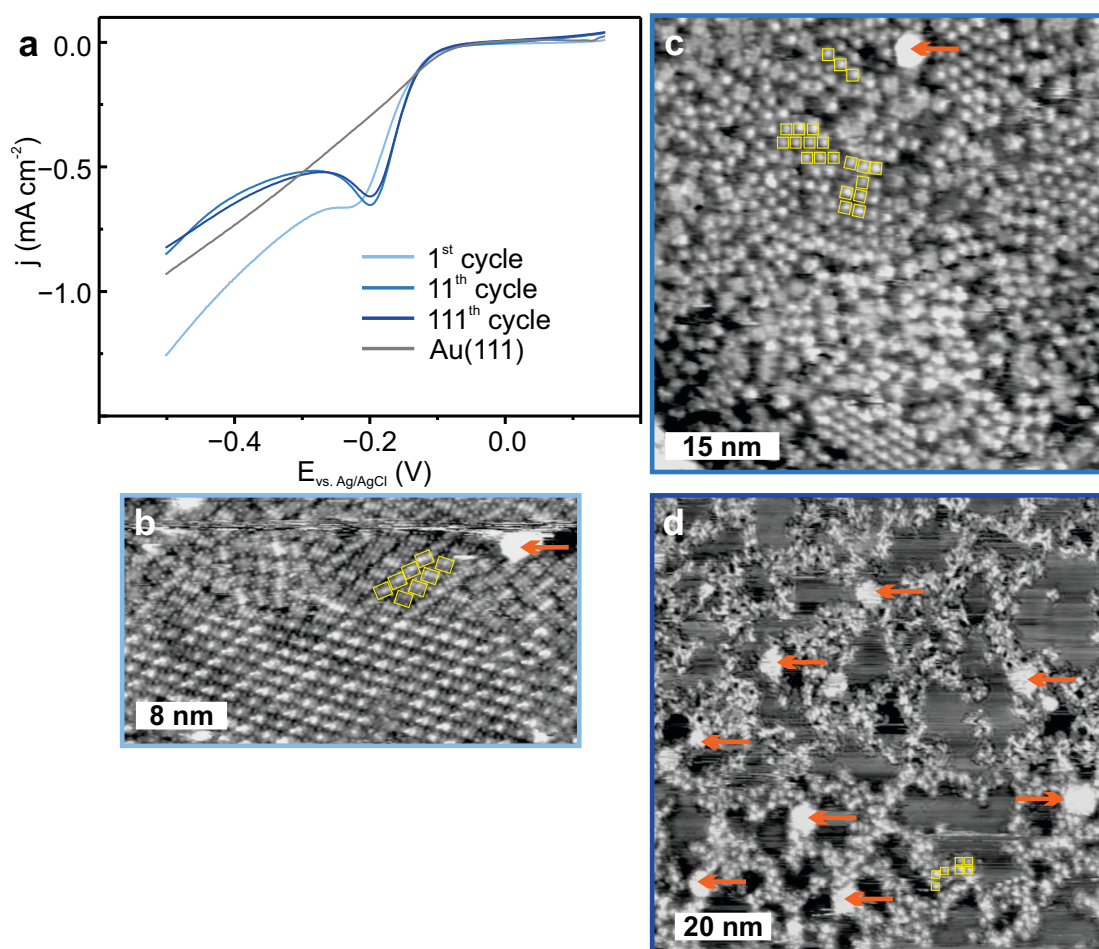
Although ORR and OER are just opposite reaction directions of the same redox couple, they proceed at potentials far apart from each other.  $O_2$  evolves at considerably more positive potentials (OER) than the back reaction consuming oxygen (ORR). Thus, the influence of the potential range on the catalyst is expected to differ for ORR and OER. As a consequence, the stability of the catalyst will be explored separately for both reactions.

Polarization curves of ORR are presented in Fig. 4.1 a. The on-set potential is determined at a current density of  $j = -0.1 \text{ mA cm}^{-2}$ . The on-set potential of  $-0.12 \text{ V}$  and the peak potential at  $-0.21 \text{ V}$  are similar for all repeated LSVs demonstrating a stable electrocatalytic performance for up to 111 cycles. At the peak potential, the current density of the 1<sup>st</sup> and the 11<sup>th</sup> cycle are comparable whereas it is reduced by 6 % for the 111<sup>th</sup>. The very first cycle differs from the others by a divergent potential jump from the open circuit potential (OCP) at  $-0.04 \text{ V}$  to the start potential of the first scan ( $0.1 \text{ V}$ ). All the following scans occur without this potential jumps during a smooth sweep of the potential, resulting in similar response of the system. The catalytic effectiveness of FeTPyP+Co is demonstrated by the enhanced current density with respect to the bare Au(111) substrate originating from an increased reduction of  $O_2$ . However, the on-set potential is similar for both systems referring to an equivalent activation overpotential.

The structural integrity of the sample was identified by STM after the 1<sup>st</sup>, 11<sup>th</sup> and 111<sup>th</sup> LSV, respectively. The molecules endure both the electrolyte (0.1 M NaOH,  $O_2$  sat.) as well as the potential window of  $0.1 \text{ V}$  to  $-0.5 \text{ V}$  (Fig. 4.1 b). Individual molecules are marked by yellow rectangles. However, the dense packed and ordered structure of the freshly prepared FeTPyP+Co network (Fig. 2.7 a) is interrupted. A small number of molecules is still grouped in islands which are distorted against each other forming grain boundaries. Moreover, cluster of roughly  $2 \text{ nm}$  in lateral extension (orange arrows) are present. Although the molecular packing is reduced, large empty areas of Au(111) are not apparent.

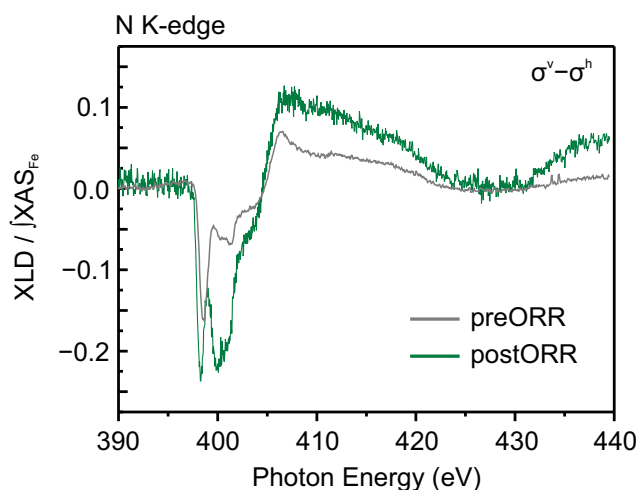
Ten more LSVs resulted in a similar structure (Fig. 4.1 c). Molecules are still intact and adsorbed on the surface. After the very first LSV, the crystallinity of the monolayer is disrupted. The STM image after 11 LSVs is similar concerning the molecules but the number of cluster and their size have grown significantly implying dynamic changes of the topography. Cluster demonstrated a lateral size of approximately  $(6 \pm 2) \text{ nm}$ .

#### 4.1. Structural Stability Over Multiple Cycles of Oxygen Reduction Reaction



**Figure 4.1:** Topographic integrity of FeTPyP+Co depending on the number of ORR cycles. (a) LSV of FeTPyP+Co for 1<sup>st</sup> LSV (light blue), 11<sup>th</sup> LSV (blue) and 111<sup>th</sup> LSV (dark blue) of ORR (0.1 V to −0.5 V, 50 mV s<sup>−1</sup>, 0.1 M NaOH, O<sub>2</sub> sat.); STM images after different number of cycles (individual molecules are identified exemplarily by yellow boxes and clusters by orange arrows): (b) 1<sup>st</sup> LSV ( $I_{\text{tunnel}} = 0.4$  nA;  $U_{\text{bias}} = 0.9$  V); (c) 11<sup>th</sup> LSV ( $I_{\text{tunnel}} = 0.3$  nA;  $U_{\text{bias}} = 1.2$  V); (d) 111<sup>th</sup> LSV ( $I_{\text{tunnel}} = 0.4$  nA;  $U_{\text{bias}} = 1.3$  V).

For a long term measurement, ORR was repeated for additional 100 LSVs resulting in a dramatic change of the morphology (Fig. 4.1 d). The cluster size remained stable while the number increased by roughly 30 %. Moreover, molecules apparently started to decompose which is evident in the upper part of Fig. 4.1 d. In the image, molecules are indistinguishable and the overall structure is not recognizable anymore. In contrast, the lower part of the image seems to resolve disordered but intact molecules (Fig. 4.1 d, yellow boxes). The few ordered patches could be interpreted as fairly ordered islands of agglomerated molecules which remind of the self-assembled molecular network. The sharp boarder between the features which could be attributed to a decomposed organic backbone and the square appearance which is attributed to intact molecules could be explained by a tip effect. However, empty areas are observed implying a reduced amount of adsorbed molecules or mobile molecules on the surface pointing to a decomposition of the molecular network.



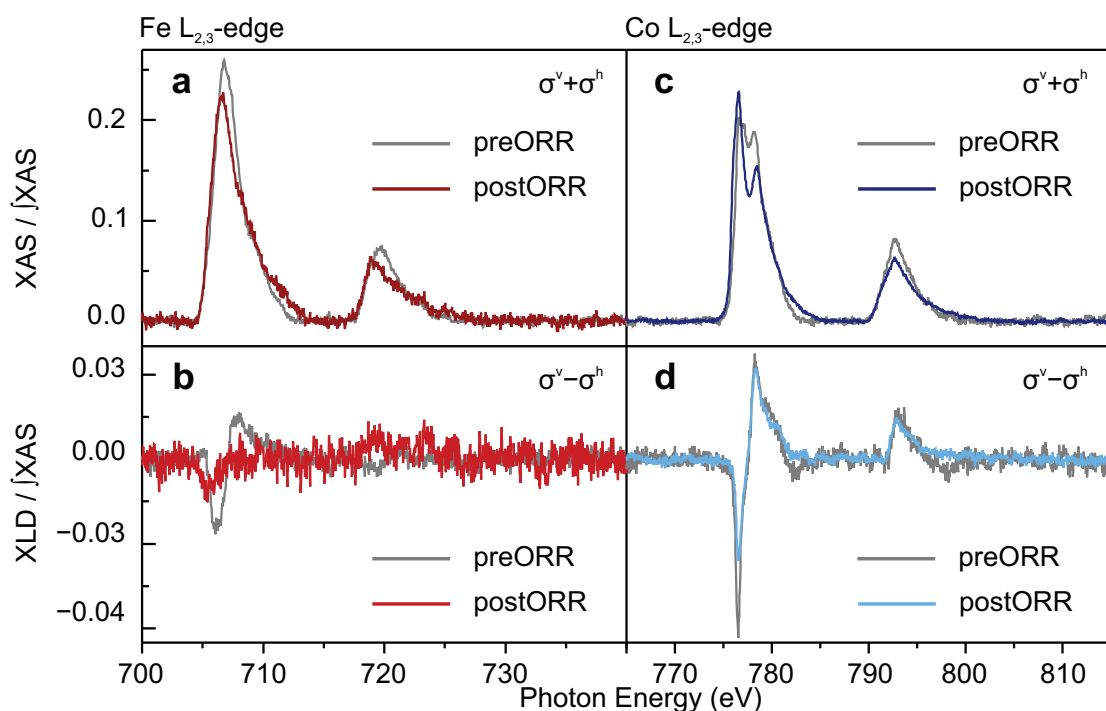
**Figure 4.2:** N K-edge, normalized to XAS of corresponding Fe  $L_{2,3}$ -edge: XLD ( $\sigma^v - \sigma^h$ ) of FeTPyP+Co after 10 LSVs (0.1 V to  $-0.5$  V,  $50 \text{ mV s}^{-1}$ ,  $0.1 \text{ M NaOH}$ ,  $\text{O}_2$  sat.). Color code: FeTPyP+Co preORR (grey), postORR (green).

The integrity of the molecular network after 10 cycles (in the following referred to postORR) is consistently supported by XAS. The N K-edge (Fig. 4.2) confirms intact and planarly adsorbed molecules. The peak positions are reminiscent of preEC (section 3.3). However, intensity ratio and overall shape differ which might be due to the changed order of the network as the dichroism is highly sensitive to the molecule's orientation on the surface.

Furthermore, the Fe  $L_{2,3}$ -edge (Fig. 4.3 a) located at  $706.6 \text{ eV}$  and  $707.7 \text{ eV}$  matches preEC in both shape and peak positions. The metallic shape of the XAS at Fe  $L_{2,3}$ -edge is explained by the on-surface transmetalation process of Fe by Co which occurs during sample preparation (see Chap. 3 for detailed explanation). The previous small but discernible XLD (Fig. 4.3 b) might be below the detection limit in this case explaining the absence of a signal. This seems plausible as XLD of preEC was already not pronounced.

Along with preEC, the Co  $L_{2,3}$ -edge (Fig. 4.3 c) illustrates a double peak at  $L_3$ -edge resulting from the coordinated character of Co. The main peak is located at  $776.6 \text{ eV}$ , the second peak lies at  $778.5 \text{ eV}$ . In difference to preEC, the ratio between the individual maxima of the double peak differs. An explanation could be an increased amount of excess Co ( $\text{Co/Fe} \approx 4.1$ ) which cannot be incorporated into the molecular network. As a result more metallic Co cluster are on the surface causing a higher intense signal at lower energies. Thus, the first peak of the double peak has a higher intensity. XLD is equivalent for both preEC and postORR (Fig. 4.3 d) demonstrating the electronic anisotropy due to the ligand field Co is exposed to.

In accordance with the cation exchange (see Chap. 3 for details), the Fe  $L_{2,3}$ -edge represents metallic properties<sup>[162,163]</sup> while the Co  $L_{2,3}$ -edge demonstrates coordinated characteristics<sup>[164]</sup>. The similarities of preEC and postORR in XAS confirm the chemical stability of the molecular catalyst for at least 10 LSVs. Moreover, clearly no reactants are adsorbed



**Figure 4.3:** XAS at Fe and Co  $L_{2,3}$ -edges of FeTPyP+Co after 10 LSVs driving the ORR (0.1 V to  $-0.5$  V,  $50 \text{ mV s}^{-1}$ ,  $0.1 \text{ M NaOH}$ ,  $\text{O}_2$  sat.). Fe  $L_{2,3}$ -edge: (a) XAS ( $\sigma^v + \sigma^h$ ) and (b) XLD ( $\sigma^v - \sigma^h$ ); Co  $L_{2,3}$ -edge: (c) XAS and (d) XLD.  $L_{2,3}$ -edges are normalized to the corresponding integral of XAS

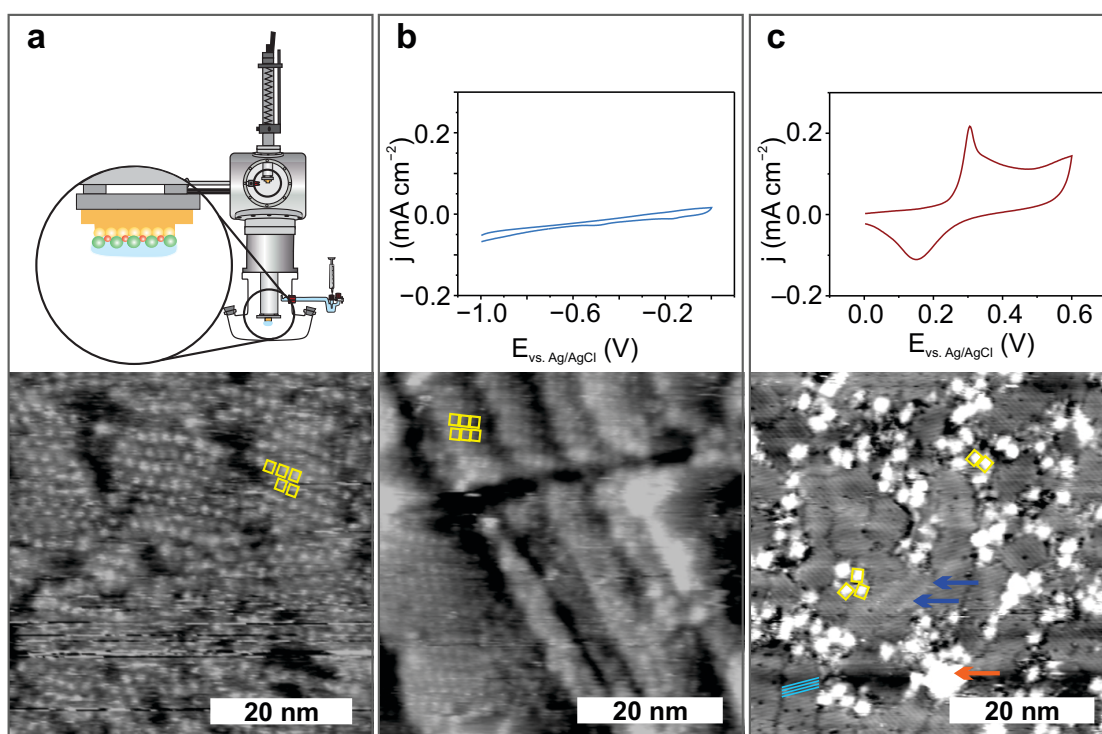
on the network which would be expressed by a strongly changed shape and shifted energy positions in the spectrum caused by an altered electronic structure.<sup>[56,181]</sup> The unchanged electronic structure after ORR displays FeTPyP+Co as catalyst which is unaltered subsequent to the reaction as expected. The global approach of XAS is substantiated by the local molecular integrity demonstrated by STM.

The reduced crystallinity of the network could be explained by dissolution of molecules in the electrolyte. In contrast, the decomposition of residual adsorbed molecules on the surface might be an effect of the applied potential or aggressive well-known intermediates such as  $\text{OOH}_{\text{ads}}$  cleaving the porphyrins. However, for at least 10 cycles the actual catalyst is assigned to the molecular network in its slightly disordered structure. The structural decomposition of the network starts before 111 LSVs confirmed by STM.

## 4.2 Potential Induced Morphological and Chemical Transformation

The FeTPyP+Co catalyst faces diverse reaction conditions when catalyzing the OER, although the electrolyte is identical. The electrochemical stability of OER was demonstrated for at least 15 CVs.<sup>[103]</sup> However, on the molecular scale a major structural change occurs already during the very first CV.<sup>[103]</sup> The origin of the morphological change has not been addressed yet.

The multi-step experiment and the large potential window of  $-1.2$  V to  $0.75$  V bedevil the elucidation of the surface transformation. Therefore, the experiment is subdivided into parts and subsequently investigated by STM. At first, the sample was exclusively exposed to the electrolyte. Thereafter, the potential window was limited to the negative range and then to the positive potential window eventually catalyzing the OER.



**Figure 4.4:** Potential induced structural change of FeTPyP+Co. (a) Exposure of FeTPyP+Co to the  $0.1$  M NaOH electrolyte, Ar sat. for  $5$  min in depicted hanging meniscus configuration and STM image of the post electrolyte network ( $I_{\text{tunnel}} = 0.3$  nA;  $U_{\text{bias}} = 830$  mV); (b) CV ( $-1.0$  V to  $0.0$  V,  $50$  mV  $\text{s}^{-1}$ ,  $0.1$  M NaOH, Ar sat.) and postEC STM image ( $I_{\text{tunnel}} = 0.3$  nA;  $U_{\text{bias}} = 830$  mV); (c) CV ( $0.0$  V to  $0.75$  V,  $50$  mV  $\text{s}^{-1}$ ,  $0.1$  M NaOH, Ar sat.) and postEC STM image<sup>[103]</sup> ( $I_{\text{tunnel}} = 0.2$  nA;  $U_{\text{bias}} = 787$  mV). Color code: single molecule (yellow boxes), cluster (orange arrow), Au(111) reconstruction (blue arrows), ordered lines (cyan lines).

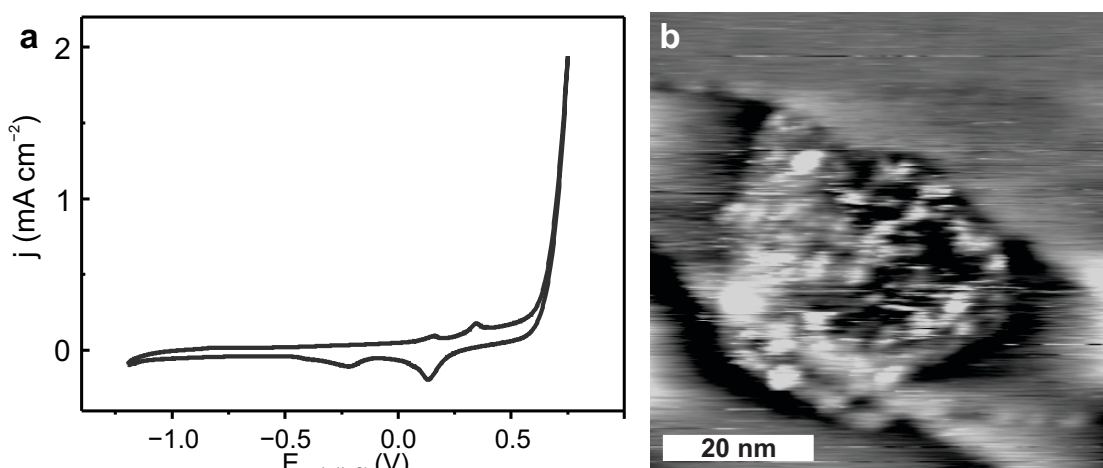
Exposing FeTPyP+Co to  $0.1$  M NaOH, Ar sat. solution results in destructed crystallinity of the network (Fig. 4.4 a). The STM image depicts the integrity of the molecules which are agglomerated in small ordered islands distorted against each other. The stability of the network towards the electrolyte is expected from section 4.1. In contrast to the postORR data, cluster are not visible.

Subsequently, a CV with a negative potential window was applied (Fig. 4.4 b). The current density is low and no redox activity is measured. The negative potential window represents the double layer region of Au(111) implying that Au is not undergoing any redox reaction. The *ex situ* STM image illustrates a comparable topography as after electrolyte exposure. Molecules

## 4.2. Potential Induced Morphological and Chemical Transformation

are still distinguishable and ordered in small islands but lacking the long range order typical for the pristine FeTPyP+Co network (Fig. 3.10 b, c).

Contrary, applying positive potential eventually leads to decomposition of the molecules (Fig. 4.4 c). The CV demonstrates three pronounced redox processes which are assigned to Au oxidation at 0.31 V and reduction at 0.15 V, respectively as well as the on-set potential of OER at 0.60 V. The surface is reminiscent of FeTPyP+Co utilized for one OER cycle (Fig. 2.7 c). Some features of the STM image could be interpreted as residual intact molecules (yellow boxes). However, this is highly speculative. The topography illustrates mainly cluster (orange arrow), some ordered lines (cyan lines) and the Au(111) reconstruction (blue arrow). The origin of the cluster is supposedly a chemical or structural change of the molecular network resulting in cluster agglomeration of residual components. However, the origin of the ordered lines is unclear. Nonetheless, the presence of the Au(111) reconstruction demonstrates the overall cleanliness of the experimental procedure because the surface reconstruction is highly sensitive to impurities.

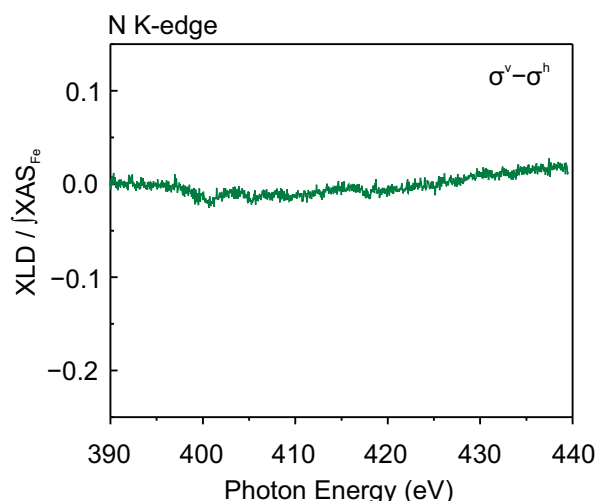


**Figure 4.5:** OER of FeTPyP+Co and STM image postOER. (a) Typical CV of FeTPyP+Co for OER (−1.2 V to 0.75 V, 50 mV s<sup>−1</sup>, 0.1 M NaOH, Ar sat.); (b) postOER STM, ( $I_{\text{tunnel}} = 0.23 \text{ nA}$ ;  $U_{\text{bias}} = 1.3 \text{ V}$ ).

STM is inconclusive about the chemical environment accompanied by the structural transformation which will therefore be addressed by XAS. Generally, EC stability of the electrocatalyst is determined by running at least 10 CVs. Although the structural change occurs already during the very first CV, for reasons of consistency XAS was performed after 10 CVs of OER. The CV illustrates several redox processes (Fig. 4.5 a): in the anodic scan the adsorption of Cl<sup>−</sup> ions at 0.16 V resulting from the reference electrode, Au oxidation at 0.35 V and the OER on-set at 0.60 V.<sup>[103]</sup> The cathodic scan depicts Au reduction at 0.13 V and the ORR at −0.22 V matching the peak potential reported in section 4.1.<sup>[103]</sup> The STM topography after 10 CVs (in the following referred to postOER) varies strongly from the picture described after exclusively applying 1 CV or the positive potential range (Fig. 2.7 c, Fig. 4.4 c respectively). The surface is barely covered but occasionally shows cluster of approximately 40 nm in diameter mainly located at

step edges. The surface of the cluster appears highly inhomogeneous with structured features in the islands but no molecules are observed.

A change in orientation of the molecular network is confirmed by the absence of a XLD signal at the N K-edge (Fig. 4.6) but lacks information on the integrity of the organic backbone. The absence of a XLD only expresses isotropy of N which could be caused by a disordered structure as well as by decomposition of the organic molecule. The XAS at N K-edge would give more information about the presence of organic N. However, the measured XAS is difficult to interpret due to x-ray beam contamination of organic N components interfering in this specific energy range. Nonetheless, the XLD signal demonstrates real effects of the sample as permanent contamination of the x-ray beam will cancel out in good approximation by subtracting the two polarization directions. Previously reported XPS for this system reported residual organic N postOER<sup>[103]</sup> (Fig. 2.9), thus the presence of N bound in an organic matrix seems plausible. The absent XLD signal could be attributed to organic fragments distributed randomly within the large clusters presented in STM explaining the isotropy.



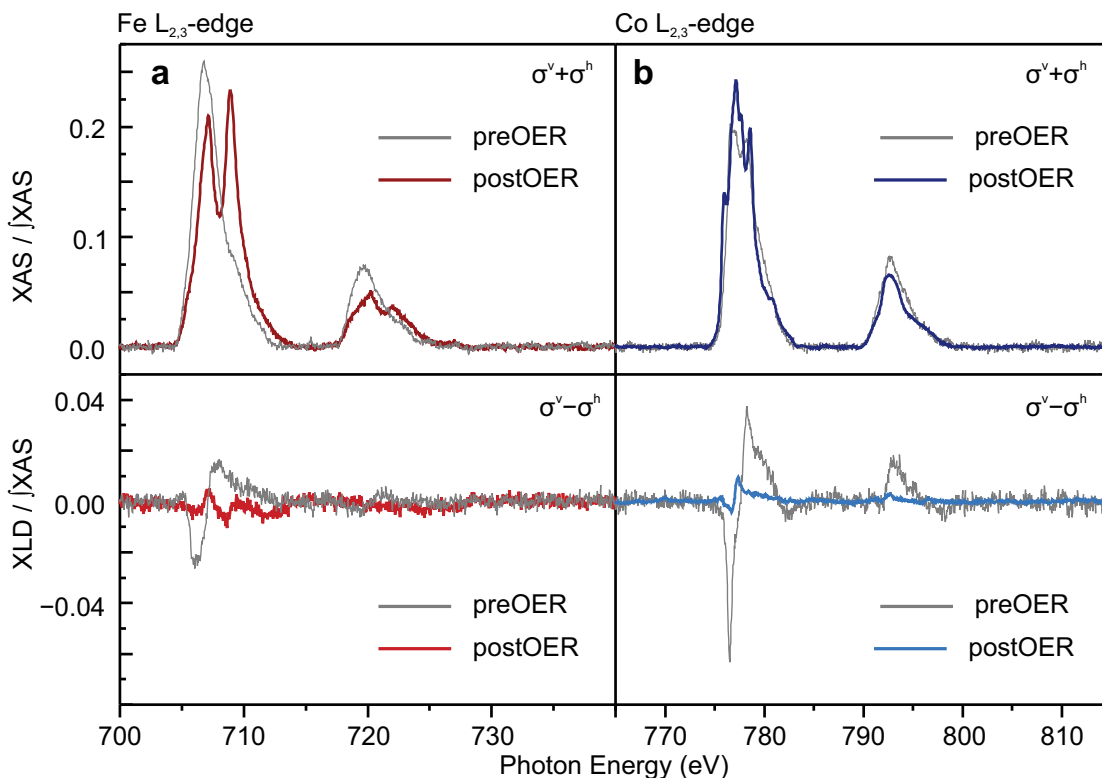
**Figure 4.6:** XLD ( $\sigma^v - \sigma^h$ ) of FeTPyP+Co postOER at N K-edge, normalized to XAS of corresponding Fe L<sub>2,3</sub>-edge. PostOER: 10 cycles, -1.2 V to 0.75 V, 50 mV s<sup>-1</sup>, 0.1 M NaOH, Ar sat.

In contrast to preEC and postORR, the Fe L<sub>2,3</sub>-edge (Fig. 4.7 a) demonstrates a multiplet structure. Fe L<sub>3</sub>-edge consists of two peaks almost equal in intensity at 707.1 eV and 708.9 eV. The multiplet structure is reproduced in the L<sub>2</sub>-edge at 720.2 eV and 722.0 eV. This double peak is typically reported for Fe oxide.<sup>[182–184]</sup> The Fe XLD is roughly zero indicating the absence of an anisotropy which would be expected for metal cluster.

The molecular network of CoTPyP, FeTPP+Co and FeTPyP+Co showed a double peak at the Co L<sub>2,3</sub>-edge. However, the postOER Co L<sub>3</sub>-edge consists of a three fold multiplet structure which is generally assigned to Co oxide.<sup>[165]</sup> The three peaks can be identified at 776.0 eV, 777.2 eV and 778.6 eV (Fig. 4.7 b). A small XLD signal can be confirmed. The minimum lies at the same position as pristine FeTPyP+Co but the maximum is shifted by about 1 eV to lower energies.

## 4.2. Potential Induced Morphological and Chemical Transformation

Due to the diverse energetic position and shape of XLD, the anisotropy results more likely from a small amount of coincidentally ordered oxide structures than from residual coordinated Co.



**Figure 4.7:** XAS ( $\sigma^v + \sigma^h$ ) and XLD ( $\sigma^v - \sigma^h$ ) of FeTPyP+Co preOER (grey) and postOER (colored) at (a) Fe  $L_{2,3}$ -edge and (b) Co  $L_{2,3}$ -edge.  $L_{2,3}$ -edges are normalized to the corresponding integral of XAS. PostOER: 10 cycles,  $-1.2$  V to  $0.75$  V,  $50 \text{ mV s}^{-1}$ ,  $0.1 \text{ M NaOH}$ , Ar sat.

Consequently, the chemical composition of the large cluster depicted by STM can be identified as Fe/Co oxide by XAS with  $\text{Co/Fe} \approx 2.3$ . It is unclear whether the cluster are a mixed oxide of both metals, but it seems plausible because of the small number and the size. Additional evidence comes from STM image of Co oxide cluster on Au(111)<sup>[185,186]</sup> which resemble those of the postOER FeTPyP+Co images (Fig. 4.5 b). The TPyP molecules possibly decompose due to oxidative cleavage during OER and organic fragments leach into the electrolyte or alternatively are involved in the large cluster but are not lying flat with the original organic backbone on the surface. The metal centers remain on the surface and sinter into oxide cluster, which are catalytically active. This cleavage could be induced by the oxidation of the gold substrate taking place at  $0.34$  V. This broad peak in the CV might also superimpose the electrochemical signal that should appear due the oxidation process of the MOCN. The degradation of the MOCN is consistently demonstrated by both STM and XAS. For FeTPyP+Co a stable OER is measured<sup>[103]</sup> leading to the conclusion of a morphological and chemical change from the bimetallic-organic network into oxides before actually driving the OER.

Co and Fe oxides are well-known for their effective catalytic properties towards ORR and OER.<sup>[9,187]</sup> Previously reported XPS (Fig. 2.9) indicated a +2 oxidation state of the metal center in the FeTPyP+Co network which is preserved postEC.<sup>[103]</sup> Also the XAS data seem to support the +2 oxidation state as in the oxide form a +2 or higher oxidation state is most likely. The N K-edge demonstrates the structural change due to the missing XLD signal, but lacks further information about the stability of the organic backbone. However, XPS confirms an intact organic backbone in the N 1s signal after only one cycle of OER.<sup>[103]</sup> The isotropy of possibly remaining N could be attributed to molecules enveloped in the oxide cluster resulting in a disordered structure.

### 4.3 Conclusion

The structural stability of porphyrin molecules with embedded metal centers differs between ORR and OER although both reactions are formally just the opposite direction of the same redox couple. XAS and STM confirm the stability of FeTPyP+Co for ORR for at least 10 LSVs. Note that already after 1 LSV the amount of molecules is reduced and clusters are formed. STM images show molecules remaining adsorbed on the Au(111) surface under reaction conditions, but reassemble into non-crystalline monolayers. Only a few small domains retain the square structure typical for preEC FeTPyP+Co. XLD at the N K-edge confirms the intact organic backbone of the molecules and the planar adsorption on the surface. According to STM the network varies between 11 to 111 LSVs. Nevertheless, molecular islands can still be identified. It can be concluded that the molecular network itself serves as electrocatalyst for ORR.

OER is more aggressive and decomposes the network quickly. The MP network serves as precursor for the potential-induced transformation from the MOCN to Co/Fe oxide which is the active catalyst. The transformation occurs right before the very first on-set of OER explaining the high electrochemical stability.<sup>[103]</sup> Once the oxide is formed, it remains stable in chemical composition as well as electrocatalytic activity. Considering the results presented in section 2.4<sup>[103]</sup> the catalytic activity of the oxide is highly dependent on the order of deposition FeTPyP+Co or CoTPyP+Fe which might be also influenced by the phenomenon of on-surface transmetalation (Chap. 3) occurring for FeTPyP+Co. The patches observed in STM after OER (Fig. 4.7 b) are catalytically active Co/Fe oxide islands demonstrated by the typically shaped XAS at Fe and Co L<sub>2,3</sub>-edge.

The presented results emphasize a difference between the picture of the catalyst depicted in section 2.4<sup>[103]</sup> and the real catalyst. The applied potential as well as the electrolyte have a major impact on the molecular structure and chemical composition. Thus, not only electrochemical but also chemical and structural integrity of an electrocatalyst need to be monitored. Only the combination of real-space imaging techniques at the molecular level and spectroscopic techniques sensitive at the submonolayer regime for all elements can reveal the fate of heterogeneous metallo-organic catalysts.

## 5 Chemical and Structural Integrity of a Vacuum-Prepared Co Electrocatalyst

Among TM oxides cobalt oxide is the most promising non-precious alternative for catalyzing the OER in alkaline media.<sup>[64,65,185,188–191]</sup> Cobalt offers a large range of oxidation states such as  $\text{Co}^{2+}$ ,  $\text{Co}^{3+}$  and  $\text{Co}^{4+}$  which differ strongly in their electrocatalytical properties.<sup>[65,185,189]</sup> The most investigated structure is the spinel  $\text{Co}_3\text{O}_4$  consisting of mixed valent  $\text{Co}^{2+}$  and  $\text{Co}^{3+}$ .<sup>[64,188,189]</sup> Under OER conditions the oxide structure possibly undergoes phase transition involving  $\text{Co}_2\text{O}_3$  and  $\text{CoOOH}$ .<sup>[65]</sup>  $\text{Co}^{3+}$ , present in the  $\text{CoOOH}$  phase, is assumed to be the reactive oxidation state acting as both reduction and oxidation agent.<sup>[191,192]</sup> However, underlying mechanisms are currently not well-understood. The role of  $\text{Co}^{4+}$ , for instance, is still under debate. The existence of  $\text{Co}^{4+}$  already in the as-prepared catalytic material supposedly delays the evolution of oxygen.<sup>[191]</sup> But also,  $\text{Co}^{4+}$  possibly acts as intermediate oxidation state involved in a productive OER.<sup>[193]</sup> It is clear that the oxidation state is an important parameter which needs to be considered for electrocatalyst design. However, the precise role in the complex reaction pathways is not well-understood, yet. In addition, the morphology of Co oxide has a high impact on the catalytic performance due to its surface dependence.<sup>[185]</sup> This lack of knowledge prohibits the development of suitable earth-abundant and low-cost catalysts for electrolyzers.

Investigating model systems on the atomic scale enables a route for a fundamental understanding of the working mechanism of the catalyst. Well-defined Co oxide structures prepared in UHV, for instance, serve as suitable model system to study the catalytic processes occurring at the oxide material. UHV prepared Co oxide islands have been studied by STM. By dosing water gas to the islands, the water splitting reaction was simulated.<sup>[186,194]</sup> The fundamental approach of gas experiments in vacuum is valid for investigating basic principles but lacks transferability to electrochemical conditions. Driving an EC reaction by an applied potential at the working electrode enables reaction pathways which are impossible to drive without the voltage, and less so in vacuum.

---

\* In collaboration with Anton Makoveev (Central European Institute of Technology, Brno, Czech Republic).

This chapter presents preliminary EC experiments on vacuum-prepared metallic Co cluster on a Au(111) substrate. In Co oxide, the oxygen determines the oxidation state of Co and therefore the electrocatalytic performance. For a distinct discrimination between the influences of the individual chemical components, Co and O, the model system is built up gradually. Following a previous strategy, the behavior of the metallic cluster in the transfer system is studied by the STM-XPS approach. Eventually, the cluster served as electrocatalyst for OER and is compared to electrochemically fabricated oxide structures based on the porphyrin MOCN precursor (see Chap. 4).

### 5.1 Behavior of the Co Cluster in the Transfer Procedure

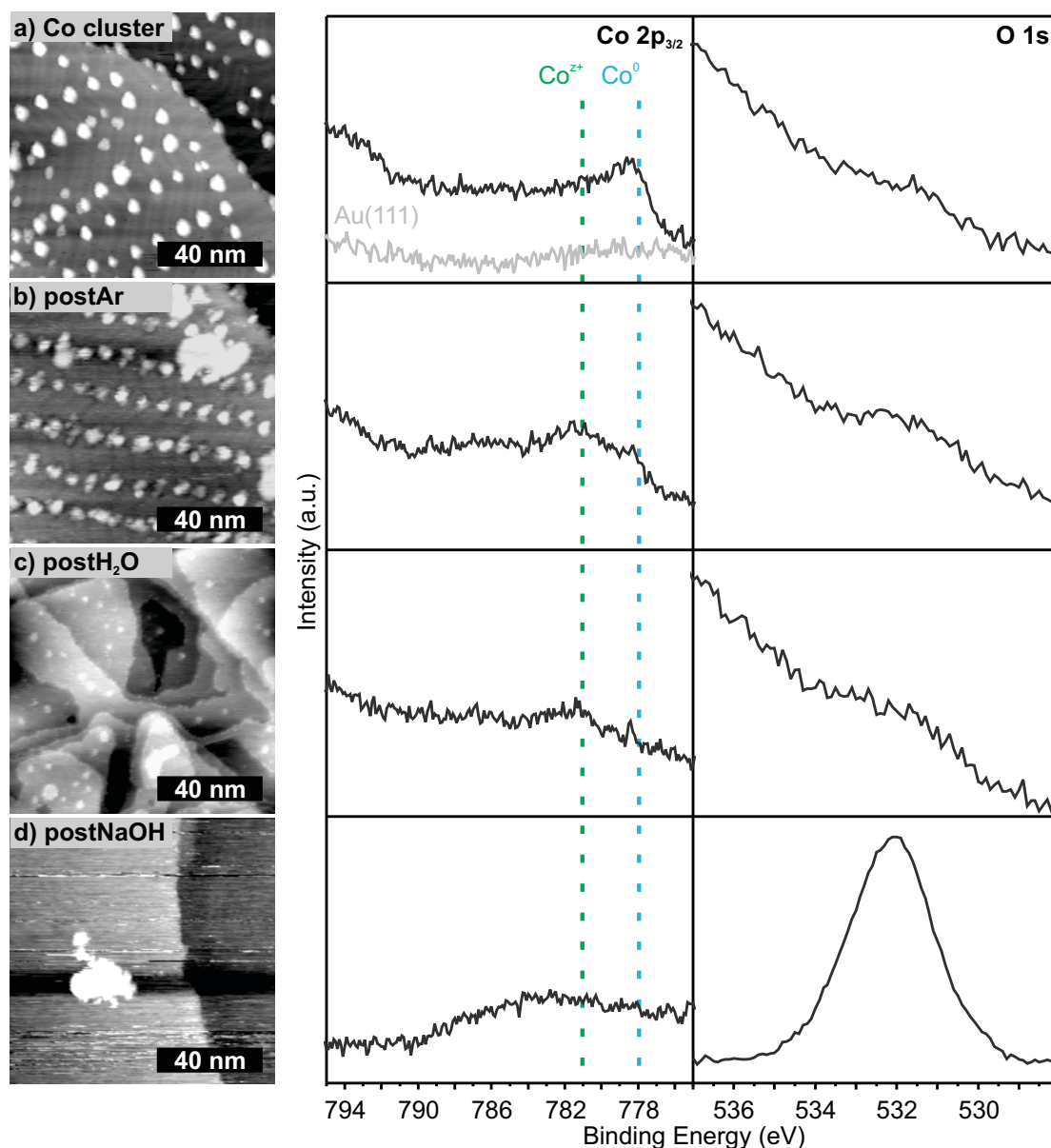
The electrocatalyst is prepared by sublimation of metallic Co onto Au(111), which forms cluster with a lateral extension of 4-8 nm on the surface (Fig. 5.1 a). The Au(111) substrate acts as template as the Co cluster are nicely arranged at the elbow sites and step edges. Chemical analysis is achieved by XPS. The background subtracting at the Co 2p<sub>3/2</sub> signal is complex and inhibits quantitative analysis. Nevertheless, shape and estimated BE give qualitative information. The Co 2p<sub>3/2</sub> spectrum demonstrates the metallic characteristic of Co at about 778 eV which agrees well with literature.<sup>[195,196]</sup> The broad tail at high BE of the signal might originate from multiplet structure of Co<sup>0</sup><sup>[197]</sup> or small amounts of oxidized Co<sup>[195,198]</sup>. However, the latter is unlikely due to the absent O 1s signal.

Exposure of the Co cluster to 1 bar of Ar (5.0) (postAr) for 5 min leaves the surface structure seemingly unchanged (Fig. 5.1 b). Thus, a difference between as-prepared and postAr Co cluster is not evident by STM. Contrary, XPS confirms a transformation in the chemical environment emphasizing again the importance of combining imaging and spectroscopic techniques. Upon Ar gas exposure (5 min), the Co 2p<sub>3/2</sub> signal strongly broadened and additional contributions appear at high BEs. The shoulder at approximately 778 eV illustrates residual metallic Co. The most intense contribution has a BE of about 781 eV attributed to oxidized Co.<sup>[195,198]</sup> The O 1s core level depicts a broad peak of low intensity disallowing a detailed interpretation. Nonetheless, the O 1s signal confirms the presence of oxygen e.g. as O, OH<sup>-</sup> or OOH<sup>-</sup> groups presumably oxidizing Co.<sup>[199]</sup> The source might be residual water or molecular oxygen contamination during Ar exposure.<sup>[199]</sup>

Upon a 5 min water contact (postH<sub>2</sub>O), Co islands illustrate a lower degree of organization demonstrating an initial sintering (Fig. 5.1 c). In addition, the intensity of the Co 2p<sub>3/2</sub> signal decreased with respect to freshly prepared Co cluster, inferring a partial loss of Co from the surface. Water molecules might interact with Co forming a semi-solvated water-Co species which could be mobile at the solid-liquid interface.<sup>[186]</sup> Based on the interaction with the water molecules, a part of the atoms could be eventually surrounded by a complete solvation shell leaving the surface which could explain the loss of Co amount. The Co 2p<sub>3/2</sub> core level suggests still a small amount of metallic Co visible by the tail around 778 eV but most Co seems

## 5.1. Behavior of the Co Cluster in the Transfer Procedure

to be oxidized. The O 1s core level is reminiscent of postAr. The signal could be explained by oxide, OH<sup>-</sup> or OOH<sup>-</sup> species resulting from water exposure.<sup>[199]</sup>



**Figure 5.1:** Cobalt cluster exposed to different environments of the transfer procedure each for 5 min. For each step an exemplary STM image as well as the Co 2p<sub>3/2</sub> and O 1s core levels are shown, BE of metallic Co (blue) and oxidized Co (green) are indicated by dashed lines: (a) Co cluster ( $I_{\text{tunnel}} = 0.3 \text{ nA}$ ;  $U_{\text{bias}} = 1.0 \text{ V}$ ); (b) postAr ( $I_{\text{tunnel}} = 0.3 \text{ nA}$ ;  $U_{\text{bias}} = -1.0 \text{ V}$ ); (c) postH<sub>2</sub>O ( $I_{\text{tunnel}} = 0.3 \text{ nA}$ ;  $U_{\text{bias}} = -1.2 \text{ V}$ ); (d) postNaOH ( $I_{\text{tunnel}} = 0.3 \text{ nA}$ ;  $U_{\text{bias}} = -1.0 \text{ V}$ ).

Electrolyte exposure (0.1 M NaOH, postNaOH) for 5 min decreases the number of cluster dramatically. At the same time the lateral extension of the cluster increases to about 30 nm (Fig. 5.1 d). Two reasons might explain the dramatic change of the surface, one, a major

part of Co is dissolved in the alkaline electrolyte and two, Co cluster turn mobile in aqueous environment resulting in sintering of Co into large cluster. The dramatic change depicted in STM is supported by XPS. The Co 2p<sub>3/2</sub> peak is fundamentally different to the metallic signal of Co depicted in Fig. 5.1 a and the very broad signal is shifted to much higher BE. The high intense O 1s signal is explained by non-rinsing the sample after electrolyte exposure with water and cannot be further evaluated.

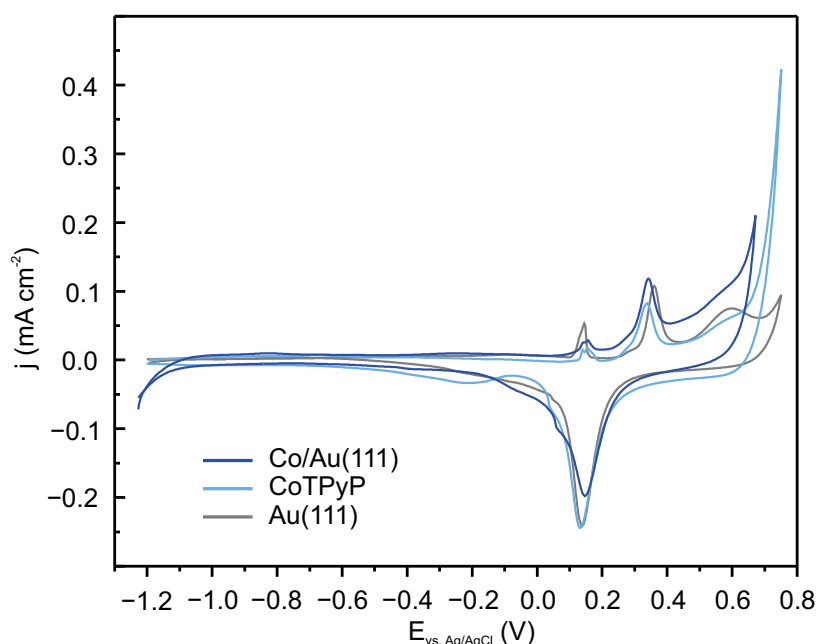
The oxidation of Co, best followed in the Co 2p<sub>3/2</sub> signal, is initiated already by Ar gas and continued by contact with aqueous solution. Applying an electrochemical potential is not necessary to trigger the oxidation process. The contact of aqueous solution goes along with dissolving and sintering of Co. The hydroxo complex of Co is insoluble in diluted NaOH but the formation of a highly soluble hexaquo complex could explain the solvation of oxidized Co from the Au(111) surface. The mobility of well-prepared Co oxide islands in UHV upon water gas exposure has been reported and might be valid also for Co cluster.<sup>[186]</sup> The described interaction of oxidized Co with water would support the hypothesis of an aquo complex. The residual Co on the surface might be hydroxylated which could explain also the pronounced O 1s peak.

## **5.2 Oxidized Co Cluster Catalyzing the Oxygen Evolution Reaction**

Co oxide is assumed to be highly stable under the harsh conditions of OER. The unconventional synthesis route starting from metallic Co oxidized upon contact with aqueous solution will be compared electrocatalytically to the oxide structures generated from CoTPyP-MOCN precursor<sup>[103]</sup>.

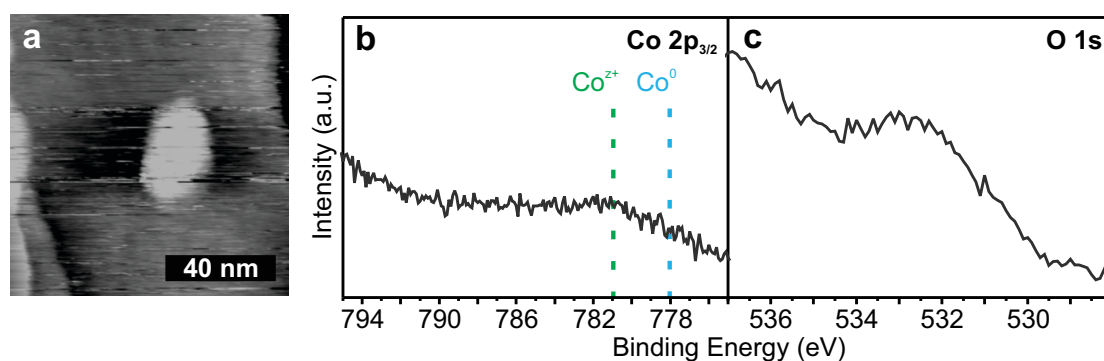
The electrolyte contact results in mainly oxidized Co islands. The representative CVs of the Co cluster, as well as reference systems, are plotted in Fig. 5.2. As explained earlier the CV contains multiple signals referring to Cl<sup>-</sup> ions from the RE and Au oxidation and reduction as well as the relevant reactions such as OER at about 0.6 V and ORR at about -0.22 V.<sup>[103]</sup>

Co cluster demonstrate an on-set potential of 0.65 V ( $j=0.15 \text{ mA cm}^{-2}$ ) for the OER which is negatively shifted by about 100 mV compared to Au(111). A current density of  $j=0.15 \text{ mA cm}^{-2}$  could not be reached at the bare Au(111) WE. As reported in Chap. 4 the application of positive potentials generates metal oxide from CoTPyP. The generated amorphous oxide structures are further referred as CoTPyP. Both Co cluster and CoTPyP consist of comparable number of Co atoms on the surface and demonstrate a slightly shifted on-set potential of about 40 mV at  $j=0.15 \text{ mA cm}^{-2}$ . However, the difference is very small and might lie within the error of comparing two different experimental sets. Thus, a significant effect on OER catalysis cannot be confirmed. The OER at the Co cluster catalyst runs stable at least for up to 10 CVs. In addition, the Co cluster presents a reduced potential window for the overall water splitting reaction visible by the diminished overpotential for both the OER and hydrogen evolution reaction (HER). Catalyzed by Co cluster, the HER starts at -1.06 mV, whereas for CoTPyP it is not observed up to -1.2 mV.



**Figure 5.2:** Cobalt cluster catalyzing OER. CV of Co cluster (dark blue) ( $-1.2$  V to  $0.70$  V,  $50$   $\text{mV s}^{-1}$ ,  $0.1$  M NaOH, Ar sat.), CoTPyP<sup>[103]</sup> (light blue) and Au(111) (grey) ( $-1.2$  V to  $0.75$  V,  $50$   $\text{mV s}^{-1}$ ,  $0.1$  M NaOH, Ar sat.).

Investigating the surface postOER results in comparable STM images as for postNaOH. Large cluster of about  $40$  nm in lateral extension are present on the surface. The decreased amount of Co is reflected in the Co  $2p_{3/2}$  spectrum. The position of the broad signal suggests completely oxidized Co on the surface in poorly defined oxidation environments. The precise oxidation state remains unclear and might not be restricted to only one state. The O  $1s$  core level shows a broad but intense signal which is probably attributed to  $\text{OH}^-$ ,  $\text{OOH}^-$  groups and oxide structures. The variation of XPS results of postNaOH and postOER could be explained by the additional oxidation process driven by the applied potential. It is well known to drive several oxidation processes including the formation of different allotropes of  $\text{CoO}_x$ .<sup>[65,189]</sup>



**Figure 5.3:** Cobalt cluster postOER ( $-1.2$  V to  $0.7$  V,  $50$   $\text{mV s}^{-1}$ ,  $0.1$  M NaOH, Ar sat., 10 CVs). (a) STM image ( $I_{\text{tunnel}} = 0.3$  nA;  $U_{\text{bias}} = 1.0$  V); XPS core levels: (b) Co  $2p_{3/2}$ ; (c) O  $1s$ . BEs of metallic Co (blue) and oxidized Co (green) are indicated by dashed lines.

CoTPyP and Co cluster present a small shift in on-set potential at  $j=0.15 \text{ mA cm}^{-2}$  demonstrating a potentially enhanced catalytic performance for the cluster. One can only speculate about possible explanations for the catalytic enhancement. In addition the reliability of the shift has to be further investigated statistically as the difference is very small between the two systems. XPS demonstrated a large amount of  $\text{OH}^-$  species involved in the oxidized Co cluster which might resemble  $\text{CoOOH}$ ,<sup>[191,192]</sup> commonly assumed to be the most reactive phase. A higher amount of highly reactive hydroxide species on the electrode surface might enhance the catalytic reaction of Co cluster. In contrast, for CoTPyP, the oxide is assumed to be the dominating chemical component (see Chap. 4) which is less reactive explaining the positively shifted on-set potential in respect to Co cluster.

### 5.3 Summary

UHV prepared Co cluster are easily oxidized by exposing to water or electrolyte. However, the oxidation state remains unclear. The oxidized Co acts as catalytic material for the complete water splitting reaction reducing both the on-set potential for OER and HER. The electrocatalyst showed a reduced activation overpotential for OER of about 100 mV compared to Au(111) and a very small improvement in respect to CoTPyP-based oxidized structures. However, the potential shift between the Co cluster and the CoTPyP is difficult to evaluate and need to be further investigated. In contrast to CoTPyP, Co cluster demonstrated a positively shifted activation overpotential for HER which was not further analyzed but opens another interesting field for these type of catalysts. The presented results can only be considered as preliminary and have to be extended.

The rather unconventional oxidation procedure causes various oxidized species which cannot be clarified by presented XPS data. As pointed out in the introduction, the oxidation state determines the electrocatalytic performance. Hence, Co cluster oxidized in the electrolyte are unsuitable to clarify these questions and more controlled systems such as vacuum prepared 2D Co oxide islands should be considered to illuminate the catalyzing sites on the atomic scale.<sup>[185,186,194]</sup> Preoxidized Co might also show increased structural stability compared to metallic Co cluster.

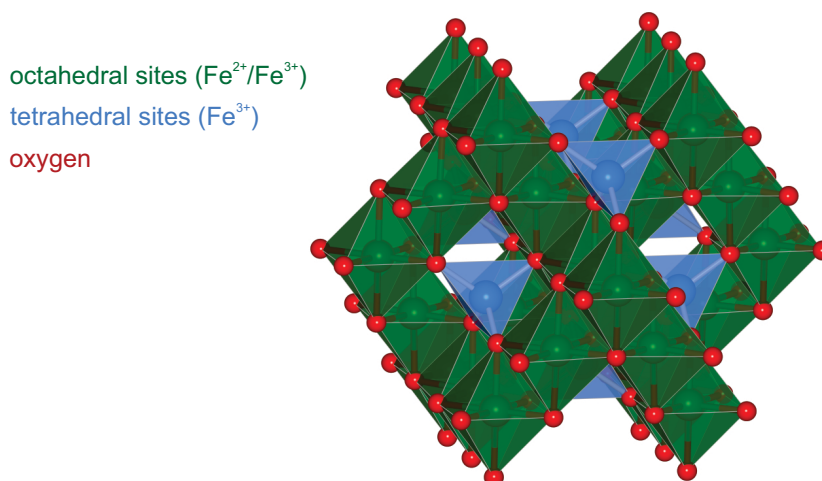
## 6 Fundamental Insights into $\text{Fe}_3\text{O}_4(001)$ Utilized as Catalyst Support

Iron oxide is one of the most common and inexpensive materials on earth.<sup>[200]</sup> It is available in manifold stoichiometry and structures resulting in a variety of oxidation states of iron which are decisive for the characteristics of the material in electrocatalysis. Although catalytic performance is comparatively lower for iron than for cobalt oxide, iron oxide is significantly cheaper and less toxic.<sup>[62]</sup>

Hematite ( $\alpha\text{-Fe}_2\text{O}_3$ ), for instance, shows promising properties for energy storage and heterogeneous catalysis.<sup>[62,201–203]</sup> Magnetite ( $\text{Fe}_3\text{O}_4$ ), on the other hand, is relatively inert and non-toxic,<sup>[204]</sup> providing a suitable substrate for catalytic material.  $\text{Fe}_3\text{O}_4$  belongs to the inverse spinel class involving two different oxidation states  $\text{Fe}^{2+}$  and  $\text{Fe}^{3+}$  (Fig. 6.1). The structure is based on a face-centered cubic (fcc)  $\text{O}^{2-}$  anion lattice (Fig. 6.1, red). 1/8 of the tetrahedral (Fig. 6.1, blue) and 1/2 of the octahedral sites (Fig. 6.1, green) are occupied. Tetrahedral sites are exclusively occupied by  $\text{Fe}^{3+}$ , whereas the octahedral sites are equally filled by  $\text{Fe}^{2+}$  and  $\text{Fe}^{3+}$ .<sup>[205–207]</sup> The diverse oxidation states on the octahedral sites are responsible for the good electronic conductivity enabled by electron hopping between the Fe cations.<sup>[208]</sup>

In heterogeneous catalysis, the substrate influences heavily the catalytic performance illustrating the importance of investigating the substrate and its effect on the catalyst.<sup>[209]</sup> Single crystal  $\text{Fe}_3\text{O}_4(001)$  offers a well-defined surface which can be prepared easily and reproducibly in UHV.<sup>[205]</sup> The surface reconstruction enables the stabilization of individual metal atoms<sup>[73,210–214]</sup> providing a model system to investigate the interaction between metal atoms and substrate. The highly ordered adatom array can be considered a well-defined single atom catalyst (SAC). In the course of miniaturization catalytic active nanoparticles have been continuously reduced in size resulting mostly in an increased catalytic performance due to quantum size effects.<sup>[215]</sup> Following this approach to the very end, SACs are expected to be the most active catalyst of the corresponding element.

It is still under debate whether single atoms can actually act as catalyst or if rather a small amount of metal atoms are needed for the involved multi-step processes.<sup>[215,216]</sup> Further studies to evaluate the potential of SACs are needed. However, reported SACs are generally



**Figure 6.1:** Model of spinel  $\text{Fe}_3\text{O}_4$ . Color code: O (red), octahedral  $\text{Fe}^{2+}$  and  $\text{Fe}^{3+}$  (green), tetrahedral  $\text{Fe}^{3+}$  (blue).

embedded in complex multicomponent, three dimensional structures<sup>[217–219]</sup> which are difficult to investigate by atomic resolution methods such as STM. But in order to understand the effectiveness of SACs atomic resolution is advantageous.

The highly structured adatom layers reported by the group of Parkinson offer a possible model composition to study SACs on the atomic scale by STM in vacuum.<sup>[73,210–214]</sup> Furthermore, the adatom layer on  $\text{Fe}_3\text{O}_4(001)$  are strongly bound to the substrate resulting in a remarkable stability.<sup>[211]</sup> Vacuum model experiments using Pt adatoms for CO and  $\text{H}_2$  oxidation demonstrated the potential use of adatoms on  $\text{Fe}_3\text{O}_4(001)$  for catalytic applications.<sup>[73]</sup> Regarding the reported promising results  $\text{Fe}_3\text{O}_4(001)$  enables a new substrate to study SACs in electrocatalysis in the UHV-EC transfer system.

Using  $\text{Fe}_3\text{O}_4(001)$  as substrate for SACs has to be based on a detailed characterization in order to distinguish effects of the catalyst from those of the substrate. Moreover, the topographic stability needs to be reviewed as the surface is easily oxidizable.<sup>[205,220]</sup> The reproducible synthesis of atomically well-defined  $\text{Fe}_3\text{O}_4(001)$  demands UHV environment. Therefore, sophisticated equipment for investigation is required and provided by the transfer system.

This chapter illustrates the stability of the surface reconstruction of  $\text{Fe}_3\text{O}_4(001)$  exposed to the individual steps of the transfer procedure between UHV and EC cell including the contact of aqueous solution studied by STM, LEED and XPS. Last, preliminary results utilizing Ag adatoms stabilized on  $\text{Fe}_3\text{O}_4(001)$  as ORR catalyst are discussed.

## 6.1 From Vacuum to Electrochemical Conditions

As reported earlier for the porphyrin network, the structural integrity of the UHV cleaned surface of  $\text{Fe}_3\text{O}_4(001)$  is gradually exposed to the diverse steps within the transfer system and investigated by STM.

The freshly prepared  $\text{Fe}_3\text{O}_4(001)$  (Fig. 6.2 a) exhibits the characteristic  $(\sqrt{2} \times \sqrt{2})$  R45° reconstruction (cyan lines). After exposure to 1 bar Ar, the surface reconstruction is preserved and the number of adsorbates is not significantly altered (Fig. 6.2 b) demonstrating the cleanliness of the transfer procedure.

The contact of  $\text{Fe}_3\text{O}_4(001)$  with MilliQ water results in first changes (Fig. 6.2 c). The major part of the surface still resembles the reconstructed  $\text{Fe}_3\text{O}_4(001)$ . However, the surface is covered with dark patches which are surrounded by adsorbates. Dark patches on the  $\text{Fe}_3\text{O}_4(001)$  surface have been reported by Parkinson *et al.*<sup>[72]</sup> and were attributed to oxygen vacancies. The presence of adsorbed hydroxide groups on the surface followed by an annealing step is reported to drive a catalytic reaction supposedly forming water. Exposing the surface to  $\text{H}_2\text{O}$  results likely in a layer of OH groups. According to their model, two adsorbed OH groups react to  $\text{H}_2\text{O}$  leaving an oxygen vacancy behind. The bright adsorbates mainly located around the dark patches are identified as adsorbed OH groups resulting from the surface reaction. The crystal was annealed subsequent to water exposure to facilitate STM scanning providing the thermal energy to drive the suggested reaction for creating oxygen vacancies.

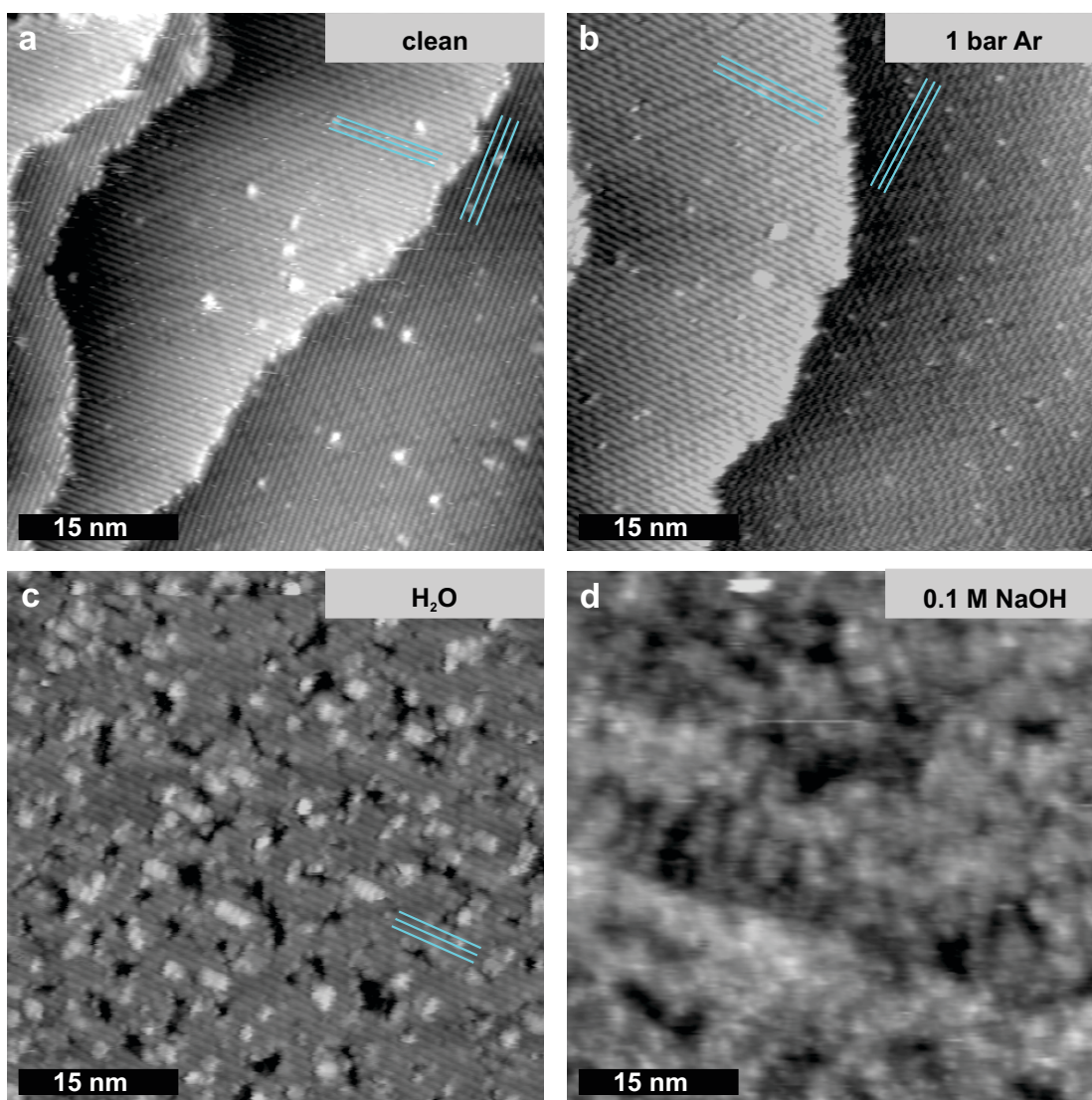
Electrolyte (0.1 M NaOH) contact changed the surface drastically (Fig. 6.2 d). In STM the typical  $\text{Fe}_3\text{O}_4(001)$  reconstruction remained undetected. The reason of the invisible reconstruction lines could be a layer of adsorbates originating from the electrolyte exposure. However, the adsorbates are not necessary limited to the components such as  $\text{H}_2\text{O}$ , OH groups and  $\text{Na}^+$  cations but might include also small gases such as  $\text{O}_2$ , CO and  $\text{CO}_2$ . This could be explained as electrolyte exposure is followed by a water rinsing step in order to remove the residual salt for enabling STM imaging afterwards. In contrast to the electrolyte which has been air depleted by Ar, the rinsing water was not air depleted introducing possibly additional gas molecules.

Alternatively, the changed surface could be explained by a combined effect of a lifted surface reconstruction and the presence of an adsorbate layer resulting in the amorphous surface appearance. Previous studies on polycrystalline  $\text{Fe}_3\text{O}_4$  have suggested the formation of a hydroxo complex at the solid-liquid interface<sup>[208]</sup> which might lift the reconstruction.

The interpretation of STM images are clearly limited and are extended by LEED for understanding long range order as well as XPS giving rise to chemical information. As STM images were meaningful for Ar and water exposure, LEED and XPS analysis were focused on the comparison of freshly prepared and postNaOH  $\text{Fe}_3\text{O}_4(001)$ .

---

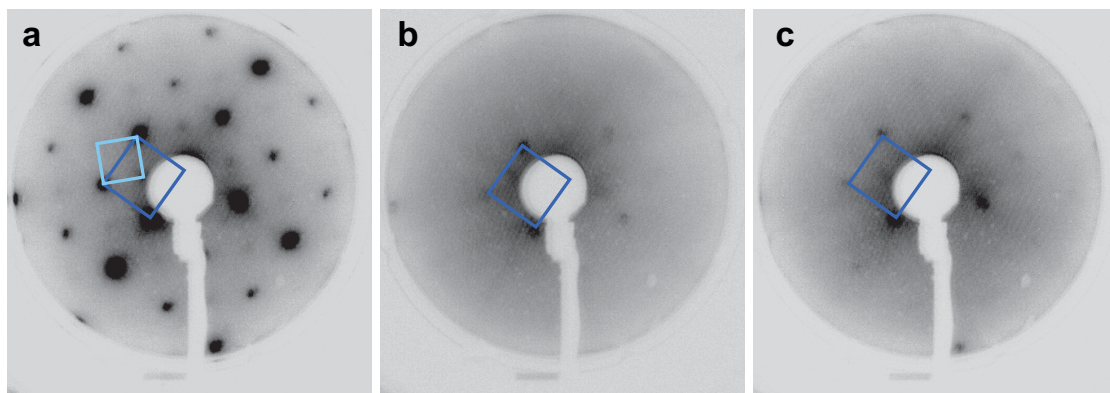
\* In collaboration with Dr. Roland Bliem (TU Vienna, Austria) and Dr. Kathrin Müller (Max Planck Institute for Solid State Research, Stuttgart, Germany).



**Figure 6.2:**  $\text{Fe}_3\text{O}_4(001)$  exposed to Ar,  $\text{H}_2\text{O}$  and NaOH. (a) STM image of freshly prepared  $\text{Fe}_3\text{O}_4(001)$ , reconstruction lines are indicated in cyan ( $I_{\text{tunnel}} = 0.5 \text{ nA}$ ;  $U_{\text{bias}} = 2.1 \text{ V}$ ); (b) postAr, 5 min exposed to 1 bar Ar ( $I_{\text{tunnel}} = 0.4 \text{ nA}$ ;  $U_{\text{bias}} = 1.4 \text{ V}$ ); (c) post $\text{H}_2\text{O}$ , exposed to MilliQ water for 5 min ( $I_{\text{tunnel}} = 0.2 \text{ nA}$ ;  $U_{\text{bias}} = 2.0 \text{ V}$ ); (d) postNaOH, 5 min in contact with 0.1 M NaOH, Ar sat. ( $I_{\text{tunnel}} = 0.1 \text{ nA}$ ;  $U_{\text{bias}} = 2.0 \text{ V}$ ).

The pristine  $\text{Fe}_3\text{O}_4(001)$  surface is determined by two different unit cells (Fig. 6.3 a). The  $(1 \times 1)$  unit cell of the substrate (blue square) and the well-reported surface reconstruction with a  $(\sqrt{2} \times \sqrt{2})$  R45° unit cell (light blue square). The low intensity of the reconstruction spots arises from a reduced long range order originating either from small terraces or from a partially unreconstructed crystal. The broad appearance of the first order spots of the  $(1 \times 1)$  unit cell supports the assumption of poor long range order. While small terraces have been observed by STM in different experiments, the absence of the reconstruction has not been observed. Thus, the small terraces together with the characteristic 90° rotation of the reconstruction

lines on adjoin terraces are responsible for the reduced long range order reflected by the low intense reconstruction diffraction spots.

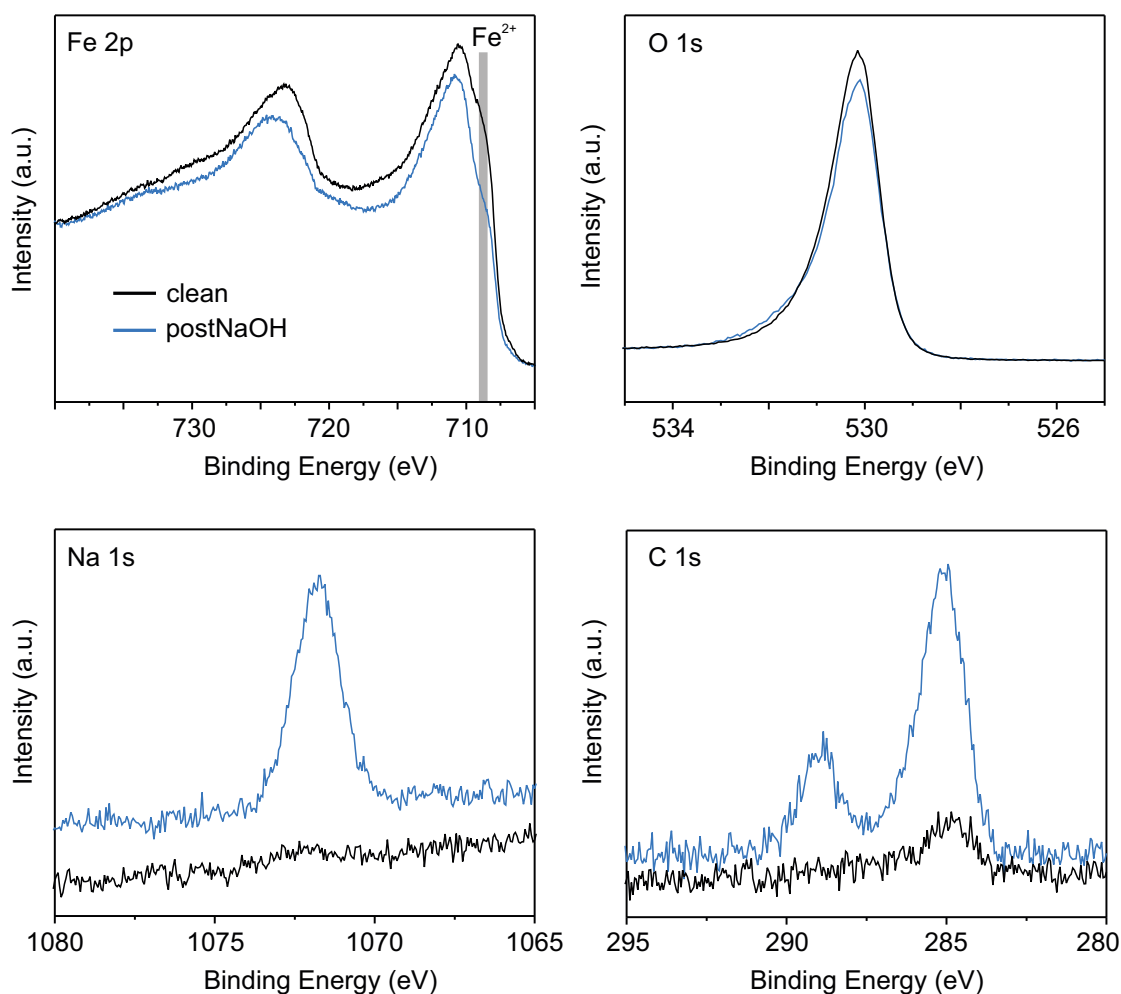


**Figure 6.3:** LEED of  $\text{Fe}_3\text{O}_4(001)$  pre and postNaOH. LEED pattern at 90 eV. (a) clean, UHV prepared; (b) exposed to NaOH for 5 min, rinsed with MilliQ water; (c) exposed to NaOH, rinsed with MilliQ water and post annealed at 150 °C for 30 min. Color code:  $(1 \times 1)$  substrate unit cell (dark blue square),  $(\sqrt{2} \times \sqrt{2})$  R45° unit cell of the surface reconstruction (light blue square).

In contrast to pristine  $\text{Fe}_3\text{O}_4(001)$ , postNaOH (Fig. 6.3 b) depicts only first order spots of the  $(1 \times 1)$  unit cell. Moreover, the intensity of the LEED pattern is clearly quenched. As demonstrated by STM, the surface is covered with adsorbates (Fig. 6.2 d) which might be the reason of the quenched intensity. The first order LEED spots of the  $(1 \times 1)$  unit cell were the most intense signals of pristine  $\text{Fe}_3\text{O}_4(001)$ . Hence, the absence of the  $(\sqrt{2} \times \sqrt{2})$  R45° reconstruction in the LEED pattern could be explained simply by a quenched signal rather than by a lifted reconstruction. In order to remove possible adsorbates, a post annealing step of 150 °C for 30 min was applied. This temperature is expected to be insufficient to recover the surface reconstruction. However, the annealing step enhances the intensity of the  $(1 \times 1)$  diffraction spots (Fig. 6.3 c). Considering the results of STM and LEED seem to indicate a lifted  $(\sqrt{2} \times \sqrt{2})$  R45° reconstruction of  $\text{Fe}_3\text{O}_4(001)$  upon NaOH exposure.

The formation of a hydroxo complex<sup>[208]</sup> to the disadvantage of the surface reconstruction might be an explanation for the reported LEED and STM results. Interestingly, the amount of OH groups in pure MilliQ water is not sufficient to lift the reconstruction. The absence of the reconstruction could also explain the similar response in electrochemical impedance spectroscopy which demonstrated similar behavior as polycrystalline  $\text{Fe}_3\text{O}_4$ .<sup>[208]</sup>

Further insights into the interaction of  $\text{Fe}_3\text{O}_4(001)$  with the electrolyte is provided by XPS (Fig. 6.4). The Fe 2p<sub>3/2</sub> peak of pristine  $\text{Fe}_3\text{O}_4(001)$  at 710.6 eV is in good agreement with literature.<sup>[71]</sup> However, postNaOH is marginally shifted to higher BEs. The shoulder at approximately 708.7 eV is assigned to  $\text{Fe}^{2+}$ <sup>[71]</sup> which clearly decreased for postNaOH. Thus, the electrolyte oxidized the surface resulting in a smaller amount of  $\text{Fe}^{2+}$  ions. Surprisingly, the O 1s peak is unchanged for both samples. Hence, further information about the hydroxo complex could not be extracted from the O 1s peak. The high intense Na 1s peak stems from the electrolyte contact as it is only present for postNaOH. The C 1s signal for postNaOH shows two



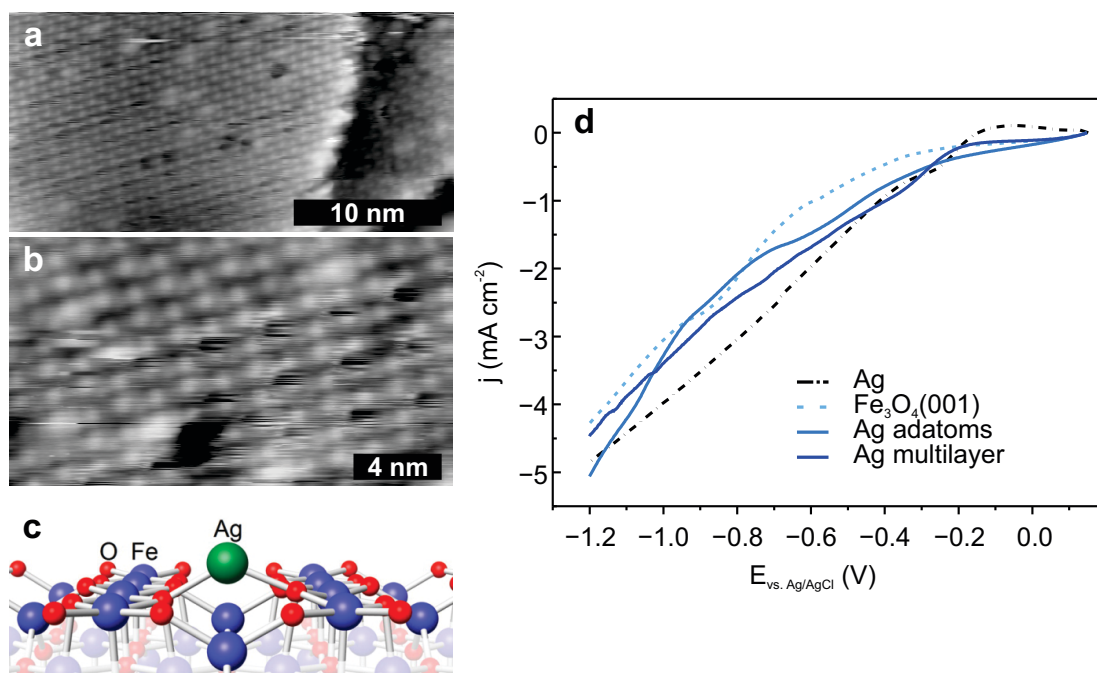
**Figure 6.4:** XPS of Fe<sub>3</sub>O<sub>4</sub>(001) pre and postNaOH. Clean Fe<sub>3</sub>O<sub>4</sub>(001) (black) and postNaOH (blue) at the following core levels: Fe 2p, O 1s, Na 1s and C 1s. XPS measurements were performed with a monochromatic Al K $\alpha$  source (Kratos Ultra, Axis).

high intense components in contrast to the clean surface which is attributed to adventitious carbon originating from air exposure during the transfer. The maxima are located at 288.9 eV attributed to C=O and 285.1 eV indicating C-C compounds.<sup>[221]</sup> Most probably, adventitious carbon stems from adsorbed hydrocarbons as well as from reactions of air CO<sub>2</sub> and CO with reactive sites of the clean surface forming amorphous carbon.

## 6.2 Decorating Fe<sub>3</sub>O<sub>4</sub>(001) by Ag for Electrocatalysis

Changing the electrocatalytic properties of materials can be easily accomplished by doping the catalyst with additional metal atoms. Doping of Fe<sub>3</sub>O<sub>4</sub>(001), for instance by TMs, might lead to a further enhancement of the catalytic performance. Ag adatoms are found to bind strongly to the Fe<sub>3</sub>O<sub>4</sub>(001) surface<sup>[71]</sup> forming a highly ordered layer along the ( $\sqrt{2} \times \sqrt{2}$ ) R45°

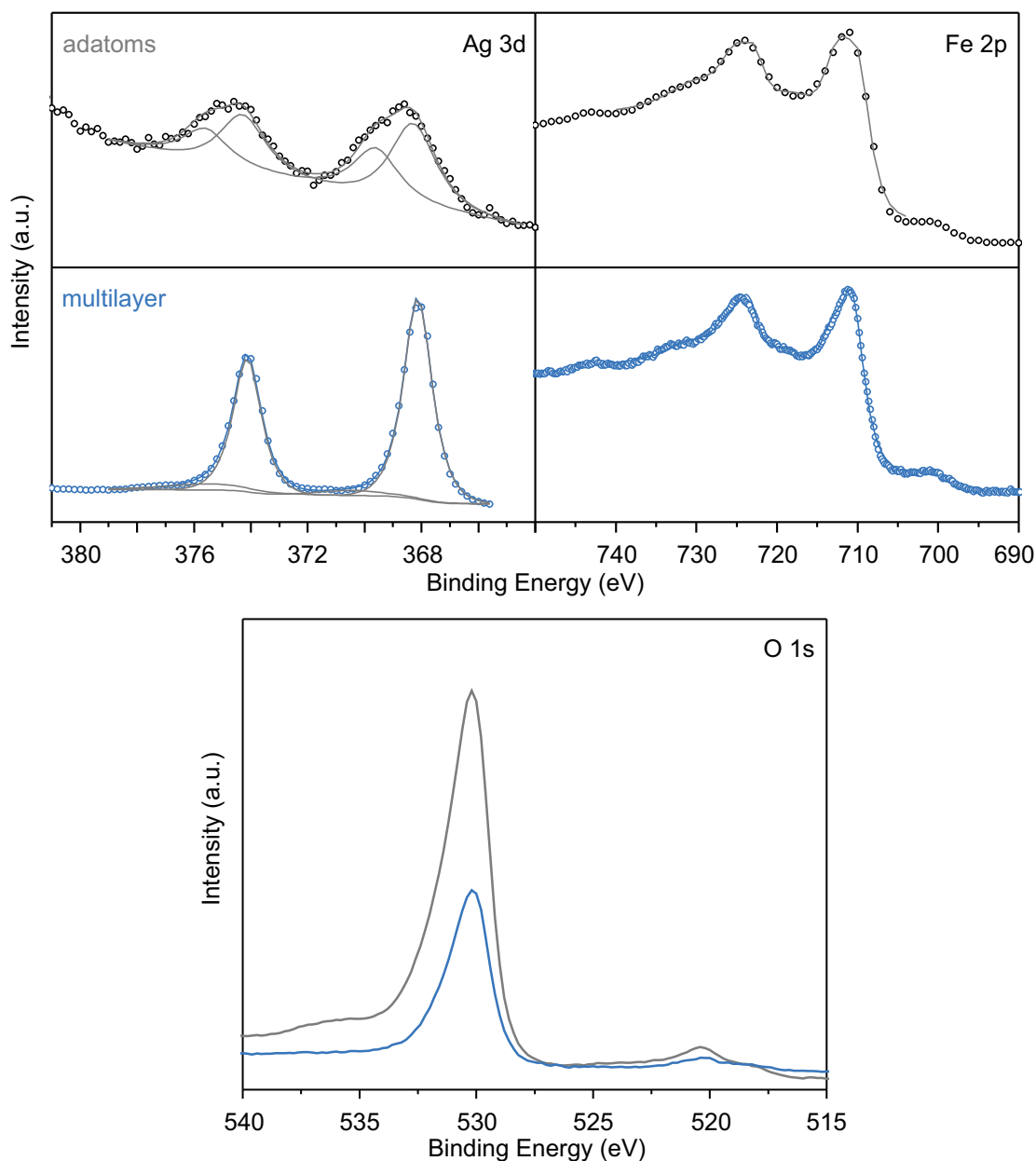
reconstruction (Fig. 6.5 a, b). Subsurface cationic vacancies enable binding of Ag adatoms to two surface oxygen forming a stable bond (Fig. 6.5 c).<sup>[211]</sup> The adatom layer could act as both as dopant of the surface as well as SAC.



**Figure 6.5:** ORR of Ag adatoms/ $\text{Fe}_3\text{O}_4(001)$ . (a) overview STM image of Ag adatom array on  $\text{Fe}_3\text{O}_4(001)$  ( $I_{\text{tunnel}} = 1 \text{ nA}$ ;  $U_{\text{bias}} = 0.7 \text{ V}$ ); (b) STM image of Ag adatoms array on  $\text{Fe}_3\text{O}_4(001)$  ( $I_{\text{tunnel}} = 0.3 \text{ nA}$ ;  $U_{\text{bias}} = 1.89 \text{ V}$ ); (c) Structural models of Ag adatoms on  $\text{Fe}_3\text{O}_4(001)$ , calculated by DFT+U<sup>[211]</sup>; (d) LSV (0.15 V to  $-1.2 \text{ V}$ ,  $50 \text{ mV s}^{-1}$ ,  $0.1 \text{ M NaOH}$ ,  $\text{O}_2$  sat.) of polycrystalline Ag (black dashed), pristine  $\text{Fe}_3\text{O}_4(001)$  (light blue dashed), Ag adatoms/ $\text{Fe}_3\text{O}_4(001)$  (blue), Ag multilayer/ $\text{Fe}_3\text{O}_4(001)$  (dark blue).

The catalytic performance towards ORR is investigated (Fig. 6.5 d). Both pristine  $\text{Fe}_3\text{O}_4(001)$  (light blue dashed) and Ag adatoms/ $\text{Fe}_3\text{O}_4(001)$  (blue) show an activation on-set potential of  $-0.23 \text{ V}$ . The value is in good agreement with literature on-set potentials of polycrystalline  $\text{Fe}_3\text{O}_4$ .<sup>[63]</sup> For both systems the current density is comparable demonstrating similar reaction rates. However, the shape of the LSVs differs.

A reference system of Ag multilayers/ $\text{Fe}_3\text{O}_4$  presents an on-set potential of  $-0.14 \text{ V}$  lying in between clean  $\text{Fe}_3\text{O}_4(001)$  ( $-0.23 \text{ V}$ ) and  $-0.08 \text{ V}$  of polycrystalline Ag (black dashed). An increasing number of Ag layers reduce the influence of the substrate on the outmost layer which is the platform of EC reactions. The reduced substrate influence explains the shift of the on-set potential towards polycrystalline Ag. All LSVs illustrate a continuously increasing current density without reaching a diffusion limit partially resulting from a continuous reduction of the Fe cations of the mixed valent  $\text{Fe}_3\text{O}_4$  lattice.<sup>[63]</sup>



**Figure 6.6:** XPS of Fe<sub>3</sub>O<sub>4</sub>(001) decorated by Ag adatoms or multilayer Ag postEC. Comparison of Ag adatoms/Fe<sub>3</sub>O<sub>4</sub>(001) (grey) and Ag multilayers/Fe<sub>3</sub>O<sub>4</sub>(001) (blue) at the following core levels: Ag 3d, Fe 2p and O 1s. The samples were investigated post ORR (0.15 V to −1.2 V, 50 mV s<sup>−1</sup>, 0.1 M NaOH, O<sub>2</sub> sat.). XPS measurements were performed with a non-monochromatic Al K $\alpha$  source and a Phoibos 150 (SPECS) analyzer.

For chemical analysis both Ag adatoms and Ag multilayers on Fe<sub>3</sub>O<sub>4</sub> were characterized by XPS postORR (Fig. 6.6). The Ag 3d<sub>5/2</sub> peak of the Ag adatoms/Fe<sub>3</sub>O<sub>4</sub>(001) can be divided into two contributions at 368.3 eV and 369.6 eV. The separated spin-orbit components Ag 3d<sub>5/2</sub> and Ag 3d<sub>7/2</sub> are split by 6.0 eV. The component at lower BE is assigned to metallic Ag<sup>[222,223]</sup> while the signal at higher BE is supposedly an oxidized Ag species<sup>[222]</sup>. The presence of metallic

Ag could be explained by local Ag cluster formation.<sup>[211]</sup> However, the origin of the oxidized species is not trivial.

An idea gives the report of Xue *et al.*<sup>[222]</sup>. They report similar BEs for a Ag<sup>+</sup> state originating from single Ag<sup>+</sup> ions stabilized between two N of imidazole molecules. N has a similar electronegativity as O and might resemble the chemical environment of Ag adatoms/Fe<sub>3</sub>O<sub>4</sub>(001) bound to two O atoms at a cationic vacancy in the Fe<sub>3</sub>O<sub>4</sub>(001) lattice.<sup>[211]</sup> The explanation of two different oxidation states present on the surface seems to be plausible supporting the predicted +1 oxidation state for the Ag adatoms/Fe<sub>3</sub>O<sub>4</sub>(001).<sup>[211]</sup> However, the Ag oxidation state of +1 is rather surprising as most of the literature report Ag<sup>0</sup> in Ag doped TM-oxide nanoparticles.<sup>[223]</sup>

Alternatively, the component at higher BEs could be also explained by a size effect which is believed to shift XPS peaks to higher BEs for smaller sized nanoparticles.<sup>[224]</sup> In this case the oxidation state remains metallic. The shift of BEs is only apparent to a critical size of the particles. As soon as the particles overcome the limit, the BEs are found to be at the position of bulk signals.<sup>[224]</sup> Thus, instead of different oxidation states, the size effect could explain the discrepancy of energy position at Ag 3d<sub>5/2</sub>. Nevertheless, 369.6 eV represents the Ag adatoms while 368.3 eV are assigned to bigger Ag clusters. Both tentative explanations confirm the presence of individually stabilized Ag atoms after ORR. In contrast, Ag multilayers show an intense metallic Ag 3d<sub>5/2</sub> peak located at 368.1 eV as expected.<sup>[225]</sup>

The Fe 2p peak is at 711.5 eV for Ag adatoms and 711.2 eV for Ag multilayers. The BE is shifted by approximately 1 eV to higher BE in respect to clean Fe<sub>3</sub>O<sub>4</sub>(001). On the one hand, the Fe 2p<sub>3/2</sub> core level lacks the typical Fe<sup>2+</sup> shoulder demonstrating a more oxidized surface. On the other hand, the spectra also lacks the characteristic Fe<sup>3+</sup> shake-up satellite at 719 eV.<sup>[226,227]</sup> Since the applied potential during EC is reductive<sup>[63,228]</sup>, it cannot explain the oxidized sample. Furthermore, electrolyte contact can also be excluded as the exposure to the electrolyte of 5 min resulted only in a marginal shift to higher BE and a reduced but still present Fe<sup>2+</sup> shoulder (Fig. 6.4). In addition, the Fe<sub>3</sub>O<sub>4</sub>(001) substrate underneath Ag multilayers should not be affected by the electrolyte. Therefore, the substrate-Ag interaction is assumed to be the reason for the oxidized Fe signal.

It has been speculated that Ag doping could transform the Fe<sub>3</sub>O<sub>4</sub> substrate partially into Fe<sub>2</sub>O<sub>3</sub>.<sup>[229,230]</sup> The oxidation of the surface due to Ag atoms could explain the conflict of the applied reductive potential and the oxidized Fe 2p peak. However, this effect of Ag is still under debate.<sup>[229–231]</sup> It is not evident if the oxidized Fe is due to the Ag or the ORR experiment.

The position of the O 1s core level is located at 530.2 eV for both samples corresponding to a negligible shift of 0.1 eV to higher BEs in respect to pristine Fe<sub>3</sub>O<sub>4</sub>(001) inhibiting strong conclusions. The discrepancy in intensity of the adatom and multilayer sample can be explained by the amount of Ag on the surface. The multilayer sample consists of several layers of Ag quenching the signal of the underlying oxide resulting in a strongly reduced O 1s signal. Regarding the rather strong change of BE of Ag doped Fe<sub>3</sub>O<sub>4</sub>(001) at the Fe 2p peak in contrast

to the small changes at the O 1s core level might be explained by a stronger interaction of Ag with the Fe cations than with the oxygen anion lattice although Bliem *et al.*<sup>[211]</sup> reported a binding of Ag to O in the position of cationic vacancies.

### 6.3 Summary

STM investigation of Fe<sub>3</sub>O<sub>4</sub>(001) demonstrated the stability of the surface in 1 bar Ar as well as MilliQ water. However, electrolyte exposure resulted in a lifted reconstruction determined by STM and LEED. Supposedly, the formation of a hydroxo complex promotes the lifting. XPS remained unaffected at Fe 2p and O 1s core levels.

Preliminary results for metal doping using the example of Ag were presented. Ag adatoms could not alter the ORR of Fe<sub>3</sub>O<sub>4</sub>(001). XPS was inconclusive about the oxidation state of Ag adatoms which could be either Ag<sup>0</sup> or Ag<sup>+</sup>. Nevertheless, the Ag 3d core level confirmed the presence of Ag adatoms postORR demonstrating the potential use of Fe<sub>3</sub>O<sub>4</sub>(001) as SAC support material. The lifting of the reconstruction might change the binding position of the individual Ag atoms but is not inducing large cluster formation. The diverse surface structure due to the lifted reconstruction might also explain the stronger interaction of Ag with Fe instead of O.

## Conclusion and Outlook

The complexity of the oxygen half-cell reaction originates from the four-electron transfer and consequential numerous bond formation and cleavage steps, all occurring on the molecular scale. Each reaction step requires different conditions on the electrocatalyst. Thus, finding a catalyst for the whole reaction is demanding. Insights into the electrocatalyst's structure on the fundamental atomic level and its stability on the molecular scale are crucial to allow a material-by-design approach.

This thesis illuminates the relation between interactions of the participating components in the catalytic material and its performance. The stability of MOCN electrocatalysts strongly depend on molecule-metal-substrate interactions. Furthermore, the applied potential as well as the electrolyte treat the catalyst quite aggressively, at times, such that active sites are not necessarily in agreement with expectations.

### Metal-Organic Coordination Networks as Electrocatalysts

**Chapter 3** illustrates an on-surface redox transmetalation of Fe and Cu porphyrin by Co sublimation occurring during electrocatalyst's preparation. At RT cobalt deposition lead to an estimated 50 % exchange ratio of Fe demonstrating a novel on-surface fabrication strategy for nanostructures. The experimental observations were supported by DFT illuminating possible intermediates and reaction mechanisms. The calculations suggest a thermodynamically driven exchange process initiated by charge transfer between the two involved metal centers Co and Fe. For the exchange the Co atom attacks from the top and lands close to the Fe center on the molecule. Oxidized Co coordinated in the porphyrin core stabilizing the expelled Fe center between molecule and Au(111) surface is considered as most stable final state. The back reaction of Fe substituting Co does not occur supporting experimentally the thermodynamic driving force. Interestingly, the availability of a second coordination site by using TPyP as molecular ligand did not inhibit the transmetalation.

The exact synthesis pathway of preparing the reported network influences strongly the OER performance.<sup>[103]</sup> For a controlled fabrication via transmetalation, the influencing parameters need to be investigated e.g. temperature and amount of co-deposited metal, influence of the substrate and type of metal centers. Comprehension of the architecture and the interaction

## Conclusion and Outlook

---

of MOCNs is crucial to go one step further towards understanding electrocatalysis at these interfaces.

**Chapter 4** was dedicated to the investigation of structural stability postEC. Although ORR and OER are formally opposite reactions, the demands for the individual reactions are entirely different. STM demonstrated a reduced long-range order already after the very first cycle of ORR which might be due to reorganization of the molecules on the surface. The MOCN persists up to 11 repetitions of ORR. Consistently, XAS confirmed the integrity of the porphyrins after 10 cycles leading to the conclusion that the network itself catalyzes ORR. After 111 cycles the molecules seem to degrade.

In contrast, the OER occurs at a more positive voltage. The molecular network was investigated by STM after exposure to the electrolyte and at different potential windows. The MOCN decomposes as soon as positive potentials vs. the Ag/AgCl RE are applied. The drastic structural change already after the very first cycle is due to oxide formation of the metal centers which were formally residing in the porphyrins. These findings point out the importance of combining imaging techniques with high resolution and analytical tools sensitive to the chemical environment. The actual catalyst is not the MOCN but a Fe/Co oxide. The early formation of the oxide explains the electrocatalytic stability over at least 15 cycles.<sup>[103]</sup> It is not obvious if the organic backbone is involved in the active site or rather oxidatively cleaved and dissolved into the electrolyte.

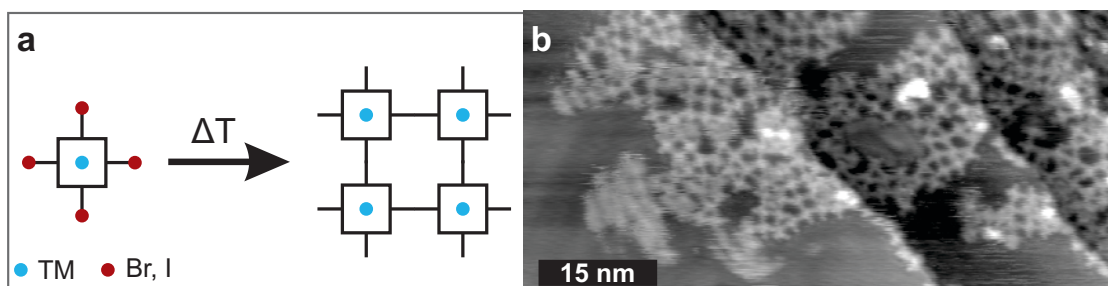
The first part highlights the importance of studying catalyst's stability during electrocatalysis. Although the electrocatalytic stability of the catalyst is commonly explored in detail, the surface structure on the molecular scale is barely investigated. Here, the effect of the exact nature of the MOCN on EC was explored. Indeed, the order during MOCN preparation determines the architecture as demonstrated in Chap. 3. Furthermore, the applied potential decides about stability and can even form different chemical environments using MOCN as precursor for the real catalyst. Although simplified systems were prepared under well-controlled conditions, the electrolyte and applied potential influence the material drastically.

## Future Perspectives of Molecular Electrocatalysts

The stability of molecular networks is a major challenge when using MOCNs as electrocatalysts and can be significantly increased by replacing self-assembled structures based on weak intermolecular bonds by covalent networks.

A well-studied reaction pathway inspired by C-C bond formation in organic chemistry is the Ullmann-type coupling (Fig. 6.7).<sup>[232,233]</sup> Organic monomers are functionalized by halogens e.g. Br or I. By heat treatment, the halogen bonds are cleaved and two molecules form a covalent C-C bond (Fig. 6.7 a).

Utilizing different halogens enables a stepped reaction by cleaving one bond after the other at different temperatures resulting in sophisticated nanoarchitecture.<sup>[233,234]</sup> The structure of the



**Figure 6.7:** On-surface polymerization via Ullmann-type coupling. (a) Schematic on-surface polymerization via Ullmann-type coupling of porphyrins to create an extended 2D polymer. Halogens like Br or I (red) are split off due to heat treatment in order to form a C-C bond. The cavity in the porphyrin can be filled with additional TMs (blue) to implement catalytic active sites. (b) STM image of a 2D FeTPP polymer synthesized from a Fe-Tetra(4-Bromophenyl)porphyrin monomer via heat treatment at 523 K on Au(111) ( $I_{\text{tunnel}} = 0.26 \text{ nA}$ ;  $U_{\text{bias}} = -1.26 \text{ V}$ ).

covalent network is not expected to be influenced as strongly by the electrolyte as structures based on weaker bonds. Furthermore, the networks are fairly large thus the probability of dissolving parts or even the whole network from the crystal when touching the electrolyte is eliminated. The morphology of the covalent network depends on the orientation and number of the halogens. The various architectures might affect the catalytic response. Moreover, the organic chemistry toolbox could be utilized to tailor the electronic and catalytic properties by suitable functional groups. For instance, large molecules like MPs could serve as building blocks including the active TM in the macrocycle (Fig. 6.7 b). Alternatively, the organic polymer could be modified with TMs using a polymer forming nanopores to stabilize small clusters down to single atoms.<sup>[235]</sup>

## Transition Metal Oxide Electrocatalysts

The discovery of the potential induced oxide formation introduced the second part of this thesis focusing on Co and Fe oxides.

### Co Islands on Au(111)

**Chapter 5** followed similar stability tests as Chap. 4 exploring metallic Co islands. Vacuum prepared Co islands on Au(111) were exposed to the different steps of the transfer and the EC cell, investigated by a combined STM-XPS study. In order to discriminate the effect of Co and O, first metallic Co clusters were studied. Co initiates oxidation already in Ar (5.0) atmosphere which is continued by contacting water and eventually the electrolyte of 0.1 M NaOH. Moreover, the alkaline environment promotes sintering of formally small and well-distributed clusters to large agglomerates of about 20 nm.

Surprisingly, both the morphology and the chemical environment change drastically from pre to postOER. Although oxides are reported to be stable under the harsh OER conditions, higher

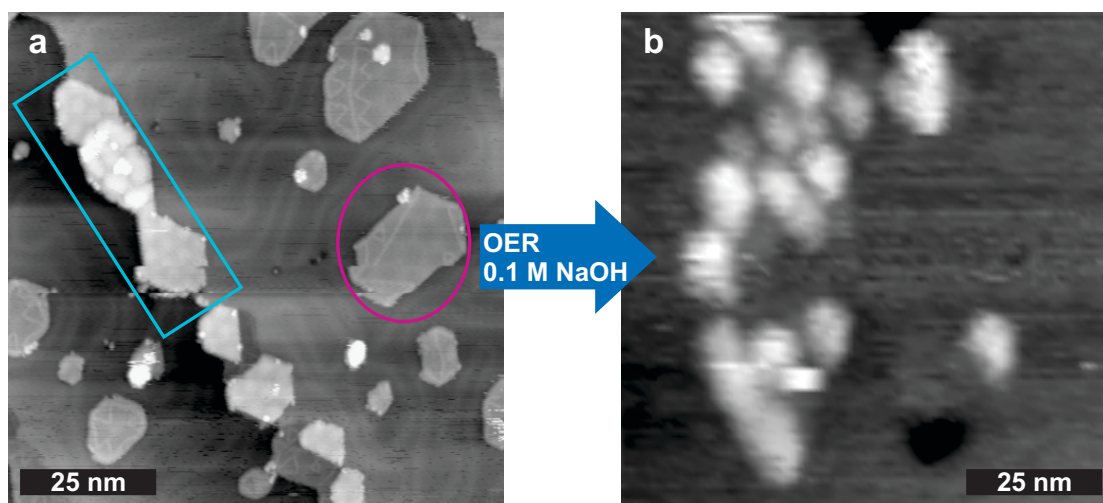
## Conclusion and Outlook

stability of the oxidized Co cluster could not be confirmed. The similar OER performance of the two entirely different prepared oxide structures, potential induced oxidation of the porphyrin MOCN and oxidized Co cluster, is surprising as the atomic structure is expected to be different. Apparently, the oxidation state of Co achieved by the electrolyte is not the most active or stable species. The experimental approach needs to be optimized to gain insights about the oxide structure and working principles.

### Optimizing the Model System: Vacuum Prepared Well-Defined Oxide Structures as Model Catalyst for the Oxygen Evolution Reaction

Preparing well-defined Co oxide in UHV could be an alternative synthesis pathway. The UHV-prepared 2D Co oxide structures<sup>[185,194]</sup> enable STM investigation. Previous experiments in UHV demonstrated activity towards the water splitting reaction.<sup>[186,194]</sup>

Preliminary results are presented in Fig. 6.8. The morphology changes from pre to postOER. The structure of monolayered oxide could not be confirmed postOER (pink circle). In contrast, the layered oxide structure (cyan square), most probably trilayered oxide, was observed postOER. However, STM demonstrates sintering of the islands due to OER. Further studies including chemical sensitive methods such as XPS are needed to complete the picture.



**Figure 6.8:** UHV-prepared 2D Co oxide islands utilized as OER electrocatalyst. 2D Co oxide islands (a) as-prepared: layered oxide (cyan rectangular) and monolayer oxide (pink circle) ( $I_{\text{tunnel}} = 0.2 \text{ nA}$ ;  $U_{\text{bias}} = 1.4 \text{ V}$ ); (b) postOER ( $-1.2 \text{ V}$  to  $0.7 \text{ V}$ ,  $50 \text{ mV s}^{-1}$ ,  $0.1 \text{ M NaOH}$ ,  $\text{O}_2 \text{ sat.}$ ,  $10 \text{ CVs}$ ), demonstrating layered oxide ( $I_{\text{tunnel}} = 0.3 \text{ nA}$ ;  $U_{\text{bias}} = 1.5 \text{ V}$ ).\*

Besides the monometallic  $\text{CoO}_x$ , mixed metallic oxides could be also utilized as electrocatalysts. Mixed oxides could lead to an increased performance compared to noble metal oxides such as  $\text{IrO}_x$ .<sup>[9,236]</sup> For instance, co-depositing Co and Fe in UHV and subsequent oxidation could

\* STM images recorded by Anton Makoveev (Central European Institute of Technology, Brno, Czech Republic) and Jakob Fester (Interdisciplinary Nanoscience Center, University Aarhus University, Denmark)

lead to well-defined bimetallic oxide structures. The bimetallic model system might help to explore active sites as well as stability in different atmospheres and eventually to understand the influence of the second metal on catalytic performance.

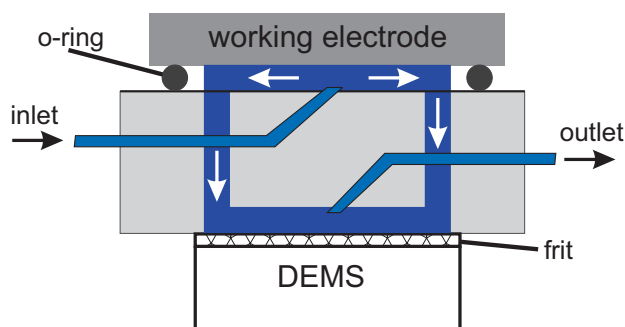
### **Fe<sub>3</sub>O<sub>4</sub>(001) as Substrate for Single Atom Catalysts**

A Fe<sub>3</sub>O<sub>4</sub>(001) crystal served as novel supporting material for TM adatoms in **Chapter 6**. Similarly as in previous chapters, the behavior of the diverse substrate was investigated in the transfer system. The surface persists the transfer which is evidenced by STM. The situation changes as soon as the crystal is exposed to the alkaline electrolyte causing the lifting of the typical ( $\sqrt{2} \times \sqrt{2}$ ) R45° reconstruction studied by LEED and STM. An explanation could be the formation of a hydroxo complex resulting in a restructuring of the surface atoms while lifting the reconstruction. Decorating Fe<sub>3</sub>O<sub>4</sub>(001) with Ag adatoms leaves ORR performance unchanged. However, the stability of the Ag adatoms postORR was confirmed by XPS.

Fe<sub>3</sub>O<sub>4</sub>(001) offers a different synthesis route to study SACs on the atomic scale. The stability of adatoms confirms a possible usage as SAC substrate. For instance, the utilization of Co might lead to enhanced catalytic performance due to a supportive interaction of Fe and Co.<sup>[90,103,237]</sup> Following a similar synthesis pathway as for Ag adatoms, Co has been successfully stabilized on Fe<sub>3</sub>O<sub>4</sub>(001).<sup>[214]</sup>

### **Improving the Experimental Set-Up**

Utilizing the meniscus configuration as presented in this thesis limits the investigation of electrocatalysis to static conditions. Generally, rotating disk electrodes or rotating ring disk electrodes are used for mechanistic or kinetic studies in EC. Additional advantage of the ring disk electrode is the possibility to detect intermediates or products.



**Figure 6.9:** Schematic flow cell. Side view: The WE is pressed on an O-ring creating a volume for the electrolyte in front of the electrode surface. The electrolyte enters the cell set-up through the inlet. The electrolyte is pumped over the surface and the frit in front of the DEMS. Ions are able to pass the frit and the chemical nature of the intermediates will be analyzed by DEMS. Finally the electrolyte leaves the cell through the outlet.

## Conclusion and Outlook

---

The described UHV-EC transfer system is limited by a static sample holder. Hence, only by a flow cell (Fig. 6.9), moving the electrolyte over the surface of the working electrode in a controlled fashion, enables similar dynamics to study kinetics.<sup>[238–240]</sup> Additionally, a flow cell could be combined with either DEMS<sup>[241]</sup> or gaschromatography-mass spectrometry (GC-MS) enabling the identification of intermediates and products. The UHV-EC transfer system could be significantly valorized by including kinetic studies as well as investigation of intermediates and products spectrometrically.

# Bibliography

- [1] Arrhenius, S. *Worlds in the Making; The Evolution of the Universe* (Harper & Brothers, New York, London, 1908).
- [2] Callendar, G. S. The Artificial Production of Carbon Dioxide and Its Influence on Temperature. *Quarterly Journal of the Royal Meteorological Society* **64**, 223–240 (1938).
- [3] Keeling, C. D. The Concentration and Isotopic Abundances of Carbon Dioxide in the Atmosphere. *Tellus* **12**, 200–203 (1960).
- [4] Emmert, J. T., Stevens, M. H., Bernath, P. F., Drob, D. P. & Boone, C. D. Observations of Increasing Carbon Dioxide Concentration in Earth's Thermosphere. *Nature Geoscience* **5**, 868–871 (2012).
- [5] Baes, C. F., Goeller, H. E., Olson, J. S. & Rotty, R. M. Carbon Dioxide and Climate: The Uncontrolled Experiment. *American Scientist* **65**, 310–320 (1977).
- [6] Katsounaros, I., Cherevko, S., Zeradjanin, A. R. & Mayrhofer, K. J. J. Oxygen Electrochemistry as a Cornerstone for Sustainable Energy Conversion. *Angewandte Chemie - International Edition* **53**, 102–121 (2014).
- [7] Hong, W. T. *et al.* Toward the Rational Design of Non-Precious Transition Metal Oxides for Oxygen Electrocatalysis. *Energy and Environmental Science* **8**, 1404–1427 (2015).
- [8] Dresch, S. *et al.* An Efficient Bifunctional Two-Component Catalyst for Oxygen Reduction and Oxygen Evolution in Reversible Fuel Cells, Electrolyzers and Rechargeable Air Electrodes. *Energy Environ. Sci.* **9**, 2020–2024 (2016).
- [9] McCrory, C. C. L., Jung, S., Peters, J. C. & Jaramillo, T. F. Benchmarking Heterogeneous Electrocatalysts for the Oxygen Evolution Reaction. *Journal of the American Chemical Society* **135**, 16977–16987 (2013).
- [10] Cook, T. R. *et al.* Solar Energy Supply and Storage for the Legacy and Nonlegacy Worlds. *Chemical Reviews* **110**, 6474–6502 (2010).
- [11] Dau, H. *et al.* The Mechanism of Water Oxidation: From Electrolysis via Homogeneous to Biological Catalysis. *ChemCatChem* **2**, 724–761 (2010).

## Bibliography

---

- [12] Lewis, N. S. & Nocera, D. G. Powering the Planet: Chemical Challenges in Solar Energy Utilization. *Proceedings of the National Academy of Sciences* **103**, 15729–15735 (2006).
- [13] Lide, D. R. *CRC Handbook of Chemistry and Physics* (CRC Press Inc, USA, 2000), 82nd edn.
- [14] Gasteiger, H. A., Kocha, S. S., Sompalli, B. & Wagner, F. T. Activity Benchmarks and Requirements for Pt, Pt-Alloy, and Non-Pt Oxygen Reduction Catalysts for PEMFCs. *Applied Catalysis B: Environmental* **56**, 9–35 (2005).
- [15] Adler, S. B. Factors Governing Oxygen Reduction in Solid Oxide Fuel Cell Cathodes. *Chemical Reviews* **104**, 4791–4844 (2004).
- [16] Armand, M. & Tarascon, J.-M. Building Better Batteries. *Nature* **451**, 652–657 (2008).
- [17] Gasteiger, H. A. & Marković, N. M. Just a Dream—or Future Reality? *Science* **324**, 48–49 (2009).
- [18] Whitesides, G. M. & Crabtree, G. W. Don't Forget Long-Term Fundamental Research in Energy. *Science* **315**, 796–798 (2007).
- [19] Stamenkovic, V. R., Strmcnik, D., Lopes, P. P. & Marković, N. M. Energy and Fuels from Electrochemical Interfaces. *Nature Materials* **16**, 57–69 (2016).
- [20] Gasteiger, H. A. & Ross, P. N. Oxygen Reduction on Platinum Low-Index Single-Crystal Surfaces in Alkaline Solution: Rotating Ring Disk Pt(hkl) Studies. *The Journal of Physical Chemistry* **100**, 6715–6721 (1996).
- [21] Marković, N. M., Gasteiger, H. A., Ross, P. N., Berkeley, L. & Division, M. S. Kinetics of Oxygen Reduction on Pt(hkl) Electrodes: Implications for the Crystallite Size Effect with Supported Pt Electrocatalysts. *Journal of The Electrochemical Society* **144**, 1591 (1997).
- [22] Chen, A. & Holt-Hindle, P. Platinum-Based Nanostructured Materials: Synthesis, Properties, and Applications. *Chemical Reviews* **110**, 3767–3804 (2010).
- [23] Frydendal, R. *et al.* Benchmarking the Stability of Oxygen Evolution Reaction Catalysts: The Importance of Monitoring Mass Losses. *ChemElectroChem* **1**, 2075–2081 (2014).
- [24] Cherevko, S. *et al.* Oxygen and Hydrogen Evolution Reactions on Ru, RuO<sub>2</sub>, Ir, and IrO<sub>2</sub> Thin Film Electrodes in Acidic and Alkaline Electrolytes: A Comparative Study on Activity and Stability. *Catalysis Today* **262**, 170–180 (2016).
- [25] Lee, Y., Suntivich, J., May, K. J., Perry, E. E. & Shao-Horn, Y. Synthesis and Activities of Rutile IrO<sub>2</sub> and RuO<sub>2</sub> Nanoparticles for Oxygen Evolution in Acid and Alkaline Solutions. *The Journal of Physical Chemistry Letters* **3**, 399–404 (2012).
- [26] Antolini, E. Iridium as Catalyst and Cocatalyst for Oxygen Evolution/Reduction in Acidic Polymer Electrolyte Membrane Electrolyzers and Fuel Cells. *ACS Catalysis* **4**, 1426–1440 (2014).

- [27] Reier, T., Oezaslan, M. & Strasser, P. Electrocatalytic Oxygen Evolution Reaction (OER) on Ru, Ir, and Pt Catalysts: A Comparative Study of Nanoparticles and Bulk Materials. *ACS Catalysis* **2**, 1765–1772 (2012).
- [28] Gorlin, Y. & Jaramillo, T. F. A Bifunctional Nonprecious Metal Catalyst for Oxygen Reduction and Water Oxidation. *Journal of the American Chemical Society* **132**, 13612–13614 (2010).
- [29] Paulus, U. A., Wokaun, A. & Scherer, G. G. Oxygen Reduction on Carbon-Supported Pt-Ni and Pt-Co Alloy Catalysts. *The Journal of Physical Chemistry B* **106**, 4181–4191 (2002).
- [30] Shao, M., Peles, A. & Shoemaker, K. Electrocatalysis on Platinum Nanoparticles: Particle Size Effect on Oxygen Reduction Reaction Activity. *Nano Letters* **11**, 3714–3719 (2011).
- [31] Taylor, S., Fabbri, E., Levecque, P., Schmidt, T. J. & Conrad, O. The Effect of Platinum Loading and Surface Morphology on Oxygen Reduction Activity. *Electrocatalysis* **7**, 287–296 (2016).
- [32] Rabis, A., Rodriguez, P. & Schmidt, T. J. Electrocatalysis for Polymer Electrolyte Fuel Cells: Recent Achievements and Future Challenges. *ACS Catalysis* **2**, 864–890 (2012).
- [33] den Boer, D. *et al.* Detection of Different Oxidation States of Individual Manganese Porphyrins During Their Reaction with Oxygen at a Solid/Liquid Interface. *Nature Chemistry* **5**, 621–7 (2013).
- [34] Jasinski, R. A New Fuel Cell Cathode Catalyst. *Nature* **201**, 1212–1213 (1964).
- [35] Hatay, I. *et al.* Proton-Coupled Oxygen Reduction at Liquid-Liquid Interfaces Catalyzed by Cobalt Porphine. *Journal of the American Chemical Society* **131**, 13453–13459 (2009).
- [36] Wang, D. & Groves, J. T. Efficient Water Oxidation Catalyzed by Homogeneous Cationic Cobalt Porphyrins with Critical Roles for the Buffer Base. *Proceedings of the National Academy of Sciences of the United States of America* **110**, 15579–84 (2013).
- [37] Su, B. *et al.* Molecular Electrocatalysis for Oxygen Reduction by Cobalt Porphyrins Adsorbed at Liquid/Liquid Interfaces. *Journal of the American Chemical Society* **132**, 2655–2662 (2010).
- [38] Nakazono, T., Parent, A. R. & Sakai, K. Cobalt Porphyrins as Homogeneous Catalysts for Water Oxidation. *Chemical Communications* **49**, 6325–6327 (2013).
- [39] Costentin, C., Dridi, H. & Savéant, J.-M. Molecular Catalysis of O<sub>2</sub> Reduction by Iron Porphyrins in Water: Heterogeneous versus Homogeneous Pathways. *Journal of the American Chemical Society* **137**, 13535–13544 (2015).

- [40] Han, Y., Wu, Y., Lai, W. & Cao, R. Electrocatalytic Water Oxidation by a Water-Soluble Nickel Porphyrin Complex at Neutral pH with Low Overpotential. *Inorganic Chemistry* **54**, 5604–5613 (2015).
- [41] Jiang, L., Cui, L. & He, X. Cobalt-Porphyrin Noncovalently Functionalized Graphene as Nonprecious-Metal Electrocatalyst for Oxygen Reduction Reaction in an Alkaline Medium. *Journal of Solid State Electrochemistry* **19**, 497–506 (2015).
- [42] Shi, C. & Anson, F. C. Catalytic Pathways for the Electroreduction of Oxygen by Iron Tetrakis(4-N-methylpyridyl)porphyrin or Iron Tetraphenylporphyrin Adsorbed on Edge Plane Pyrolytic Graphite Electrodes. *Inorganic Chemistry* **29**, 4298–4305 (1990).
- [43] Song, E., Shi, C. & Anson, F. C. Comparison of the Behavior of Several Cobalt Porphyrins as Electrocatalysts for the Reduction of O<sub>2</sub> at Graphite Electrodes. *Langmuir* **14**, 4315–4321 (1998).
- [44] Stepanow, S., Lin, N. & Barth, J. V. Modular Assembly of Low-Dimensional Coordination Architectures on Metal Surfaces. *Journal of Physics: Condensed Matter* **20**, 184002 (2008).
- [45] Gottfried, J. M. Surface Chemistry of Porphyrins and Phthalocyanines. *Surface Science Reports* **70**, 259–379 (2015).
- [46] Auwärter, W., Écija, D., Klappenberger, F. & Barth, J. V. Porphyrins at Interfaces. *Nature Chemistry* **7**, 105–120 (2015).
- [47] Koslowski, U. I., Abs-Wurmbach, I., Fiechter, S. & Bogdanoff, P. Nature of the Catalytic Centers of Porphyrin-Based Electrocatalysts for the ORR: A Correlation of Kinetic Current Density with the Site Density of Fe-N<sub>4</sub> Centers. *The Journal of Physical Chemistry C* **112**, 15356–15366 (2008).
- [48] Dodelet, J.-P. Oxygen Reduction in PEM Fuel Cell Conditions: Heat-Treated Non-Precious Metal-N<sub>4</sub> Macrocycles and Beyond. In Zagal, J. H., Bedioui, F. & Dodelet, J.-P. (eds.) *N<sub>4</sub>-Macrocyclic Metal Complexes*, 83–147 (Springer New York, New York, 2006).
- [49] Pylypenko, S., Mukherjee, S., Olson, T. S. & Atanassov, P. Non-Platinum Oxygen Reduction Electrocatalysts Based on Pyrolyzed Transition Metal Macrocycles. *Electrochimica Acta* **53**, 7875–7883 (2008).
- [50] Wiesener, K. N<sub>4</sub>-Chelates as Electrocatalyst for Cathodic Oxygen Reduction. *Electrochimica Acta* **31**, 1073–1078 (1986).
- [51] Lefèvre, M., Proietti, E., Jaouen, F. & Dodelet, J.-P. Iron-Based Catalysts with Improved Oxygen Reduction Activity in Polymer Electrolyte Fuel Cells. *Science* **324**, 71–74 (2009).
- [52] Holliday, B. J. & Mirkin, C. A. Strategies for the Construction of Supramolecular Compounds Through Coordination Chemistry. *Angewandte Chemie - International Edition* **40**, 2022–2043 (2001).

- [53] Barth, J. V., Costantini, G. & Kern, K. Engineering Atomic and Molecular Nanostructures at Surfaces. *Nature* **437**, 671–679 (2005).
- [54] Bartels, L. Tailoring Molecular Layers at Metal Surfaces. *Nature Chemistry* **2**, 87–95 (2010).
- [55] Murphy, B. E. *et al.* Homolytic Cleavage of Molecular Oxygen by Manganese Porphyrins Supported on Ag(111). *ACS Nano* **8**, 5190–8 (2014).
- [56] Fabris, S. *et al.* Oxygen Dissociation by Concerted Action of Di-Iron Centers in Metal-Organic Coordination Networks at Surfaces: Modeling Non-Heme Iron Enzymes. *Nano Letters* **11**, 5414–20 (2011).
- [57] Yoshimoto, S., Tada, A. & Itaya, K. In Situ Scanning Tunneling Microscopy Study of the Effect of Iron Octaethylporphyrin Adlayer on the Electrocatalytic Reduction of O<sub>2</sub> on Au(111). *The Journal of Physical Chemistry B* **108**, 5171–5174 (2004).
- [58] Gu, J.-Y., Cai, Z.-F., Wang, D. & Wan, L.-J. Single-Molecule Imaging of Iron-Phthalocyanine-Catalyzed Oxygen Reduction Reaction by In Situ Scanning Tunneling Microscopy. *ACS Nano* **10**, 8746–8750 (2016).
- [59] Gutzler, R., Stepanow, S., Grumelli, D., Lingenfelder, M. & Kern, K. Mimicking Enzymatic Active Sites on Surfaces for Energy Conversion Chemistry. *Accounts of Chemical Research* **48**, 2132–2139 (2015).
- [60] Lyons, M. E. G. & Brandon, M. P. A Comparative Study of the Oxygen Evolution Reaction on Oxidised Nickel, Cobalt and Iron Electrodes in Base. *Journal of Electroanalytical Chemistry* **641**, 119–130 (2010).
- [61] Castro, E. B. & Gervasi, C. A. Electrodeposited Ni-Co-Oxide Electrodes: Characterization and Kinetics of the Oxygen Evolution Reaction. *International Journal of Hydrogen Energy* **25**, 1163–1170 (2000).
- [62] Tartaj, P., Morales, M. P., Gonzalez-Carreño, T., Veintemillas-Verdaguer, S. & Serna, C. J. The Iron Oxides Strike Back: From Biomedical Applications to Energy Storage Devices and Photoelectrochemical Water Splitting. *Advanced Materials* **23**, 5243–5249 (2011).
- [63] Vago, E. R., Calvo, E. J. & Stratmann, M. Electrocatalysis of Oxygen Reduction at Well-Defined Iron Oxide Electrodes (1994).
- [64] Esswein, A. J., McMurdo, M. J., Ross, P. N., Bell, A. T. & Tilley, T. D. Size-Dependent Activity of Co<sub>3</sub>O<sub>4</sub> Nanoparticle Anodes for Alkaline Water Electrolysis. *The Journal of Physical Chemistry C* **113**, 15068–15072 (2009).
- [65] Palmas, S., Ferrara, F., Vacca, A., Mascia, M. & Polcaro, A. M. Behavior of Cobalt Oxide Electrodes During Oxidative Processes in Alkaline Medium. *Electrochimica Acta* **53**, 400–406 (2007).

## Bibliography

---

- [66] Iwakura, C., Honji, A. & Tamura, H. The Anodic Evolution of Oxygen on  $\text{Co}_3\text{O}_4$  Film Electrodes in Alkaline Solutions. *Electrochimica Acta* **26**, 1319–1326 (1981).
- [67] Bergmann, A. *et al.* Reversible Amorphization and the Catalytically Active State of Crystalline  $\text{Co}_3\text{O}_4$  During Oxygen Evolution. *Nature Communications* **6**, 8625 (2015).
- [68] Diebold, U., Koplitz, L. V. & Dulub, O. Atomic-Scale Properties of Low-Index  $\text{ZnO}$  Surfaces. *Applied Surface Science* **237**, 336–342 (2004).
- [69] Diebold, U. The Surface Science of Titanium Dioxide. *Surface Science Reports* **48**, 53–229 (2003).
- [70] Stanka, B., Hebenstreit, W., Diebold, U. & Chambers, S. Surface Reconstruction of  $\text{Fe}_3\text{O}_4(001)$ . *Surface Science* **448**, 49–63 (2000).
- [71] Bliem, R. *et al.* Subsurface Cation Vacancy Stabilization of the Magnetite (001) Surface. *Science* **346**, 1215–1218 (2014).
- [72] Parkinson, G. S., Novotný, Z., Jacobson, P., Schmid, M. & Diebold, U. Room Temperature Water Splitting at the Surface of Magnetite. *Journal of the American Chemical Society* **133**, 12650–5 (2011).
- [73] Bliem, R. *et al.* An Atomic-Scale View of  $\text{CO}$  and  $\text{H}_2$  Oxidation on a  $\text{Pt}/\text{Fe}_3\text{O}_4$  Model Catalyst. *Angewandte Chemie - International Edition* **54**, 1–5 (2015).
- [74] Kolb, D. An Atomistic View of Electrochemistry. *Surface Science* **500**, 722–740 (2002).
- [75] Hoster, H. E. & Gasteiger, H. A. Ex-Situ Surface Preparation and Analysis : Transfer Between UHV and Electrochemical Cell. In Vielstich, W., Lamm, A. & Gasteiger, H. A. (eds.) *Handbook of Fuel Cells - Fundamental, Technology and Application*, vol. 2, chap. 18, 236–265 (John Wiley & Sons, Ltd, Chichester, 2003).
- [76] Mercer, M. P. & Hoster, H. E. Ultrahigh Vacuum and Electrocatalysis – The Powers of Quantitative Surface Imaging. *Nano Energy* **29**, 394–413 (2016).
- [77] Grumelli, D., Wurster, B., Stepanow, S. & Kern, K. Bio-Inspired Nanocatalysts for the Oxygen Reduction Reaction. *Nature Communications* **4**, 2904 (2013).
- [78] Galvani, L. De viribus electricitatis in motu musculari commentarius. *De Bononiensi Scientiarum et Artium Instituto atque Academia Commentarii* **7**, 363–419 (1791).
- [79] Volta, A. & Banks, J. On the Electricity Excited by the Mere Contact of Conducting Substances of Different Kinds. *Philosophical Magazine Series* **7**, 289–311 (1800).
- [80] Faraday, M. *Experimental Researches in Electricity* (Richard and John Edward Taylor, London, 1849).
- [81] Ostwald, W. *Elektrochemie: Ihre Geschichte und Lehre* (Veit and Comp., Leipzig, 1896).

- 
- [82] Greeley, J. & Marković, N. M. The Road from Animal Electricity to Green Energy: Combining Experiment and Theory in Electrocatalysis. *Energy & Environmental Science* **5**, 9246 (2012).
- [83] Hamann, C. H. & Vielstich, W. *Elektrochemie* (Wiley-VCH, Weinheim, 2005), 4 edn.
- [84] Vielstich, W., Lamm, A. & Gasteiger, H. A. *Handbook of Fuel Cells: Fundamentals, Technology, and Applications* (Wiley-VCH, Weinheim, 2003), 1st edn.
- [85] Pletcher, D. *A First Course in Electrode Processes* (The Royal Society of Chemistry, Cambridge, 2009), 1 edn.
- [86] Bard, A. J. & Faulkner, L. R. *Fundamentals and Applications* (John Wiley & Sons, Inc., New York, 2015), 2nd edn.
- [87] Suen, N.-T. *et al.* Electrocatalysis for the Oxygen Evolution Reaction: Recent Development and Future Perspectives. *Chemical Society Reviews* **46**, 337–365 (2017).
- [88] Rossmeisl, J., Karlberg, G. S., Jaramillo, T. F. & Nørskov, J. K. Steady State Oxygen Reduction and Cyclic Voltammetry. *Faraday Discussions* **140**, 337–346 (2009).
- [89] Rossmeisl, J., Qu, Z.-W., Zhu, H., Kroes, G.-J. & Nørskov, J. K. Electrolysis of Water on Oxide Surfaces. *Journal of Electroanalytical Chemistry* **607**, 83–89 (2007).
- [90] Ge, X. *et al.* Oxygen Reduction in Alkaline Media: From Mechanisms to Recent Advances of Catalysts. *ACS Catalysis* **5**, 4643–4667 (2015).
- [91] Binnig, G., Rohrer, H., Gerber, C. & Weibel, E. Surface Studies by Scanning Tunneling Microscopy. *Physical Review Letters* **49**, 57–61 (1982).
- [92] Binnig, G. & Rohrer, H. Scanning Tunneling Microscopy—from Birth to Adolescence. *Reviews of Modern Physics* **59**, 615–625 (1987).
- [93] Tersoff, J. & Hamann, D. R. Theory and Application for the Scanning Tunneling Microscope. *Physical Review Letters* **50**, 1998–2001 (1983).
- [94] Tersoff, J. & Hamann, D. R. Theory of the Scanning Tunneling Microscope. *Physical Review B* **31**, 805–813 (1985).
- [95] Bardeen, J. Tunnelling from a Many-Particle Point of View. *Physical Review Letters* **6**, 57–59 (1961).
- [96] Chen, C. J. *Introduction to Scanning Tunneling Microscopy* (Oxford University Press, 2007), 2 edn.
- [97] Meyer, E., Hug, H. J. & Bennewitz, R. *Scanning Probe Microscopy: The Lab on a Tip* (Springer, Berlin, Heidelberg, 2004).

## Bibliography

---

- [98] Hertz, H. Über einen Einfluss des ultravioletten Lichtes auf die elektrische Entladung. *Annalen der Physik und Chemie* **267**, 983–1000 (1887).
- [99] Einstein, A. Über einen die Erzeugung und Verwandlung des Lichtes betreffenden heuristischen Gesichtspunkt. *Annalen der Physik* **322**, 132–148 (1905).
- [100] Hötger, D. *et al.* Polymorphism and Metal-Induced Structural Transformation in 5,5'-Bis(4-pyridyl)(2,2'-bispyrimidine) Adlayers on Au(111). *Physical Chemistry Chemical Physics* **20**, 15960–15969 (2018).
- [101] Dirac, P. A. M. The Quantum Theory of the Emission and Absorption of Radiation. *Proceedings of the Royal Society A: Mathematical, Physical and Engineering Sciences* **114**, 243–265 (1927).
- [102] Fermi, E. *Nuclear Physics*. August (University of Chicago Press, Chicago, 1974), revised edn.
- [103] Wurster, B., Grumelli, D., Hötger, D., Gutzler, R. & Kern, K. Driving the Oxygen Evolution Reaction by Nonlinear Cooperativity in Bimetallic Coordination Catalysts. *Journal of the American Chemical Society* **138**, 3623–3626 (2016).
- [104] Valdez, C. E., Smith, Q. A., Nechay, M. R. & Alexandrova, A. N. Mysteries of Metals in Metalloenzymes. *Accounts of Chemical Research* **47**, 3110–3117 (2014).
- [105] Lu, Y., Yeung, N., Sieracki, N. & Marshall, N. M. Design of Functional Metalloproteins. *Nature* **460**, 855–862 (2009).
- [106] van den Beuken, E. K. & Feringa, B. L. Bimetallic Catalysis by Late Transition Metal Complexes. *Tetrahedron* **54**, 12985–13011 (1998).
- [107] Lubitz, W., Ogata, H., Rüdiger, O. & Reijerse, E. Hydrogenases. *Chemical Reviews* **114**, 4081–4148 (2014).
- [108] Que, L. & Tolman, W. B. Biologically Inspired Oxidation Catalysis. *Nature* **455**, 333–340 (2008).
- [109] Liu, J. *et al.* Metalloproteins Containing Cytochrome, Iron–Sulfur, or Copper Redox Centers. *Chemical Reviews* **114**, 4366–4469 (2014).
- [110] Rosati, F. & Roelfes, G. Artificial Metalloenzymes. *ChemCatChem* **2**, 916–927 (2010).
- [111] Meeuwissen, J. & Reek, J. N. H. Supramolecular Catalysis Beyond Enzyme Mimics. *Nature Chemistry* **2**, 615–621 (2010).
- [112] Wiester, M. J., Ulmann, P. A. & Mirkin, C. A. Enzyme Mimics Based Upon Supramolecular Coordination Chemistry. *Angewandte Chemie - International Edition* **50**, 114–137 (2011).

- [113] Tait, S. L. *et al.* One-Dimensional Self-Assembled Molecular Chains on Cu(100): Interplay Between Surface-Assisted Coordination Chemistry and Substrate Commensurability. *The Journal of Physical Chemistry C* **111**, 10982–10987 (2007).
- [114] Tait, S. L. *et al.* Assembling Isostructural Metal-Organic Coordination Architectures on Cu(100), Ag(100) and Ag(111) Substrates. *ChemPhysChem* **9**, 2495–2499 (2008).
- [115] Kresse, G. & Furthmüller, J. Efficiency of Ab-Initio Total Energy Calculations for Metals and Semiconductors Using a Plane-Wave Basis Set. *Computational Materials Science* **6**, 15–50 (1996).
- [116] Kresse, G. & Hafner, J. Ab Initio Molecular Dynamics for Open-Shell Transition Metals. *Physical Review B* **48**, 13115–13118 (1993).
- [117] Blöchl, P. E. Projector Augmented-Wave Method. *Physical Review B* **50**, 17953–17979 (1994).
- [118] Klimeš, J. *et al.* Chemical Accuracy for the van-der-Waals Density Functional. *Journal of Physics: Condensed Matter* **22**, 022201 (2010).
- [119] Liu, J. *et al.* Structural Transformation of Two-Dimensional Metal-Organic Coordination Networks Driven by Intrinsic In-Plane Compression. *Journal of the American Chemical Society* **133**, 18760–18766 (2011).
- [120] Boland, T. & Ratner, B. D. Two-Dimensional Assembly of Purines and Pyrimidines on Au(111). *Langmuir* **10**, 3845–3852 (1994).
- [121] Herrera, S. *et al.* Surface Structure of 4-Mercaptopyridine on Au(111): A New Dense Phase. *Langmuir* **33**, 9565–9572 (2017).
- [122] Mateo-Martí, E., Briones, C., Pradier, C. & Martín-Gago, J. A DNA Biosensor Based on Peptide Nucleic Acids on Gold Surfaces. *Biosensors and Bioelectronics* **22**, 1926–1932 (2007).
- [123] Buchner, F. *et al.* Coordination of Iron Atoms by Tetraphenylporphyrin Monolayers and Multilayers on Ag(111) and Formation of Iron-Tetraphenylporphyrin. *The Journal of Physical Chemistry C* **112**, 15458–15465 (2008).
- [124] Artyushkova, K. *et al.* Density Functional Theory Calculations of XPS Binding Energy Shift for Nitrogen-Containing Graphene-Like Structures. *Chemical Communications* **49**, 2539 (2013).
- [125] Yu, W., Porosoff, M. D. & Chen, J. G. Review of Pt-Based Bimetallic Catalysis: From Model Surfaces to Supported Catalysts. *Chemical Reviews* **112**, 5780–5817 (2012).
- [126] Steinhagen, H. & Helmchen, G. Asymmetric Two-Center Catalysis - Learning from Nature. *Angewandte Chemie International Edition in English* **35**, 2339–2342 (1996).

## Bibliography

---

- [127] Li, Y. *et al.* Coordination and Metalation Bifunctionality of Cu with 5,10,15,20-Tetra(4-pyridyl)porphyrin: Toward a Mixed-Valence Two-Dimensional Coordination Network. *Journal of the American Chemical Society* **134**, 6401–6408 (2012).
- [128] Shi, Z. & Lin, N. Self-Assembly of a Two-Dimensional Bimetallic Coordination Framework and Dynamic Control of Reversible Conversions to Homo-Metallic Hydrogen-Bond Arrays. *ChemPhysChem* **11**, 97–100 (2010).
- [129] Bai, Y. *et al.* Adsorption of Cobalt (II) Octaethylporphyrin and 2H-Octaethylporphyrin on Ag(111): New Insight into the Surface Coordinative Bond. *New Journal of Physics* **11**, 125004 (2009).
- [130] Bai, Y. *et al.* Interfacial Coordination Interactions Studied on Cobalt Octaethylporphyrin and Cobalt Tetraphenylporphyrin Monolayers on Au(111). *Physical Chemistry Chemical Physics* **12**, 4336 (2010).
- [131] Lukasczyk, T. *et al.* Interaction of Cobalt(II) Tetraarylporphyrins with a Ag(111) Surface Studied with Photoelectron Spectroscopy. *The Journal of Physical Chemistry C* **111**, 3090–3098 (2007).
- [132] Gottfried, J. M. *et al.* Direct Metalation of a Phthalocyanine Monolayer on Ag ( 111 ) with Coadsorbed Iron Atoms Direct Metalation of a Phthalocyanine Monolayer on Ag ( 111 ) with Coadsorbed Iron Atoms. *Society* 6087–6092 (2008).
- [133] Piamonteze, C. *et al.* X-Treme Beamline at SLS: X-Ray Magnetic Circular and Linear Dichroism at High Field and Low Temperature. *Journal of Synchrotron Radiation* **19**, 661–674 (2012).
- [134] Horcas, I. *et al.* WSxM : A Software for Scanning Probe Microscopy and a Tool for Nanotechnology. *Review of Scientific Instruments* **78**, 013705 (2007).
- [135] Takulapalli, B. R. *et al.* Electrical Detection of Amine Ligation to a Metalloporphyrin via a Hybrid SOI-MOSFET. *Journal of the American Chemical Society* **130**, 2226–2233 (2008).
- [136] Jurow, M., Schuckman, A. E., Batteas, J. D. & Drain, C. M. Porphyrins as Molecular Electronic Components of Functional Devices. *Coordination Chemistry Reviews* **254**, 2297–2310 (2010).
- [137] Hsia, C. C. W. Respiratory Function of Hemoglobin. *New England Journal of Medicine* **338**, 239–248 (1998).
- [138] Groves, J. T. The Bioinorganic Chemistry of Iron in Oxygenases and Supramolecular Assemblies. *Proceedings of the National Academy of Sciences* **100**, 3569–3574 (2003).
- [139] Björn, L. O., Papageorgiou, G. C., Blankenship, R. E. & Govindjee. A Viewpoint: Why Chlorophyll A? *Photosynthesis Research* **99**, 85–98 (2009).

- [140] Marbach, H. Surface-Mediated in Situ Metalation of Porphyrins at the Solid-Vacuum Interface. *Accounts of Chemical Research* **48**, 2649–2658 (2015).
- [141] Gottfried, J. M. & Marbach, H. Surface-Confined Coordination Chemistry with Porphyrins and Phthalocyanines: Aspects of Formation, Electronic Structure, and Reactivity. *Zeitschrift für Physikalische Chemie* **223**, 53–74 (2009).
- [142] Kadish, K. M., Smith, K. M. & Guillard, R. *The Porphyrin Handbook*, vol. 4 (Academic Press, San Diego, 2000), 4th edn.
- [143] Barnes, J. W. & Dorough, G. D. Exchange and Replacement Reactions of  $\alpha,\beta,\gamma,\delta$ -Tetraphenyl-metalloporphins. *Journal of the American Chemical Society* **72**, 4045–4050 (1950).
- [144] Lavalley, D. K. Kinetics and Mechanisms of Metalloporphyrin Reactions. *Coordination Chemistry Reviews* **61**, 55–96 (1985).
- [145] Cheung, S. K., Dixon, F. L., Fleischer, E. B., Jeter, D. Y. & Krishnamurthy, M. Kinetic Studies of the Formation, Acid-Catalyzed Solvolysis, and Cupric Ion Displacement of a Zinc Porphyrin in Aqueous Solutions. *Bioinorganic Chemistry* **2**, 281–294 (1973).
- [146] Shamim, A. & Hambright, P. Exchange Reactions of Transition Metal Ions and Labile Cadmium Porphyrins. *Journal of Inorganic and Nuclear Chemistry* **42**, 1645–1647 (1980).
- [147] Grant, C. & Hambright, P. Kinetics of Electrophilic Substitution Reactions Involving Metal Ions in Metalloporphyrins. *Journal of the American Chemical Society* **91**, 4195–4198 (1969).
- [148] Baker, H., Hambright, P., Wagner, L. & Ross, L. Metal Ion Interactions with Porphyrins. I. Exchange and substitution reactions. *Inorganic Chemistry* **12**, 2200–2202 (1973).
- [149] Hambright, P. & Chock, P. B. Metal-Porphyrin Interactions. III. Dissociative-Interchange Mechanism for Metal Ion Incorporation Into Porphyrin Molecules. *Journal of the American Chemical Society* **96**, 3123–3131 (1974).
- [150] Reid, J. & Hambright, P. Kinetics of Cadmium Porphyrin-Zinc Ion Electrophilic Exchange Reactions: An Isokinetic Relationship. *Inorganica Chimica Acta* **33**, L135–L136 (1979).
- [151] Hieringer, W. *et al.* The Surface Trans Effect: Influence of Axial Ligands on the Surface Chemical Bonds of Adsorbed Metalloporphyrins. *Journal of the American Chemical Society* **133**, 6206–6222 (2011).
- [152] Diller, K. *et al.* Self-Metalation of 2H-Tetraphenylporphyrin on Cu(111): An X-Ray Spectroscopy Study. *The Journal of Chemical Physics* **136**, 014705 (2012).
- [153] Auwärter, W. *et al.* Controlled Metalation of Self-Assembled Porphyrin Nanoarrays in Two Dimensions. *ChemPhysChem* **8**, 250–254 (2007).

## Bibliography

---

- [154] Gottfried, J. M., Flechtner, K., Kretschmann, A., Lukasczyk, T. & Steinrück, H.-P. Direct Synthesis of a Metalloporphyrin Complex on a Surface. *Journal of the American Chemical Society* **128**, 5644–5645 (2006).
- [155] Doyle, C. M. *et al.* Ni–Cu Ion Exchange Observed for Ni(II)–Porphyrins on Cu(111). *Chemical Communications* **50**, 3447 (2014).
- [156] Shen, K. *et al.* On-Surface Manipulation of Atom Substitution Between Cobalt Phthalocyanine and the Cu(111) Substrate. *RSC Advances* **7**, 13827–13835 (2017).
- [157] Franke, M. *et al.* Zinc Porphyrin Metal-Center Exchange at the Solid-Liquid Interface. *Chemistry - A European Journal* **22**, 8520–8524 (2016).
- [158] Rieger, A., Schnidrig, S., Probst, B., Ernst, K.-H. & Wäckerlin, C. Ranking the Stability of Transition-Metal Complexes by On-Surface Atom Exchange. *The Journal of Physical Chemistry Letters* **8**, 6193–6198 (2017).
- [159] Di Santo, G. *et al.* Supramolecular Engineering Through Temperature-Induced Chemical Modification of 2H-Tetraphenylporphyrin on Ag(111): Flat Phenyl Conformation and Possible Dehydrogenation Reactions. *Chemistry - A European Journal* **17**, 14354–14359 (2011).
- [160] Narioka, S. *et al.* XANES Spectroscopic Studies of Evaporated Porphyrin Films: Molecular Orientation and Electronic Structure. *The Journal of Physical Chemistry* **99**, 1332–1337 (1995).
- [161] Miguel, J., Hermanns, C. F., Bernien, M., Krüger, A. & Kuch, W. Reversible Manipulation of the Magnetic Coupling of Single Molecular Spins in Fe-Porphyrins to a Ferromagnetic Substrate. *The Journal of Physical Chemistry Letters* **2**, 1455–1459 (2011).
- [162] Scherz, A. *et al.* Measuring the Kernel of Time-Dependent Density Functional Theory with X-Ray Absorption Spectroscopy of 3d Transition Metals. *Physical Review Letters* **95**, 3–6 (2005). 0511016.
- [163] Chen, C. T. *et al.* Experimental Confirmation of the X-Ray Magnetic Circular Dichroism Sum Rules for Iron and Cobalt. *Physical Review Letters* **75**, 152–155 (1995).
- [164] Vijayaraghavan, S. *et al.* Restoring the Co Magnetic Moments at Interfacial Co-Porphyrin Arrays by Site-Selective Uptake of Iron. *ACS Nano* **9**, 3605–3616 (2015).
- [165] Regan, T. *et al.* Chemical Effects at Metal/Oxide Interfaces Studied by X-Ray-Absorption Spectroscopy. *Physical Review B* **64**, 1–11 (2001).
- [166] Kresse, G. & Joubert, D. From Ultrasoft Pseudopotentials to the Projector Augmented-Wave Method. *Physical Review B* **59**, 1758–1775 (1999).
- [167] Tang, W., Sanville, E. & Henkelman, G. A Grid-Based Bader Analysis Algorithm Without Lattice Bias. *Journal of Physics Condensed Matter* **21**, 084204 (2009).

- [168] Auwärter, W. *et al.* Conformational Adaptation and Selective Adatom Capturing of Tetrapyrrolyl-Porphyrin Molecules on a Copper (111) Surface. *Journal of the American Chemical Society* **129**, 11279–11285 (2007).
- [169] Lin, T., Kuang, G., Wang, W. & Lin, N. Two-Dimensional Lattice of Out-of-Plane Dinuclear Iron Centers Exhibiting Kondo Resonance. *ACS Nano* **8**, 8310–8316 (2014).
- [170] Wang, Y., Zhou, K., Shi, Z. & Ma, Y.-Q. Structural Reconstruction and Spontaneous Formation of Fe Polynuclears: A Self-Assembly of Fe–Porphyrin Coordination Chains on Au(111) Revealed by Scanning Tunneling Microscopy. *Physical Chemistry Chemical Physics* **18**, 14273–14278 (2016).
- [171] Stepanow, S. *et al.* Giant Spin and Orbital Moment Anisotropies of a Cu-Phthalocyanine Monolayer. *Physical Review B* **82**, 014405 (2010).
- [172] Shubina, T. E. *et al.* Principle and Mechanism of Direct Porphyrin Metalation: Joint Experimental and Theoretical Investigation. *Journal of the American Chemical Society* **129**, 9476–9483 (2007).
- [173] Buchner, F., Schwald, V., Comanici, K., Steinrück, H.-P. & Marbach, H. Microscopic Evidence of the Metalation of a Free-Base Porphyrin Monolayer with Iron. *ChemPhysChem* **8**, 241–243 (2007).
- [174] Wiesener, K., Ohms, D., Neumann, V. & Franke, R. N<sub>4</sub> Macrocycles as Electrocatalysts for the Cathodic Reduction of Oxygen. *Materials Chemistry and Physics* **22**, 457–475 (1989).
- [175] Hod, I. *et al.* Fe-Porphyrin-Based Metal-Organic Framework Films as High-Surface Concentration, Heterogeneous Catalysts for Electrochemical Reduction of CO<sub>2</sub>. *ACS Catalysis* **5**, 6302–6309 (2015).
- [176] Collman, J. P. *et al.* A Cytochrome C Oxidase Model Under Rate-Limiting Electron Flux. *Science* **315**, 1565–1569 (2007).
- [177] Carver, C. T., Matson, B. D. & Mayer, J. M. Electrocatalytic Oxygen Reduction by Iron Tetraarylporphyrins Bearing Pendant Proton Relays. *Journal of the American Chemical Society* **134**, 5444–5447 (2012).
- [178] He, Q., Mugadza, T., Hwang, G. & Nyokong, T. Mechanisms of Electrocatalysis of Oxygen Reduction by Metal Porphyrins in Trifluoromethane Sulfonic Acid Solution. *International Journal of Electrochemical Science* **7**, 7045–7064 (2012).
- [179] Jahan, M., Bao, Q. & Loh, K. P. Electrocatalytically Active Graphene–Porphyrin MOF Composite for Oxygen Reduction Reaction. *Journal of the American Chemical Society* **134**, 6707–6713 (2012).
- [180] Bezerra, C. W. B. *et al.* A Review of Fe-N/C and Co-N/C Catalysts for the Oxygen Reduction Reaction. *Electrochimica Acta* **53**, 4937–4951 (2008).

## Bibliography

---

- [181] Miedema, P. S. *et al.* Oxygen Binding to Cobalt and Iron Phthalocyanines As Determined from in Situ X-Ray Absorption Spectroscopy. *The Journal of Physical Chemistry C* **115**, 25422–25428 (2011).
- [182] Miedema, P. S. & de Groot, F. M. The Iron L edges: Fe 2p X-Ray Absorption and Electron Energy Loss Spectroscopy. *Journal of Electron Spectroscopy and Related Phenomena* **187**, 32–48 (2013).
- [183] Kuiper, P., Searle, B. G., Duda, L. C., Wolf, R. M. & VanderZaag, P. J. Fe L<sub>2,3</sub> Linear and Circular Magnetic Dichroism of Fe<sub>3</sub>O<sub>4</sub>. *Journal of Electron Spectroscopy and Related Phenomena* **86**, 107–113 (1997).
- [184] Brice-Profeta, S. *et al.* Magnetic Order in Nanoparticles: A XMCD Study. *Journal of Magnetism and Magnetic Materials* **288**, 354–365 (2005).
- [185] Walton, A. S. *et al.* Interface Controlled Oxidation States in Layered Cobalt Oxide Nanoislands on Gold. *ACS Nano* **9**, 2445–2453 (2015).
- [186] Fester, J. *et al.* Edge Reactivity and Water-Assisted Dissociation on Cobalt Oxide Nanoislands. *Nature Communications* **8**, 14169 (2017).
- [187] Stracke, J. J. & Finke, R. G. Electrocatalytic Water Oxidation Beginning with the Cobalt Polyoxometalate [Co<sub>4</sub>(H<sub>2</sub>O)<sub>2</sub>(PW<sub>9</sub>O<sub>34</sub>)<sub>2</sub>]<sub>0</sub><sup>1-</sup>: Identification of Heterogeneous CoO<sub>x</sub> as the Dominant Catalyst. *Journal of the American Chemical Society* **133**, 14872–14875 (2011).
- [188] Jiao, F. & Frei, H. Nanostructured Cobalt Oxide Clusters in Mesoporous Silica as Efficient Oxygen-Evolving Catalysts. *Angewandte Chemie - International Edition* **48**, 1841–1844 (2009).
- [189] Yeo, B. S. & Bell, A. T. Enhanced Activity of Gold-Supported Cobalt Oxide for the Electrochemical Evolution of Oxygen. *Journal of the American Chemical Society* **133**, 5587–5593 (2011).
- [190] Rosen, J., Hutchings, G. S. & Jiao, F. Ordered Mesoporous Cobalt Oxide as Highly Efficient Oxygen Evolution Catalyst. *Journal of the American Chemical Society* **135**, 4516–4521 (2013).
- [191] Friebe, D. *et al.* On the Chemical State of Co Oxide Electrocatalysts During Alkaline Water Splitting. *Physical Chemistry Chemical Physics* **15**, 17460 (2013).
- [192] Bajdich, M., García-Mota, M., Vojvodic, A., Nørskov, J. K. & Bell, A. T. Theoretical Investigation of the Activity of Cobalt Oxides for the Electrochemical Oxidation of Water. *Journal of the American Chemical Society* **135**, 13521–13530 (2013).
- [193] McAlpin, J. G. *et al.* EPR Evidence for Co(IV) Species Produced During Water Oxidation at Neutral pH. *Journal of the American Chemical Society* **132**, 6882–6883 (2010).

- [194] Fester, J., Walton, A., Li, Z. & Lauritsen, J. V. Gold-Supported Two-Dimensional Cobalt Oxyhydroxide (CoOOH) and Multilayer Cobalt Oxide Islands. *Physical Chemistry Chemical Physics* **19**, 2425–2433 (2017).
- [195] McIntyre, N. S. & Cook, M. G. X-Ray Photoelectron Studies on Some Oxides and Hydroxides of Cobalt, Nickel, and Copper. *Analytical Chemistry* **47**, 2208–2213 (1975).
- [196] Strydom, C. & Strydom, H. X-Ray Photoelectron Spectroscopy Studies of Some Cobalt(II) Nitrate Complexes. *Inorganica Chimica Acta* **159**, 191–195 (1989).
- [197] Raaen, S. Correlation Effects in 3d Transition Metals: Presence of a Two-Hole Core-Satellite in Cobalt. *Solid State Communications* **60**, 991–993 (1986).
- [198] Barreca, D. *et al.* Composition and Microstructure of Cobalt Oxide Thin Films Obtained from a Novel Cobalt(II) Precursor by Chemical Vapor Deposition. *Chemistry of Materials* **13**, 588–593 (2001).
- [199] Tyuliev, G. & Angelov, S. The Nature of Excess Oxygen in  $\text{Co}_3\text{O}_{4+\epsilon}$ . *Applied Surface Science* **32**, 381–391 (1988).
- [200] He, H. *et al.* Natural Magnetite: An Efficient Catalyst for the Degradation of Organic Contaminant. *Scientific Reports* **5**, 10139 (2015).
- [201] Thackeray, M., David, W. & Goodenough, J. Structural Characterization of the Lithiated Iron Oxides  $\text{Li}_x\text{Fe}_3\text{O}_4$  and  $\text{Li}_x\text{Fe}_2\text{O}_3$  ( $0 < x < 2$ ). *Materials Research Bulletin* **17**, 785–793 (1982).
- [202] Di Pietro, B., Patriarca, M. & Scrosati, B. On the Use of Rocking Chair Configurations for Cyclable Lithium Organic Electrolyte Batteries. *Journal of Power Sources* **8**, 289–299 (1982).
- [203] Sharghi, H., Jokar, M., Doroodmand, M. M. & Khalifeh, R. Catalytic Friedel-Crafts Acylation and Benzoylation of Aromatic Compounds Using Activated Hematite as a Novel Heterogeneous Catalyst. *Advanced Synthesis & Catalysis* **352**, 3031–3044 (2010).
- [204] Baeza, A., Guillena, G. & Ramón, D. J. Magnetite and Metal-Impregnated Magnetite Catalysts in Organic Synthesis: A Very Old Concept with New Promising Perspectives. *ChemCatChem* **8**, 49–67 (2016).
- [205] Parkinson, G. S. Iron Oxide Surfaces. *Surface Science Reports* **71**, 272–365 (2016).
- [206] Arndt, B. *et al.* Atomic Structure and Stability of Magnetite  $\text{Fe}_3\text{O}_4$  (001): An X-Ray View. *Surface Science* **653**, 76–81 (2016).
- [207] Gargallo-Caballero, R. *et al.* Co on  $\text{Fe}_3\text{O}_4$ (001): Towards Precise Control of Surface Properties. *The Journal of Chemical Physics* **144**, 094704 (2016).

## Bibliography

---

- [208] Castro, P. A., Vago, E. R. & Calvo, E. J. Surface Electrochemical Transformations on Spinel Iron Oxide Electrodes in Aqueous Solutions. *Journal of the Chemical Society, Faraday Transactions* **92**, 3371 (1996).
- [209] Widmann, D. & Behm, R. J. Activation of Molecular Oxygen and the Nature of the Active Oxygen Species for CO Oxidation on Oxide Supported Au Catalysts. *Accounts of Chemical Research* **47**, 740–749 (2014).
- [210] Novotný, Z. *et al.* Ordered Array of Single Adatoms with Remarkable Thermal Stability: Au/Fe<sub>3</sub>O<sub>4</sub>(001). *Physical Review Letters* **108**, 1–5 (2012).
- [211] Bliem, R. *et al.* Cluster Nucleation and Growth from a Highly Supersaturated Adatom Phase: Silver on Magnetite. *ACS Nano* **8**, 7531–7537 (2014).
- [212] Novotný, Z. *et al.* Probing the Surface Phase Diagram of Fe<sub>3</sub>O<sub>4</sub>(001) Towards the Fe-Rich Limit: Evidence for Progressive Reduction of the Surface. *Physical Review B* **87**, 195410 (2013).
- [213] Parkinson, G. S. *et al.* Carbon Monoxide-Induced Adatom Sintering in a Pd-Fe<sub>3</sub>O<sub>4</sub> Model Catalyst. *Nature Materials* **12**, 724–8 (2013).
- [214] Bliem, R. *et al.* Adsorption and Incorporation of Transition Metals at the Magnetite Fe<sub>3</sub>O<sub>4</sub> (001) Surface. *Physical Review B* **92**, 075440 (2015).
- [215] Yang, X.-F. *et al.* Single-Atom Catalysts: A New Frontier in Heterogeneous Catalysis. *Accounts of Chemical Research* **46**, 1740–1748 (2013).
- [216] Rao, C. N. R., Kulkarni, G. U., Thomas, P. J. & Edwards, P. P. Size-Dependent Chemistry: Properties of Nanocrystals. *Chemistry - A European Journal* **8**, 28–35 (2002).
- [217] Thomas, J. M., Raja, R. & Lewis, D. W. Single-Site Heterogeneous Catalysts. *Angewandte Chemie - International Edition* **44**, 6456–6482 (2005).
- [218] Qiao, B. *et al.* Single-Atom Catalysis of CO Oxidation Using Pt<sub>1</sub>/FeO<sub>x</sub>. *Nature Chemistry* **3**, 634–641 (2011).
- [219] Lin, J. *et al.* Remarkable Performance of Ir<sub>1</sub>/FeO<sub>x</sub> Single-Atom Catalyst in Water Gas Shift Reaction. *Journal of the American Chemical Society* **135**, 15314–7 (2013).
- [220] Allen, P., Hampson, N., Tyson, J. & Bignold, G. The Differential Capacitance of Magnetite. *Surface Technology* **9**, 395–400 (1979).
- [221] Miller, D. J., Biesinger, M. C. & McIntyre, N. S. Interactions of CO<sub>2</sub> and CO at Fractional Atmosphere Pressures with Iron and Iron Oxide Surfaces: One Possible Mechanism for Surface Contamination? *Surface and Interface Analysis* **33**, 299–305 (2002).
- [222] Xue, G., Dai, Q. & Jiang, S. Chemical Reactions of Imidazole with Metallic Silver Studied by the use of SERS and XPS Techniques. *Journal of the American Chemical Society* **110**, 2393–2395 (1988).

- [223] Zheng, Y. *et al.* Ag/ZnO Heterostructure Nanocrystals: Synthesis, Characterization, and Photocatalysis. *Inorganic Chemistry* **46**, 6980–6986 (2007).
- [224] Lopez-Salido, I., Lim, D. C. & Kim, Y. D. Ag Nanoparticles on Highly Ordered Pyrolytic Graphite (HOPG) Surfaces Studied Using STM and XPS. *Surface Science* **588**, 6–18 (2005).
- [225] Hoflund, G. B., Weaver, J. F. & Epling, W. S. Ag Foil by XPS. *Surface Science Spectra* **3**, 151–156 (1994).
- [226] Chambers, S. A., Kim, Y. J. & Gao, Y. Fe 2p Core-Level Spectra for Pure, Epitaxial  $\alpha$ -Fe<sub>2</sub>O<sub>3</sub>(0001),  $\gamma$ -Fe<sub>2</sub>O<sub>3</sub>(001), and Fe<sub>3</sub>O<sub>4</sub>(001). *Surface Science Spectra* **5**, 219–228 (1998).
- [227] Amarjargal, A., Tijing, L. D., Im, I.-T. & Kim, C. S. Simultaneous Preparation of Ag/Fe<sub>3</sub>O<sub>4</sub> Core-Shell Nanocomposites with Enhanced Magnetic Moment and Strong Antibacterial and Catalytic Properties. *Chemical Engineering Journal* **226**, 243–254 (2013).
- [228] Vago, E. R. & Calvo, E. J. Electrocatalysis of Oxygen Reduction at Fe<sub>3</sub>O<sub>4</sub> Oxide Electrodes in Alkaline Solutions. *Journal of Electroanalytical Chemistry* **339**, 41–67 (1992).
- [229] Hsu, J.-H., Chen, S.-Y. & Chang, C.-R. Anomalous Positive Magnetoresistance in Fe<sub>3</sub>O<sub>4</sub>-Ag Composite Films. *Journal of Magnetism and Magnetic Materials* **242–245**, 479–481 (2002).
- [230] Hsu, J.-H. *et al.* Magnetoresistance Effect in Ag-Fe<sub>3</sub>O<sub>4</sub> and Al-Fe<sub>3</sub>O<sub>4</sub> Composite Films. *Journal of Applied Physics* **93**, 7702–7704 (2003).
- [231] Master, R., Choudhary, R. J. & Phase, D. M. Effect of Silver Addition on Structural, Electrical and Magnetic Properties of Fe<sub>3</sub>O<sub>4</sub> Thin Films Prepared by Pulsed Laser Deposition. *Journal of Applied Physics* **111**, 073907 (2012).
- [232] Lackinger, M. Surface-Assisted Ullmann Coupling. *Chemical Communications* **53**, 7872–7885 (2017).
- [233] Fan, Q., Gottfried, J. M. & Zhu, J. Surface-Catalyzed C–C Covalent Coupling Strategies Toward the Synthesis of Low-Dimensional Carbon-Based Nanostructures. *Accounts of Chemical Research* **48**, 2484–2494 (2015).
- [234] Lafferentz, L. *et al.* Controlling On-Surface Polymerization by Hierarchical and Substrate-Directed Growth. *Nature Chemistry* **4**, 215–220 (2012).
- [235] Eichhorn, J. *et al.* On-Surface Ullmann Coupling: The Influence of Kinetic Reaction Parameters on the Morphology and Quality of Covalent Networks. *ACS Nano* **8**, 7880–7889 (2014).
- [236] Seh, Z. W. *et al.* Combining Theory and Experiment in Electrocatalysis: Insights into Materials Design. *Science* **355**, eaad4998 (2017).

## Bibliography

---

- [237] Wang, C.-H., Yang, C.-W., Lin, Y.-C., Chang, S.-T. & Chang, S. L. Cobalt–Iron(II,III) Oxide Hybrid Catalysis with Enhanced Catalytic Activities for Oxygen Reduction in Anion Exchange Membrane Fuel Cell. *Journal of Power Sources* **277**, 147–154 (2015).
- [238] Lindgren, A., Munteanu, F.-D., Gazaryan, I. G., Ruzgas, T. & Gorton, L. Comparison of Rotating Disk and Wall-Jet Electrode Systems for Studying the Kinetics of Direct and Mediated Electron Transfer for Horseradish Peroxidase on a Graphite Electrode. *Journal of Electroanalytical Chemistry* **458**, 113–120 (1998).
- [239] Hoster, H. & Behm, R. J. The Effect of Structurally Well-Defined Pt Modification on the Electrochemical and Electrocatalytic Properties of Ru(0001) Electrodes. In Koper, M. T. M. (ed.) *Fuel Cell Catalysis*, 465–505 (John Wiley & Sons, Inc., Hoboken, NJ, USA, 2008).
- [240] Zhang, D., Deutschmann, O., Seidel, Y. E. & Behm, R. J. Interaction of Mass Transport and Reaction Kinetics During Electrocatalytic CO Oxidation in a Thin-Layer Flow Cell. *The Journal of Physical Chemistry C* **115**, 468–478 (2011).
- [241] Baltruschat, H. Differential Electrochemical Mass Spectrometry. *Journal of the American Society for Mass Spectrometry* **15**, 1693–1706 (2004).

# Acknowledgements

A PhD thesis is never a one (wo)man show and I would like to take the time to express my gratitude to the people who contributed in many different ways to the success of this work.

First, I would like to thank Prof. Klaus Kern for the opportunity to work in his department at the Max Planck Institute for Solid State Research in Stuttgart. I am thankful for the freedom he gave me during the past years as well as the chance to present my research at several conferences.

I also thank the members of my thesis committee, Prof. Karen Scrivener, Prof. Michael Gottfried, Prof. Sabine Maier, and Prof. Anna Fontcuberta i Morral for their time and work.

Special thanks go to my daily-supervisor Dr. Rico Gutzler. Our numerous scientific discussions and his expertise helped me to learn how to approach scientific questions. Translating between the language of physics and chemistry became a lot easier over the years. Thank you, for your faith in me and for always being there when necessary.

I thank Prof. Doris Grumelli for sharing her electrochemical knowledge and her enthusiasm about research. I really enjoyed our conversations about science and beyond.

I cannot imagine this thesis without the support of Dr. Markus Etzkorn who introduced me to the world of x-ray absorption spectroscopy. I appreciate his constructive comments and his advice which guided me one step closer to understand our results.

I am indebted to the team of two beamtimes at the Swiss Light Source, Dr. Jan Dreiser, Dr. Markus Etzkorn, Dr. Rico Gutzler, Dr. Claudius Morchutt, and Dr. Sebastian Stepanow. These highly intense weeks not only formed the major part of my thesis but also let me grow as a scientist.

Many collaborations promoted a deep understanding of the various electrocatalysts. The thought-provoking impulses and interesting discussions influenced this thesis strongly. DFT calculations by Dr. Paula Abufager and Dr. H. Fabio Busnengo helped explaining the exchange mechanism. Thank you, for many helpful emails and Skype meetings. Moreover, I would like to thank Dr. Pilar Carro for the theoretical insights into the stability of the PBP+Fe network. Together with Anton Makoveev, I explored the behavior of cobalt as an electrocatalyst. In this context the expertise of Jakob Fester helped us a lot to develop future projects and for understanding the collected data. The experience of Dr. Roland Bliem, Santiago Herrera, and Prof. Gareth Parkinson supported my work with magnetite as a novel substrate for electrocatalysis. For the interesting XPS and LEED experiments on magnetite, I thank Dr. Kathrin Müller.

## Acknowledgements

---

Furthermore, I would like to thank my predecessor Dr. Benjamin Wurster for his detailed introduction to the experimental set-up. Moreover, Dr. Benjamin Wurster and Dr. Claudius Morchutt simplified the first period of my PhD and I was glad to work with them in the lab. Most of my time in the past years I spend in the lab 6B15, including many ups and downs. Thank you, Patrick Alexa, Pascal Gröger, Santiago Herrera, Anton Makoveev, Dr. Claudius Morchutt, Miriam Rodriguez, and Dr. Benjamin Wurster for the supportive atmosphere we had. I remember numerous funny moments, lively debates and the good music which was extremely motivating.

I acknowledge our highly enthusiastic and competent technicians, Peter Andler, Marko Memmler and Wolfgang Stiepany who supported me in maintaining the sophisticated experimental set-up. Furthermore, I would like to thank the heart of our department, Sabine Birtel, who guided me through the jungle of bureaucracy.

Our lunch group often enriched my day, thank you, Dr. Sabine Abb, Dr. Christian Dette, Dr. Christoph Große, Dr. Rico Gutzler, Lukas Krumbein, Dr. Claudius Morchutt, Hannah Ochner, Katharina Polyudov, Anna Roslowska, Alessio Scavuzzo, Sven Szilagyi, Andreas Topp, Dr. Benjamin Wurster, and many more who joined us at our crowded table for colorful discussions about life, football, chess and science. I enjoyed working in the Nanoscale Science department and I would like to thank all group members for the creative and warm atmosphere in the past years.

Thank you, Dr. Jacob Senkpiel for accompanying me through the whole PhD process at EPFL starting from the first year exam to the soutenance. Thank you for sharing travel time, information and experience. I appreciated your support and your friendship.

Furthermore, I am thankful for many coffee breaks, legendary cooking and Sushi evenings with Dr. Sabine Abb and Andreas Topp. Often the world looked differently afterwards (mostly better). Often it was not necessary to explain the facts, you just understood. Sabine, particularly your positive power always impressed and encouraged me.

Last but not least I would like to thank my family and friends as you are one of the most important parts of my life: Ohne meine Eltern und Geschwister würde ich heute wohl nicht an dieser Stelle stehen. Ich danke euch für eure Unterstützung, eure Liebe und euer Vertrauen. Ihr habt mir immer den Rücken gestärkt und ich würde wohl ohne euch nicht so selbstbewusst durch das Leben gehen.

Ich möchte mich auch an dieser Stelle bei meinen Freunden ganz herzlich bedanken für die Begleitung durch die letzten Jahre, für die offenen Ohren, für euer Verständnis, für den Zuspruch und eure Unterstützung. Das Leben wäre so viel weniger spannend, lustig und schön ohne euch. Danke, dass ich mich bei euch immer aufgehoben fühle.

Zum Schluss möchte ich Luca, der wohl wichtigsten Person in meinem Leben, danken. Danke, dass du mit mir ein Leben teilst. Ich danke dir für deine unerschütterliche Geduld, deine Liebe, deine Unterstützung, dein Verständnis, dein Frohsinn und deinen Glauben an mich. Du kannst mir eigentlich immer ein Lächeln ins Gesicht zaubern und versuchst mir jedes Gewicht von den Schultern zu nehmen. Du wusstest schon wesentlich früher als ich, dass dieser Tag kommen wird. Was wohl als nächstes auf uns wartet?

# Curriculum Vitae

*Name* Diana Hötger  
*Address* Brückenstraße 55  
70376 Stuttgart  
Germany  
*Birth* May, 2 1989  
in Pforzheim, Germany

## EDUCATION

*July 14 – present* **Doctoral Studies (PhD)**  
École Polytechnique Fédérale de Lausanne, Switzerland  
Doctoral School: Materials Science and Engineering  
Research assistant in the department of nanoscale science (Prof. Klaus Kern), Max Planck Institute for Solid State Research, Stuttgart, Germany

*Mar 13 – Sep 13* **Research Exchange**  
Università degli Studi di Bari "Aldo Moro", Italy  
Topic: *Electrosynthesis of ZnO nanoparticles for organic field effect transistors*  
in the group of Prof. Nicola Cioffi and Luisa Torsi

*Oct 12 – May 14* **Master Studies in Chemistry**  
Universität Ulm, Germany  
Master thesis: *Nanoparticle Enhanced Biosensors Based on Zinc Oxide and Gold Nanoparticles*  
in the group of Prof. Boris Mizaikoff and P.D. Christine Kranz

*Oct 09 – July 12* **Bachelor Studies in Chemistry and Management**  
Universität Ulm, Germany  
Bachelor thesis: *Gold Nanoparticle for Biosensors*  
in the group of Prof. Boris Mizaikoff and P.D. Christine Kranz

*1999 – 2008* **Gymnasium (High School)**  
Johannes Kepler Gymnasium, Pforzheim, Germany

### AWARDS & HONORS

- Mar 17            **Student Poster Award Ascona 2017**  
                      *"Iron – Cobalt Exchange by Cobalt Metalation of a Self-Assembled Iron-Porphyrin Network on Au(111)"*  
                      Conference on Molecular Nanostructures, Ascona, 2017
- Jan 15            **Student Poster Award**  
                      *"Two-Dimensional Metal-Organic Networks as Heterogeneous Nanocatalysts"*  
                      Conference on Electrochemical Surface Science, Bad Honnef, 2015
- June 08 – present    **e-fellows.net Scholarship**

### CONFERENCES

- Aug 17            ECOS17, Szeged (Hungary)  
                      *"On-Surface Transmetalation of Fe-Porphyrin Networks on Au(111)"* (talk)
- Mar 17            DPG Spring Meeting, Dresden (Germany)  
                      *"Stability of Metalloporphyrin Networks Under Oxygen Reduction and Evolution Conditions in Basic Media"* (talk)
- Mar 17            Conference on Molecular Nanostructures, Ascona (Switzerland)  
                      *"Iron – Cobalt Exchange by Cobalt Metalation of a Self-Assembled Iron-Porphyrin Network on Au(111)"* (poster)
- Feb 17            Gordon Research Conference on Chemical Reactions on Surfaces, Lucca (Italy)  
                      *"Structural Change of a Bifunctional Metalloporphyrin Network for Oxygen Reduction and Evolution Reaction in Alkaline Media"* (poster)
- July 16            Conference on Molecular Nanostructures, Berlin (Germany)  
                      *"Electronic and Magnetic Structure of a Bimetallic Tetrapyrrolylporphyrin Electrocatalyst Probed by XMCD"* (poster)
- Mar 16            DPG spring meeting, Regensburg (Germany)  
                      *"Enhancement of Electrocatalytic Activity for Oxygen Evolution in Bimetallic Tetrapyrrolylporphyrin Networks"* (talk)
- Mar 15            DPG Spring Meeting, Berlin (Germany)  
                      *Electrochemistry of Natural Polycrystalline vs. Natural Single Crystal magnetite* (poster)
- Jan 15            Conference on Electrochemical Surface Science, Bad Honnef (Germany)  
                      *"Two-Dimensional Metal-Organic Networks as Heterogeneous Nanocatalysts"* (poster)

## PUBLICATIONS

1. Santiago Herrera, Evangelina Pensa, Diana Hötger, Rico Gutzler, Doris Grumelli, Klaus Kern, "Phthalocyanine: UHV vs. Vacuum" *In preparation*
2. Diana Hötger, Paula Abufager, Claudius Morchutt, Patrick Alexa, Doris Grumelli, Jan Dreiser, Sebastian Stepanow, Pietro Gambardella, H. Fabio Busnengo, Markus Etzkorn, Rico Gutzler, Klaus Kern, "On-Surface Transmetalation of Metalloporphyrins" *submitted*
3. Diana Hötger, Markus Etzkorn, Claudius Morchutt, Jan Dreiser, Sebastian Stepanow, Doris Grumelli, Rico Gutzler, Klaus Kern, "Stability of Bifunctional Metalloporphyrin Networks under Oxygen Reduction and Evolution Conditions in Basic Media" *submitted*
4. Diana Hötger, Pilar Carro, Rico Gutzler, Benjamin Wurster, Rajadurai Chandrasekar, Svetlana Klyatskaya, Mario Ruben, Roberto C. Salvarezza, Klaus Kern, Doris Grumelli "Polymorphism and Metal Induced Structural Transformation in 5,5'-bis(4-pyridyl)(2,2'-bispyrimidine) Adlayers on Au(111)" *Physical Chemistry Chemical Physics*, **2018**
5. Benjamin Wurster, Doris Grumelli, Diana Hötger, Rico Gutzler, K. Kern, "Driving the Oxygen Evolution Reaction by Nonlinear Cooperativity in Bimetallic Coordination Catalysts" *Journal of the American Chemical Society*, **2016**
6. Rosaria Anna Picca, Maria Chiara Sportelli, Diana Hötger, Kyriaki Manoli, Christine Kranz, Boris Mizaikoff, Luisa Torsi, Nicola Cioffi, "Electrosynthesis and Characterization of ZnO Nanoparticles as Inorganic Component in Organic Thin-Film Transistors Active Layer" *Electrochimica Acta*, **2015**.
7. Maria Chiara Sportelli, Diana Hötger, Rosaria Anna Picca, Kyriaki Manoli, Christine Kranz, Boris Mizaikoff, Luisa Torsi, Nicola Cioffi, "Electrosynthesized Polystyrene Sulphonate-Capped Zinc Oxide Nanoparticles as Electrode Modifiers for Sensing Devices" *MRS Proceedings*, **2014**.